SLAC-R-665

A measurement of the lambda-c baryon decays to proton kaon(-) pion(+) absolute branching fraction with the BaBar detector [*]

Christopher M. Roat

Stanford Linear Accelerator Center
Stanford University
Stanford, CA 94309

SLAC-Report-665
May 2003

Prepared for the Department of Energy
under contract number DE-AC03-76SF00515

Printed in the United States of America. Available from the National Technical Information Service, U.S. Department of Commerce, 5285 Port Royal Road, Springfield, VA 22161.

[*] Ph.D. thesis, Stanford University, Stanford CA 94309

A MEASUREMENT OF THE $\Lambda_c^+ \to pK^-\pi^+$ ABSOLUTE BRANCHING FRACTION WITH THE BABAR DETECTOR

A DISSERTATION

SUBMITTED TO THE DEPARTMENT OF PHYSICS

AND THE COMMITTEE ON GRADUATE STUDIES

OF STANFORD UNIVERSITY

IN PARTIAL FULFILLMENT OF THE REQUIREMENTS

FOR THE DEGREE OF

DOCTOR OF PHILOSOPHY

Christopher M. Roat

May 2003

I certify that I have read this dissertation and that, in my opinion, it is fully adequate in scope and quality as a dissertation for the degree of Doctor of Philosophy.

Patricia Burchat
(Principal Adviser)

I certify that I have read this dissertation and that, in my opinion, it is fully adequate in scope and quality as a dissertation for the degree of Doctor of Philosophy.

Giorgio Gratta

I certify that I have read this dissertation and that, in my opinion, it is fully adequate in scope and quality as a dissertation for the degree of Doctor of Philosophy.

Scott Thomas

Approved for the University Committee on Graduate Studies.

Abstract

A measurement of $\mathcal{B}(\Lambda_c^+ \to pK^-\pi^+)$ is presented based on data collected with the BaBar detector at the Stanford Linear Accelerator Center. Branching fraction measurements represent a large portion of what is known about short-lived particles, the strong force that binds them, and the weak force that causes them to decay. While the majority of branching fraction measurements are done as ratios between two decay modes, it is the absolute measurements of a few particular decay modes that set the scale for these relative measurements. The Λ_c^+ particle is one of the four weakly decaying hadrons into which more than 90% of the known heavy quark hadrons will eventually decay. Thus, an absolute measurement of the branching fraction for $\Lambda_c^+ \to pK^-\pi^+$ is important for many studies of the heavy quark sector, from spectroscopy to B meson decays. The number of produced Λ_c^+'s is inferred from the number of events reconstructed with an antiproton and an accompanying $\overline{D}$ meson. The final result of $\mathcal{B}(\Lambda_c^+ \to pK^-\pi^+) = [6.12 \pm 0.31(stat.) \pm 0.42(syst.)]\%$ represents more than a two-fold improvement in precision over the world average. The dominant source of systematic uncertainty is the irreducible background of Ξ_c baryons.

Acknowledgments

After so many years, I have quite a list of people to thank! Here goes... and to those I may have forgotten, please forgive me.

Pat Burchat for allowing me to find my own path and always being available at the drop of a hat to help with any question. She has been a good role model, providing a glimpse of how to combine a challenging career and a rewarding life.

David Kirkby for taking the time to show me the ropes. He's a very clever and brilliant physicist, and I would not have wanted to learn from anyone else.

Tim and Chih-hsiang for providing intelligent insights dispersed among the normal patter at the office. Good luck to them both!

Brian, Adam, and Stephanie for bringing in the new guard for the group. It looks to be in great hands.

Linda, Maria, Muriel, Jennifer, Marcia and all other members of the Varian staff over the years. They've done a great job keeping the Stanford physics department running smoothly day in and day out.

Special thanks to all my friends who made Stanford an enjoyable experience over the

years: Mat, Bob, Nabeel, Jarett, Brian, Emily, Laura, Bart, Jon, Nathan, Vineet, Chris H., Marc, Tammi, Terry, Matt, Becky, Bryan, Jeremy, Monica, Steph, Jersey, Will, Rich, Pete, Joyce, and Alex F.

Stanford Masters Swimming for providing a excellent program and a great way blow off extra steam after a hard day of thesis work. Thanks to all the coaches: Tim, Ross & Judy, Holly, Bruce, Greg, Jody; as well as Sam & Jane, Dr. January, Steve, Randy, Carr, Tim and all the rest of that over-chlorinated bunch.

Kim for all of her love and support. She has been a great traveling companion and a reminder that there's more out there than just fermions and bosons. I'm so lucky to have found her! I also owe a big thanks to Kim's parents, Ned & Jimi, for providing a home away from home and making sure my stomach always stayed full.

Finally and most of all, I would like to thank my parents, Anne & Bill, and my sister, Dori, for providing support and friendship even when they may have doubted that I would ever finish school. It's safe to say that I would not be writing this document had it not been for them.

Contents

List of Tables

List of Figures

Chapter 1

Introduction

According to the Standard Model of particle physics, matter is made up of six leptons and six quarks, These particles interact by exchanging bosons associated with the three fundamental forces: photons of the electromagnetic force; W and Z^0 bosons of the weak force; and gluons of the strong force. Quarks are bound together by the strong force into either quark-antiquark pairs called mesons or quark triplets called baryons. The familiar matter of the world is comprised of only a subset of these particles. The common baryons are the protons and neutrons that make up the nuclei of all atoms. The proton is made from two up quarks and a down quark, while the neutron is made from one up quark and two down quarks. The electron is the most well-known lepton, bound to the nuclei of atoms via the electromagnetic force. The weak force does not cause any binding of matter; it is responsible for mutation of one particle into another, such as occurs during radioactive decay.

The focus of this thesis is the Λ_c^+ baryon, a heavy cousin of the proton. The Λ_c^+ has a mass of $2.285\,\mathrm{GeV}/c^2$, nearly two and a half times heavier than the $0.938\,\mathrm{GeV}/c^2$ proton. The extra mass is due to the replacement of one of the proton's quarks with a charm quark. Because it is so much heavier than ordinary matter, the Λ_c^+ is unstable.

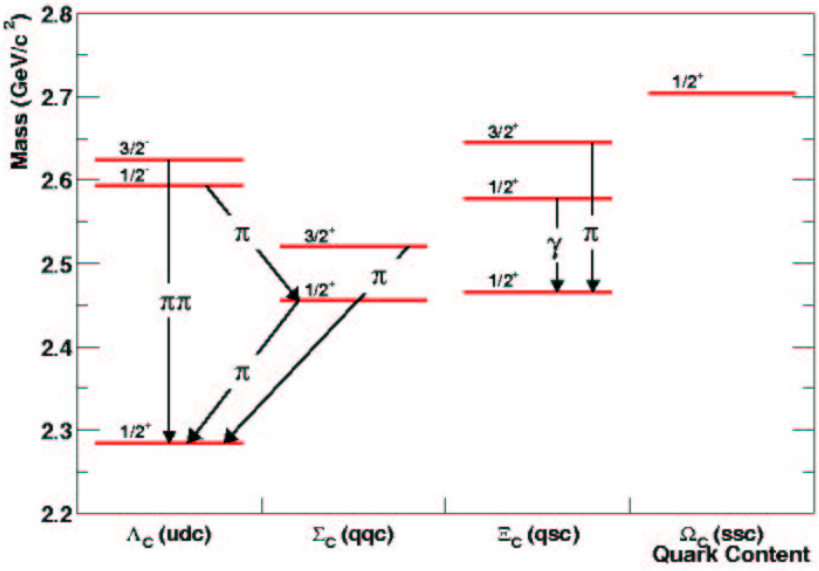

Figure 1.1: Mass spectrum for known baryons. Labels along the x-axis show the quark content of the baryon, with the ground and excited states denoted as horizontal red lines. The angular momentum J and parity P of each state is denoted as J^P. The dominant strong and electromagnetic decays are shown with black arrows. The lower case q is used to represent a light quark, either a u or a d. Baryons shown with no strong or electromagnetic transition do decay via the weak interaction.

The Λ_c^+ decays via the weak force with a lifetime of 200 fs [1].

In addition to the Λ_c^+, several other charm baryons have been discovered. Some are excitations of the ground state Λ_c^+, while others contain different combinations of the lighter u, d, and s quarks. Figure 1.1 shows the mass spectrum of the known charm baryons and their dominant strong and electromagnetic decays. All of the Λ_c^+-type and Σ_c-type baryons eventually decay to a Λ_c^+, so studies of these baryons is directly linked to understanding the ground state Λ_c^+.

Branching fractions are some of the most commonly measured quantities in high

energy physics experiments. Beyond the measurements of a particle's mass and lifetime, the more numerous branching fraction measurements provide much of the information we know about a particle. Of the fundamental absolute branching fractions that normalize charm hadron branching ratios, $\mathcal{B}(\Lambda_c^+ \to pK^-\pi^+)$ and $\mathcal{B}(D_s^+ \to \phi\pi^+)$ are the least precisely measured. Since the Λ_c^+ baryon appears in most decay chains of heavy baryons, an absolute measurement of $\mathcal{B}(\Lambda_c^+ \to pK^-\pi^+)$ is important for many studies of the heavy quark sector, from spectroscopy to B meson decays.

In addition to baryon studies, $\mathcal{B}(\Lambda_c^+ \to pK^-\pi^+)$ is essential in measuring the number of charm quarks produced in a data sample. Parameters of Quantum Chromodynamics (QCD), such as the quark masses and the renormalization cutoff scale, can be better determined with precise knowledge of the number of charm quarks produced per bottom quark decay. Higher order corrections in QCD can be tested by measuring the number of charm quarks produced per hadronic event at the Z^0 boson center-of-mass energy.

This thesis describes a determination of

$$\mathcal{B}(\Lambda_c^+ \to pK^-\pi^+) \cdot \frac{\mathcal{B}(e^+e^- \to c\overline{c} \to \Lambda_c^+ \; X)}{\mathcal{B}(e^+e^- \to c\overline{c} \to \Xi_c \; X) + \mathcal{B}(e^+e^- \to c\overline{c} \to \Xi_c \; X)} \tag{1.1}$$

using data collected with the *BABAR* detector at the Stanford Linear Accelerator Center. A model-dependent extraction of $\mathcal{B}(\Lambda_c^+ \to pK^-\pi^+)$ is then presented. Brief introductions to charm baryons and the *BABAR* detector are given first. Familiarity with the Standard Model of physics is assumed.

1.1 Charm Baryons

Charm baryons are those baryons containing a single charm quark and two other light quarks (u, d, or s). Baryons with two heavy quarks are predicted to exist and some

preliminary results from the SELEX experiment at FermiLab [2] indicate they have been seen. These "doubly charmed" baryons are rare and will be neglected in this discussion.

In a singly charmed baryon, the heavy charm quark ($m_c \sim 1.3\,\mathrm{GeV}/c^2$) is nearly motionless in the baryon's center-of-mass frame, with the lighter quarks traveling relativistically about it.

The light quarks are confined by QCD to lie within a sphere of radius Λ_{QCD}^{-1} since the strong coupling constant diverges at the scale $\Lambda_{QCD} \sim 0.57\,\mathrm{GeV}$. The quarks then can only exchange hard gluons with energies of order Λ_{QCD}. Since the charm mass is greater than Λ_{QCD} (the definition of "heavy"), it is relatively unaffected by the gluons, and thus decouples from the light quark degrees of freedom. Consequently, the system can be thought of as a light di-quark system bound to a spin-$\frac{1}{2}$ color source.

The charm baryon states with the lowest masses are those with no net orbital angular momentum. In this configuration, the light quarks can form either a singlet (antisymmetric) or triplet (symmetric) spin combination. The overall wave function of the baryon [3]

$$\psi = \psi(color)\psi(space)\psi(spin)\psi(flavor) \tag{1.2}$$

must be antisymmetric under the interchange of the light constituent fermions. Due to QCD confinement, hadrons must always appear as color singlets, so $\psi(color)$ is always an antisymmetric state. In addition, the $L = 0$ ground state is symmetric, which leaves $\psi(space)$ a symmetric state. Therefore, $\psi(spin)\psi(flavor)$ must be fully symmetric.

If the two quarks are in a spin-0 state, $\psi(spin)$ is asymmetric and therefore $\psi(flavor)$ must also be antisymmetric, leading to an isospin singlet called the Λ_c^+. If the two quarks are in a spin-1 state, $\psi(spin)$ is symmetric and $\psi(flavor)$ must

also be symmetric. This produces an isospin triplet called the Σ_c. Because the Σ_c di-quark has net spin, its color field interacts with the color field of the charm quark through spin-spin and spin-orbit interactions, elevating the Σ_c mass above the mass of the Λ_c^+. This is analogous to the fine-structure interaction in the hydrogen atom.

The motivation for measuring $\mathcal{B}(\Lambda_c^+ \to pK^-\pi^+)$ comes from the study of the interactions of heavy quarks. Since the two light quarks in a heavy quark baryon can be considered a single unexcited di-quark state, heavy quark baryons provide an arena to test Heavy Quark Effective Theory (HQET) without dealing with light degrees of freedom that have net spin or isospin.

The Λ_c^+ baryon plays a significant role in understanding both charm and bottom baryons. As the lightest charm baryon, the Λ_c^+ is common to many decays of the more massive baryons. The Σ_c states decay strongly through pion emission directly to Λ_c^+, as this is the only kinematically allowed strong decay. Baryons containing a bottom quark decay weakly to states including a charm baryon. It is through the decay to a Λ_c^+ that bottom baryons are most often detected. Therefore, the branching ratios of the bottom baryons depend on the $\mathcal{B}(\Lambda_c^+ \to pK^-\pi^+)$ measurements.

Charm baryons containing strange quarks, called Ξ_c and Ω_c, usually do not decay into Λ_c^+ baryons. The heavy charm quark decays before the strange quark can decay, leaving behind a system with two or more strange quarks. These systems are generally detected though reconstruction of a Ξ baryon and other decay products.

1.2 Branching Fractions

Branching fractions of weakly decaying particles are an indirect way to probe the strong and weak interactions. The strong force binds the quarks in the initial and final state hadrons and causes interactions among the final state particles. The weak force is responsible for the decay of the heavy quark in initial states that are stable

against decay via the strong or electromagnetic interactions. The ability to learn directly about the fundamental forces of nature from measured branching fractions is hindered by the detailed and difficult calculations required to form theoretical predictions.

A branching fraction is defined as $B_i = \frac{\Gamma_i}{\Gamma}$, where Γ_i is the partial decay rate for mode i and Γ is the sum of all the partial decay rates. Partial decay rates are sometimes theoretically calculable, but it is the branching fractions that are experimentally measurable. Once the lifetime τ of a particle is measured, decay rates and branching fractions can be compared using the relation $\tau = 1/\Gamma$.

It is often easier to measure the relative decay rate between two decay modes, both theoretically and experimentally. On the theoretical side, a calculation sometimes involves parameters whose values are not known with good precision. If an unknown parameter appears in the formulas for multiple decay rates, the parameter will cancel in a ratio of decay rates and the ratio can be calculated more precisely than an individual rate. Experimentally, a decay rate measurement often involves knowledge about the detector setup that is poorly understood, such as particle identification efficiency or acceptance correction. If two decay modes make use of particle identification and acceptance, uncertainties of these numbers will tend to cancel in a measurement of their decay rate ratio. Also, it is difficult to determine the absolute number of produced particles in an experiment. By measuring a decay rate ratio, this complication is avoided.

Though relative decay rates are easier to calculate and measure, measurements of at least one partial decay rate is needed to convert the ratios of decay rates to absolute decay rates. If all partial decay rates are measured for a particle, their sum should be the total decay rate. In the case of the τ lepton, this has nearly been realized. It is known that 30 observed decay modes account for 99.9% of τ decays. This is not true for many other particles, notably hadrons containing heavier (c or b) quarks. The D^0

and D^+ mesons both have approximately 100 measured decay modes, yet the sum of measured branching fractions is less than 70%. In the cases of the D_s^+ meson and the Λ_c^+ baryon, each has approximately 50 measured decay modes, but they only account for 50% of the total decay rate.

Many unseen decay rates can be estimated from the observed decay rates. Unfortunately, even using symmetry arguments to estimate unseen rates, the sum of the decay rates for charm hadrons is never equal to the full decay rate: the sum of the branching fractions is never precisely 100%. Figures 1.2-1.5 show the sum of all measured and inferred branching fractions for the D^0, D^+, D_s^+, and Λ_c^+ hadrons, respectively [4]. The figures illustrate that the sum of branching fractions is often substantially smaller or larger than 100%. In the case of D^0, the sum is 120%, whereas the sum for the Λ_c^+ is only 78%. The difference with 100% can be attributed to incorrect estimates for the unknown branching fractions or for the few measured branching fractions that are described next. The comparison is in stark contrast to the well understood sum of the τ branching fractions shown in Figure 1.6 [4].

Many of the measurements of charm hadron branching fractions are made relative to some known absolute branching fraction or to a more copious mode with an unknown branching fraction. The most common charm hadrons have many of their relative branching fractions tied to "standard candles." Standard candles are those absolute branching fractions that can be measured with small statistical error due to a large branching fraction and/or high efficiency of reconstruction. These standard candles of the most common charm hadrons have been measured [1]:

- $B(D^0 \to K^-\pi^+) = 0.0383 \pm 0.0009$ (2%)
- $B(D^+ \to K^-\pi^+\pi^+) = 0.0900 \pm 0.0060$ (7%)
- $B(D_s^+ \to \phi\pi^+) = 0.0360 \pm 0.0090$ (25%)

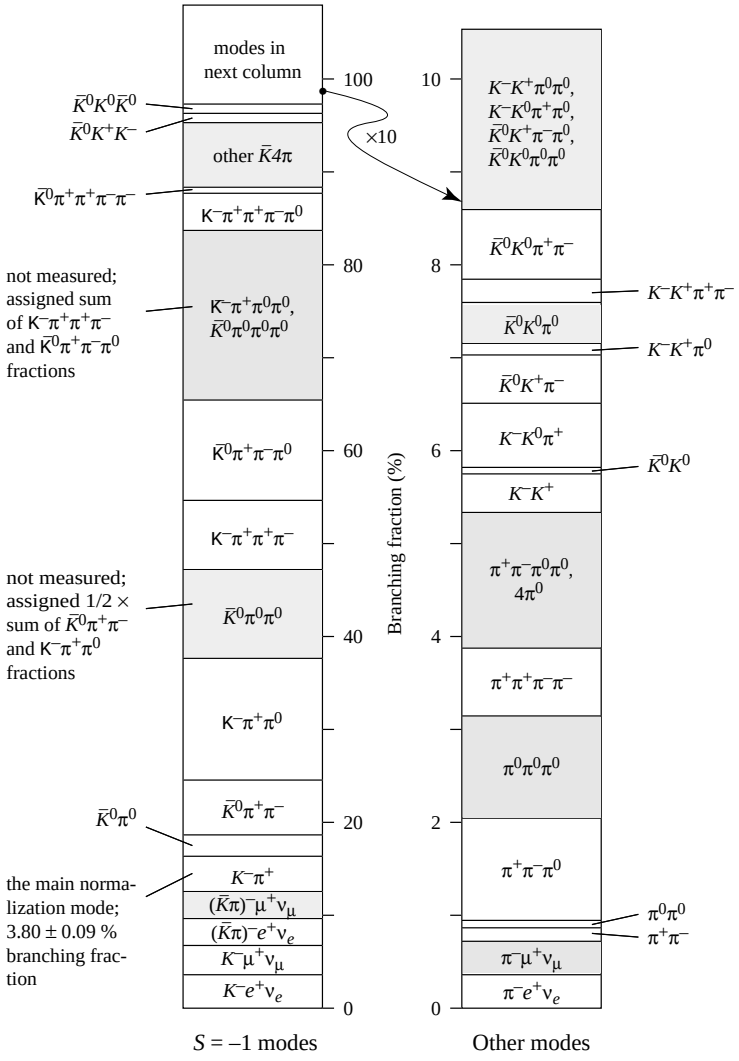

Figure 1.2: Branching fractions for the D^0 meson. Shaded regions have not been measured, but are set equal to the unweighted average of similar, measured modes [4].

- $B(\Lambda_c^+ \to pK^-\pi^+) = 0.050 \pm 0.013$ (25%)

The poorly known values for the D_s^+ and Λ_c^+ are readily apparent.

As the standard candle for the Λ_c^+ baryon, $\mathcal{B}(\Lambda_c^+ \to pK^-\pi^+)$ sets the scale for understanding many processes involving baryons, including $b \to c$ transitions, heavy quark fragmentation, and B decays to baryons. Reconstructing the decay $\Lambda_c^+ \to$

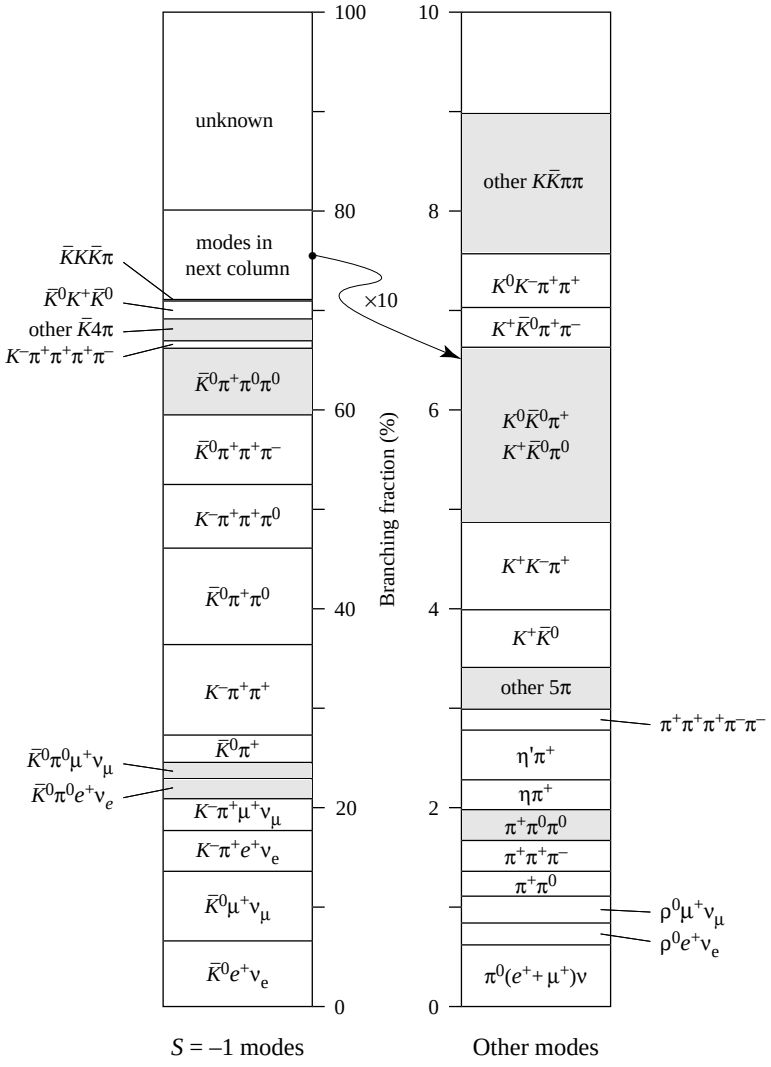

Figure 1.3: Branching fractions for the D^+ meson. Shaded regions have not been measured, but are set equal to the unweighted average of similar, measured modes [4].

$pK^-\pi^+$ is also the starting point for reconstructing many heavier charm and bottom baryons, since many can eventually decay through the Λ_c^+ baryon.

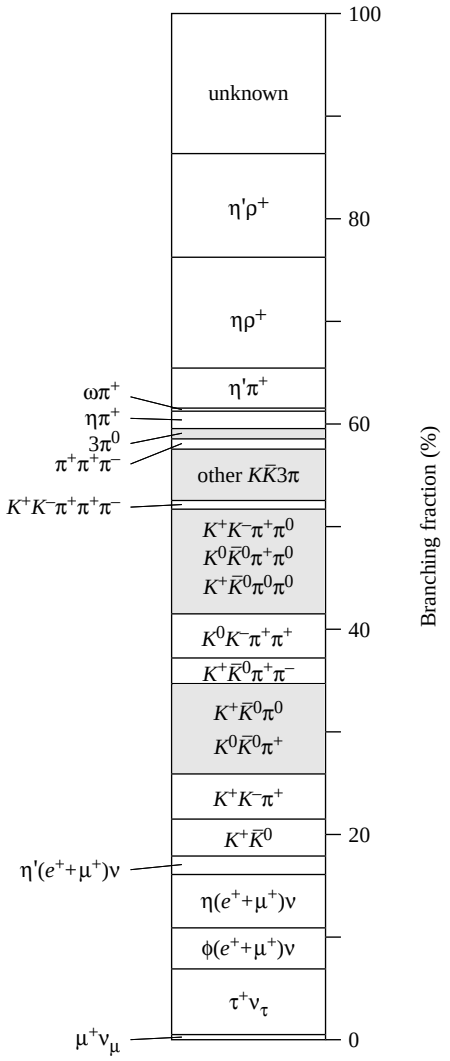

Figure 1.4: Branching fractions for the D_s^+ meson. Shaded regions have not been measured, but are set equal to the unweighted average of similar, measured modes [4].

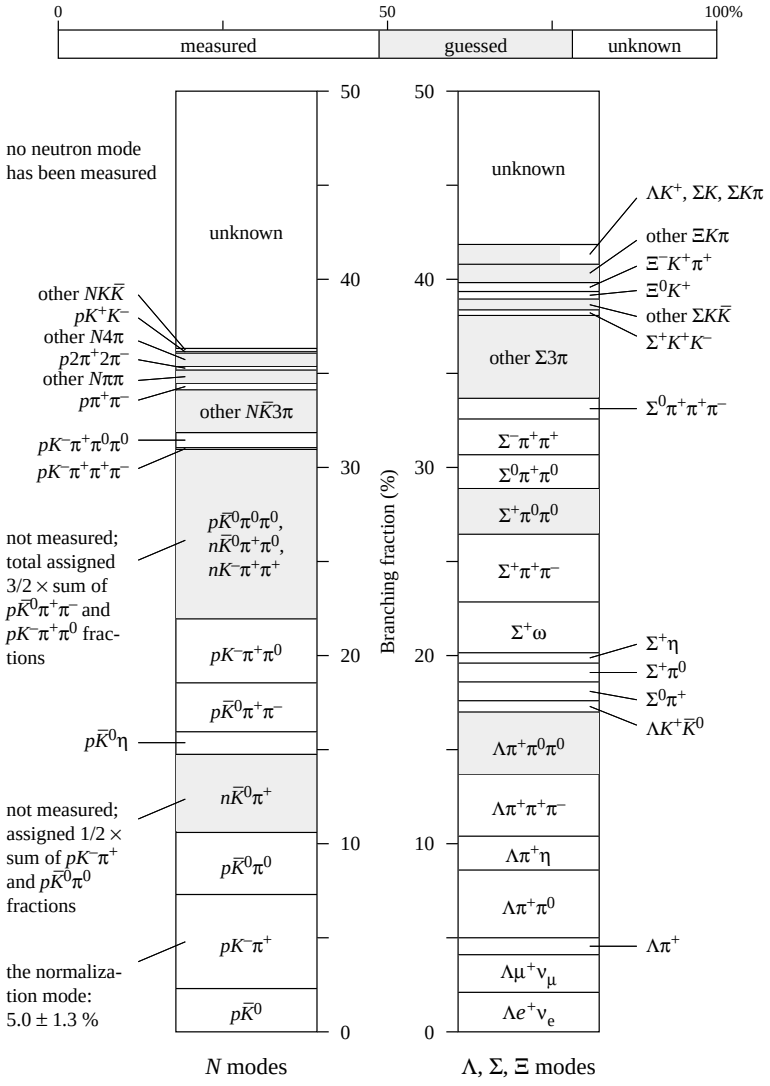

Figure 1.5: Branching fractions for the Λ_c^+ baryon. Shaded regions have not been measured, but are set equal to the unweighted average of similar, measured modes [4].

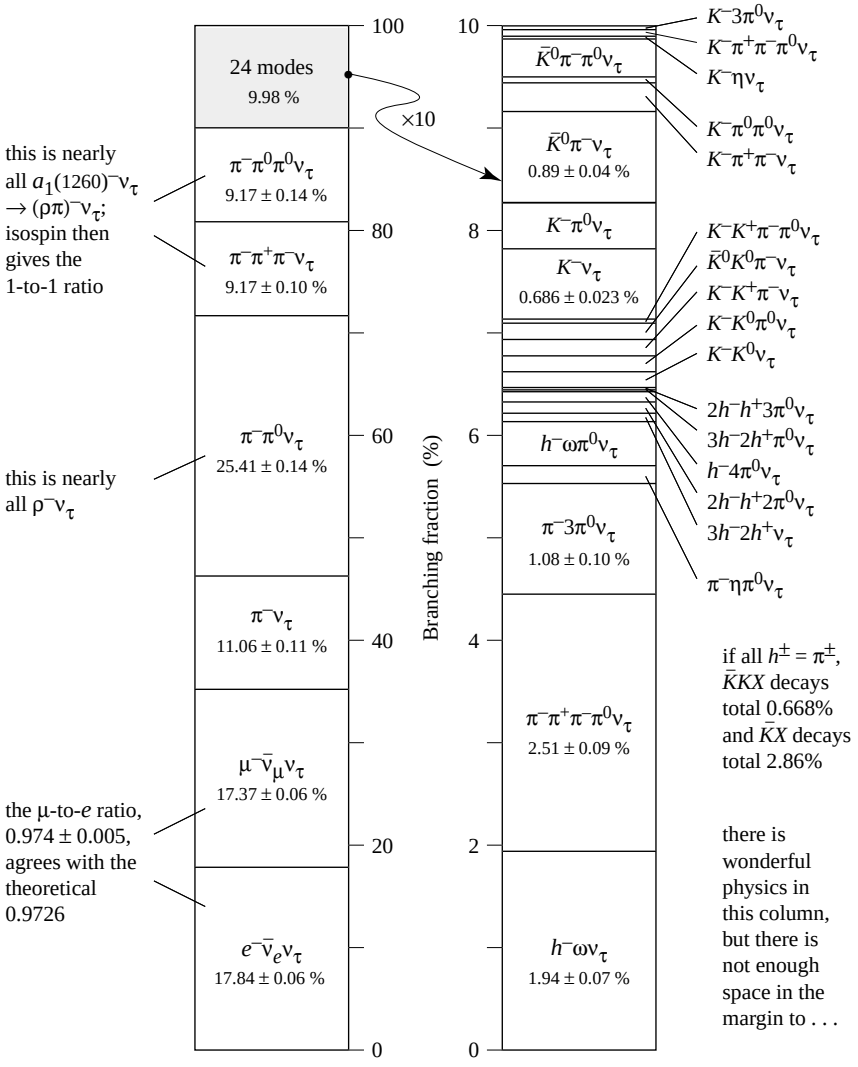

Figure 1.6: Branching fractions for the τ lepton. Six modes account for 90% of the decays, while 24 modes account for the remaining 10% [4].

1.3 Charm Counting

In addition to their use in the direct study of heavy baryons, the Λ_c^+ is also key in charm counting. Counting of charm quarks is important for two tests of the Standard Model. The first is the measurement of R_c, the ratio of charm quark production to total hadron production in e^+e^- annihilations at the Z^0 resonance. The second measurement related to charm counting is a determination of n_c, the average number of charm quarks produced in the decay of the bottom quark.

Having a good estimate of branching fractions allows one to deduce the true number of charm quarks in a data sample. An experiment will reconstruct the most common charm hadrons (D^0, D^+, D_s^+, and Λ_c^+) to their standard candle modes. The total number of charm quarks can be deduced by using the efficiency of reconstruction along with knowledge of the absolute branching fractions:

$$n_c = \sum_{i=D^0,D^+,D_s^+,\Lambda_c^+} \frac{N_i}{\varepsilon_{reco} \cdot B(i \to mode)} \tag{1.3}$$

The relative proportion of charm hadrons produced depends on the center-of-mass energy of the experiment, but it can be reasonably approximated as $N_{D^+} : N_{D^0} : N_{D_s^+} : N_{\Lambda_c^+} \approx 2.5 : 4 : 1.5 : 1$ at both the $\Upsilon(4S)$ and Z^0 center-of-mass energies. Given these ratios, it is easy to see how the poor knowledge of the D_s^+ and Λ_c^+ standard candle branching fractions translates into large systematic errors in counting charm quarks.

At the Z^0 center-of-mass energy, fermion production proceeds through a virtual photon or virtual Z^0 boson. Including interference effects, the cross section for quark

production at the Z^0 pole is [5]

$$\sigma(e^+e^- \rightarrow Z^0 \rightarrow Q\overline{Q}) = \frac{\beta s G_F^2 M_Z^2 (1 - 4sin^2\theta_w + 8sin^4\theta_w)}{4\pi[(s - M_Z^2)^2 + \Gamma_Z^2 M_Z^2]}[2g_V^2(3 - \beta^2) + 4g_A^2\beta^2], \tag{1.4}$$

where β is the velocity of the quarks, s is the center-of-mass energy squared, G_F is the Fermi coupling constant, M_Z is the Z^0 mass, θ_w is the Weinberg weak mixing angle, and g_V and g_A are the weak vector and axial-vector coupling strengths.

Higher-order QCD and loop corrections modify both the Z^0 field self-energy and the vertex strength. Calculations to two-loops have been undertaken for heavy quark production, giving [6]

$$R_c^{SM} = \frac{\sigma(e^+e^- \rightarrow Z^0 \rightarrow b\overline{b})}{\sigma(e^+e^- \rightarrow Z^0 \rightarrow u\overline{u}, d\overline{d}, s\overline{s}, c\overline{c}, b\overline{b})} = 0.1719 \pm 0.0017 \tag{1.5}$$

Experiments at LEP have measured R_c to be

- $0.1738 \pm 0.0047(stat) \pm 0.0088(sys) \pm 0.0075(BR)$ (ALEPH) [7],
- $0.1665 \pm 0.0051(stat) \pm 0.0061(sys) \pm 0.0054(BR)$ (DELPHI) [8].

Both experiments separately list the systematic error due to uncertainty in the charm hadron branching fractions in order to emphasize the significant contribution from this systematic uncertainty. ALEPH and DELPHI count hadrons using the standard candle modes, as described earlier. DELPHI also uses a method in which D^* mesons are reconstructed and fragmentation models are used to determine the number of charm mesons. DELPHI's combination of methods leads to a smaller dependence on the absolute branching fractions.

To measure n_c, a sample of bottom quarks is isolated and the number of charm quarks produced is determined. Charm quarks are produced through the weak decay of a bottom quark, both directly from the bottom quark transition ($b \rightarrow Wc$) and

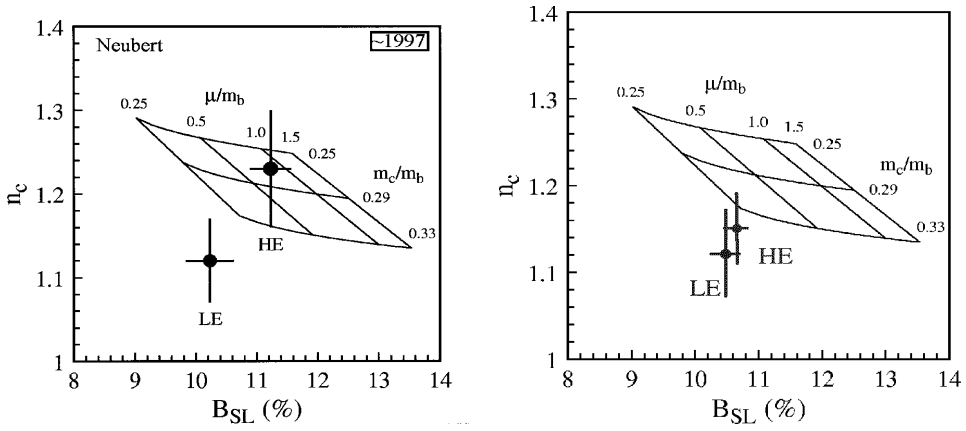

(a) Situation in 1997

(b) Situation in 1999

Figure 1.7: Theoretical predictions and experimental results for the number of charm quarks in bottom hadron decays and the inclusive semileptonic branching fraction [9, 10]. The grid shows the theoretical "comfort zone," as described by Neubert [9]. Experimental points are for experiments at the $\Upsilon(4S)$ resonance (LE) and the Z^0 resonance (HE).

from the decay of the W boson (e.g, $W \to cs$). When the bottom quark decays directly to an up quark or decays via a penguin diagram, it is possible for no charm quark to result.

When combined with the inclusive semileptonic branching fraction of bottom meson, n_c provides constraints on theoretical models. These quantities can be related to the ratio of charm quark to bottom quark masses and the ratio of the renormalization scale to the bottom quark mass [9]. In recent years, increasingly precise experimental measurements of the inclusive semileptonic branching fraction and n_c at different center-of-mass energies have shown discrepancies with each other and with theoretical models [8]. Figure 1.7 shows the results for experiments at the $\Upsilon(4S)$ and Z^0 resonances, along with the theoretical "comfort zone."

In addition to charm counting, a measurement of the $\Lambda_c^+ \to pK^-\pi^+$ branching fraction can be used to test theoretical predictions for the rate $\Gamma(\Lambda_c^+ \to pK^-\pi^+)$.

While this may be true, no theorist has attempted such a prediction. Calculations involving nonperturbative QCD are still extremely complicated, and a three-body decay mode computation is well beyond the realization of theorists with modern-day tools. The tests of theoretical predictions provided by this measurement are only indirect: through normalization fixing and charm counting as discussed previously.

1.4 Previous Studies

The importance of $\mathcal{B}(\Lambda_c^+ \to pK^-\pi^+)$ in the study of heavy quarks means that it requires attention, and it has already been the focus of three major classes of studies.

In the first class of analysis, the ratio $\frac{\mathcal{B}(\Lambda_c^+ \to pK^-\pi^+)}{\mathcal{B}(\Lambda_c^+ \to \Lambda^0 X l^+ \nu)}$ is measured. The branching fraction $\mathcal{B}(\Lambda_c^+ \to \Lambda^0 X l^+ \nu)$ is estimated from the semileptonic decay rate of the D meson using the following equation:

$$\mathcal{B}(\Lambda_c^+ \to \Lambda^0 X l^+ \nu) = \frac{\Gamma(D \to X l^+ \nu_l)}{1 + |\frac{V_{cd}^2}{V_{cs}^2}|} \cdot \tau_{\Lambda_c^+} \cdot T, \tag{1.6}$$

where the correction factor T is given by

$$T = \frac{\mathcal{B}(\Lambda_c^+ \to \Lambda l^+ \nu_l)}{\mathcal{B}(\Lambda_c^+ \to X_s l^+ \nu_l)} \cdot \frac{\Gamma(\Lambda_c^+ \to X_s l^+ \nu_l)}{\Gamma(D \to X_s l^+ \nu_l)}. \tag{1.7}$$

Both terms contributing to T are theoretically estimated to be near 1.0. Unfortunately, the errors on the theoretical estimates of T are quite large, leading to a large systematic uncertainty on the final estimation of $\mathcal{B}(\Lambda_c^+ \to pK^-\pi^+)$.

The second class of $\mathcal{B}(\Lambda_c^+ \to pK^-\pi^+)$ analysis involves studying Λ_c^+ baryons resulting from the decays of B mesons. In this type of analysis, the product of branching fractions $\mathcal{B}(\overline{B} \to \Lambda_c^+ X) \cdot \mathcal{B}(\Lambda_c^+ \to pK^-\pi^+)$ is measured [11, 12]. Using the assumption that $\mathcal{B}(\overline{B} \to baryons) = \mathcal{B}(\overline{B} \to \Lambda_c^+ X)$, a measurement of $\mathcal{B}(\overline{B} \to baryons)$ is

also performed [13, 12]. From these two results, $\mathcal{B}(\Lambda_c^+ \to pK^-\pi^+)$ is estimated to be $(4.14 \pm 0.91)\%$ [1]. The assumption that all baryonic decays of B mesons contain a Λ_c^+ rests on two additional statements: (1) all B meson decays to baryons contain a charmed baryon, and (2) all B meson decays to charm baryons result in a Λ_c^+.

The first statement is challenged by a recent CLEO measurement [14] of $\mathcal{B}(B^0 \to D^{*-}p\overline{p}\pi^+) = (0.65^{+0.13}_{-0.12} \pm 0.10) \times 10^{-3}$ and $B(B^0 \to D^{*-}p\overline{n}) = (1.45^{+0.34}_{-0.30} \pm 0.27) \times 10^{-3}$. This is the first observation of a D meson accompanying a baryonic B decay. If one also allows the possibility of comparable branching fractions for similar decays with additional pions and other D mesons, it is clear that a non-negligible number of B decays to baryons do not contain a charm baryon. The second statement is challenged by two observations. First, the current world average $\mathcal{B}(B \to \bar{\Sigma}_c^{--}\, X) = (4.2 \pm 2.4) \times 10^{-3}$ demonstrates the possibility of non-Λ_c^+ charm baryons in B decays. Second, theoretically it has been calculated [15] that the contribution of Ξ_c and Ω_c baryons relative to Λ_c^+ will be appreciable.

A third alternative has been proposed by theorist Isi Dunietz [16], and is the model used in this thesis. It requires a large data sample, so it is ideal for a high-luminosity B factory operating at the $\Upsilon(4S)$. The method uses only $c\overline{c}$ events, so B meson events have to be rejected by requiring the charm hadron momentum to be above the kinematic threshold for charm hadrons from B decays. A Λ_c^+ is assumed to be produced when a $\overline{D}$ meson and an $\overline{p}$ are produced. A sufficient understanding of the backgrounds can be obtained from data to allow a model-independent determination of $\mathcal{B}(\Lambda_c^+ \to pK^-\pi^+)$.

An analysis by CLEO with an integrated luminosity of $4.7\,\mathrm{fb}^{-1}$ uses this method to measure $\mathcal{B}(\Lambda_c^+ \to pK^-\pi^+)$. While CLEO's measurement is consistent with other measurements, it is dominated by its systematic error, giving a result of $(5.0 \pm 0.5 \pm 1.2)\%$ [17]. Like CLEO, the PEP-II/*BABAR* experiment is well suited for using this new method. In the case of PEP-II/*BABAR*, higher luminosity reduces the statistical

errors and allows better background and selection studies to improve the systematic uncertainties.

1.5 Nomenclature

Charge conjugate states are always implied throughout this thesis, unless specifically mentioned otherwise in the text. When referring to generic D mesons, the three weakly decaying mesons, D^0, D^+, and D_s^+, are implied. The thrust axis, used to divide an event into hemispheres, is calculated using only charged tracks, and the symbol "$\Longleftrightarrow$" is used to separate particles reconstructed in different event hemispheres. All fits are performed using RooFit [18] and are unbinned extended maximum likelihood fits.

1.6 Analysis Overview

An absolute branching fraction measurement for $\Lambda_c^+ \to pK^-\pi^+$ requires knowledge of the number of Λ_c^+ baryons produced and the number of $\Lambda_c^+ \to pK^-\pi^+$ decays that occur. To count Λ_c^+ baryons, events are selected in which an $\overline{p}$ (called the tag) is found to conserve baryon number, and a $\overline{D}$ meson is found to conserve charm. To ensure all $\overline{c}$ quarks are counted, all flavors of $\overline{D}$ meson ($\overline{D}^0$, D^-, and D_s^-) need to be reconstructed. In order to reduce the probability that the $\overline{p}$ has come from a charm baryon, the $\overline{p}$ is required to appear in the same hemisphere of the event as the Λ_c^+; i.e., "$\overline{p}\Lambda_c^+ \Longleftrightarrow \overline{D}$". To eliminate the contamination of hadrons from B meson decays, the $\overline{D}$ or the Λ_c^+ is required to have momentum greater than 2.5 GeV.

The final configuration of the production model can be seen in Figure 1.8(a). In all figures of this section, particles that are not reconstructed are depicted with dashed lines. Neglecting backgrounds, the number of produced Λ_c^+ baryons is the number of

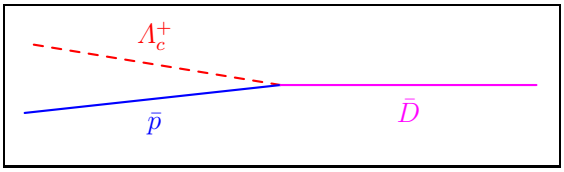

(a) Production Model

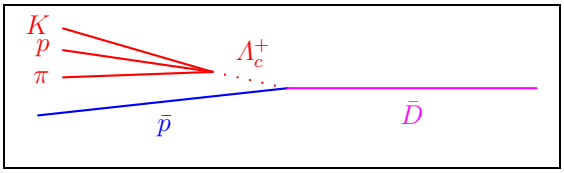

(b) Decay Model

Figure 1.8: Event topologies used in this analysis. (a) When "$\overline{p} \Longleftrightarrow \overline{D}$" is detected, an unobserved Λ_c^+ may be produced in the $\overline{p}$'s hemisphere. (b) The fraction of events that also contain a $\Lambda_c^+ \to pK^-\pi^+$ in the $\overline{p}$'s hemisphere gives $\mathcal{B}(\Lambda_c^+ \to pK^-\pi^+)$.

"$\overline{p} \Longleftrightarrow \overline{D}$" events, shown in Figure 1.8(a). The fraction of these events containing $\Lambda_c^+ \to pK^-\pi^+$ in the same hemisphere as the $\overline{p}$ tag, shown in Figure 1.8(b), estimates the absolute branching fraction.

The majority of the events in Figure 1.8(a) do contain a Λ_c^+, though some backgrounds can contribute at a low level. The largest source of background is when a nucleon–D-meson pair or a Ξ_c baryon is created instead of a Λ_c^+, as shown in Figure 1.9.

In order to understand $\overline{p}D \Longleftrightarrow N\overline{D}$ backgrounds, "$\overline{p}D \Longleftrightarrow X$" candidates are selected with a topology shown in Figure 1.9(a). These events are likely to contain a $\overline{D}$ meson, since creating an anti-charm baryon instead would result in the highly unlikely event with two anti-baryons, two baryons, and a D meson.

The cleanest method to detect the $\overline{D}$ meson is to fully reconstruct it. However, full reconstruction severely limits the number of events due to the small efficiency for

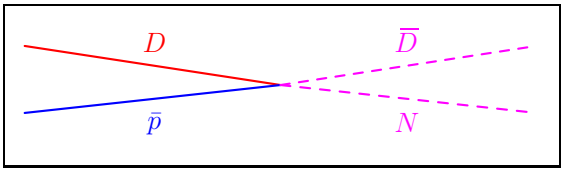

(a) nucleon–D-meson pair

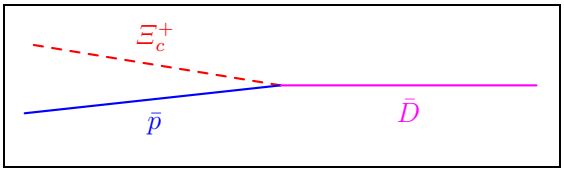

(b) Ξ_c baryon

Figure 1.9: Two sources of background in the Λ_c^+ production model. Instead of a Λ_c^+, a nucleon-D pair (a) or a Ξ_c baryon (b) is formed. Events in (a) can be efficiently detected by reconstructing the $\overline{p}$ and D meson in the same hemisphere. Events in (b) cannot be differentiated from those shown in Figure 1.8(a) and represent undetectable backgrounds to the estimate of produced Λ_c^+ baryons.

fully reconstructing D mesons. To bolster statistics, the requirement of detecting a $\overline{D}$ when reconstructing a Λ_c^+ is released. Rejecting $B\overline{B}$ is still accomplished by requiring the Λ_c^+ to have a center-of-mass momentum greater than 2.5 GeV. Figure 1.10 shows the configuration for the full D reconstruction method. The drawback of this method is that events with a Λ_c^+-$\overline{\Lambda}_c^-$ pair can be selected, as shown in Figure 1.11. Since these events are not part of the assumed production mechanism, this will cause an overestimation of the branching ratio and an appropriate correction must be made.

Using full reconstruction of a D meson, the final branching fraction can be calculated using the following equation:

$$\mathcal{B}(\Lambda_c^+ \to pK^-\pi^+) = \frac{N(\overline{p}\Lambda_c^+ \to pK^-\pi^+ \Longleftrightarrow) - N(\overline{p} \Longleftrightarrow \overline{\Lambda}_c^- \to \overline{p}K^+\pi^-)}{N(\overline{p} \Longleftrightarrow \overline{D}) - N(\overline{p}D \Longleftrightarrow)}. \quad (1.8)$$

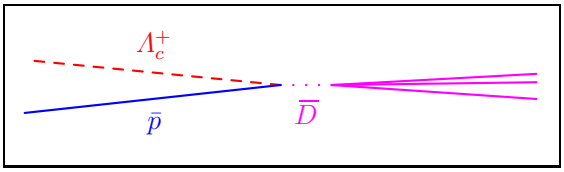

(a) Fully reconstructed $\overline{D}$ meson

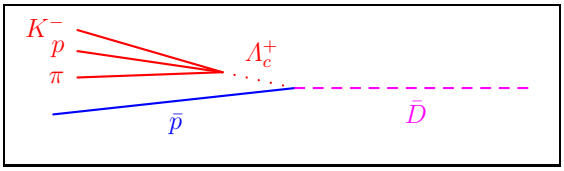

(b) Fully reconstructed Λ_c^+ baryon

Figure 1.10: A "$\overline{p} \Longleftrightarrow \overline{D}_{reco}$" event (a) is used to flag potential Λ_c^+ production, and a "$\overline{p}\Lambda_c^+ \rightarrow pK^-\pi^+ \Longleftrightarrow$" event (b) is used to flag Λ_c^+ decay to $pK^-\pi^+$ within the assumed production model. The $\overline{D}$ meson is not reconstructed in events in (b), leading to additional backgrounds shown in Figure 1.11.

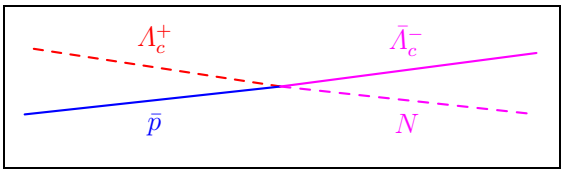

Figure 1.11: In order to estimate the amount of $\overline{p}\Lambda_c^+ \Longleftrightarrow N\overline{\Lambda}_c^-$ contamination in the sample of "$\overline{p}\Lambda_c^+ \rightarrow pK^-\pi^+ \Longleftrightarrow$" candidates, events with the topology shown, "$\overline{p} \Longleftrightarrow \overline{\Lambda}_c^- \rightarrow \overline{p}K^+\pi^-$", are selected.

Of particular importance is the fact that the result is in the form of a ratio, so that many systematic effects will tend to cancel. For example, each event type requires an $\overline{p}$ to be selected, so any uncertainty in the $\overline{p}$ selection efficiency will be mitigated in the ratio. Additionally, many reconstruction errors will be reduced since all event

types have similar number of tracks and reconstruction methods.

The next chapter describes the components that make up the *BABAR* detector used to collect the data for this analysis. Following the detector description, Chapters 3 and 4 present the tracking and particle identification techniques used in the analysis. Chapter 5 provides a more detailed description of the analysis procedure, and Chapter 6 presents a validation of the procedure on Monte Carlo simulation. Chapters 7 and 8 give the final results and an analysis of the systematic errors on the results. The final chapter discusses the results and their ramifications.

Chapter 2

The PEP-II B Factory and the *BABAR* Detector

The design of the *BABAR* detector and the PEP-II storage rings is uniquely optimized to study CP violation in the decays of neutral B mesons at the $\Upsilon(4S)$ resonance. The PEP-II storage rings are designed asymmetrically in order to give a boost to the produced B mesons. The boost dilates the observed decay time of the mesons, allowing a relative decay time measurement that would not exist if the B meson were produced at rest. To insure high acceptance in the boost direction, the *BABAR* detector also includes an asymmetric design. Figure 2.1 shows the design of the detector. The detector region in the boost direction is called the forward region, while the region opposite the boost is referred to as the backward region. Figure 2.2 shows the effect of the boost on acceptance. Because of the compression of the center-of-mass acceptance to the forward direction, the detector is designed with a concentration of active material in that direction. Many of the non-active detector elements are located in the backward region, where acceptance in the laboratory frame is less crucial. While the boost is necessary for precision B meson studies, it has no

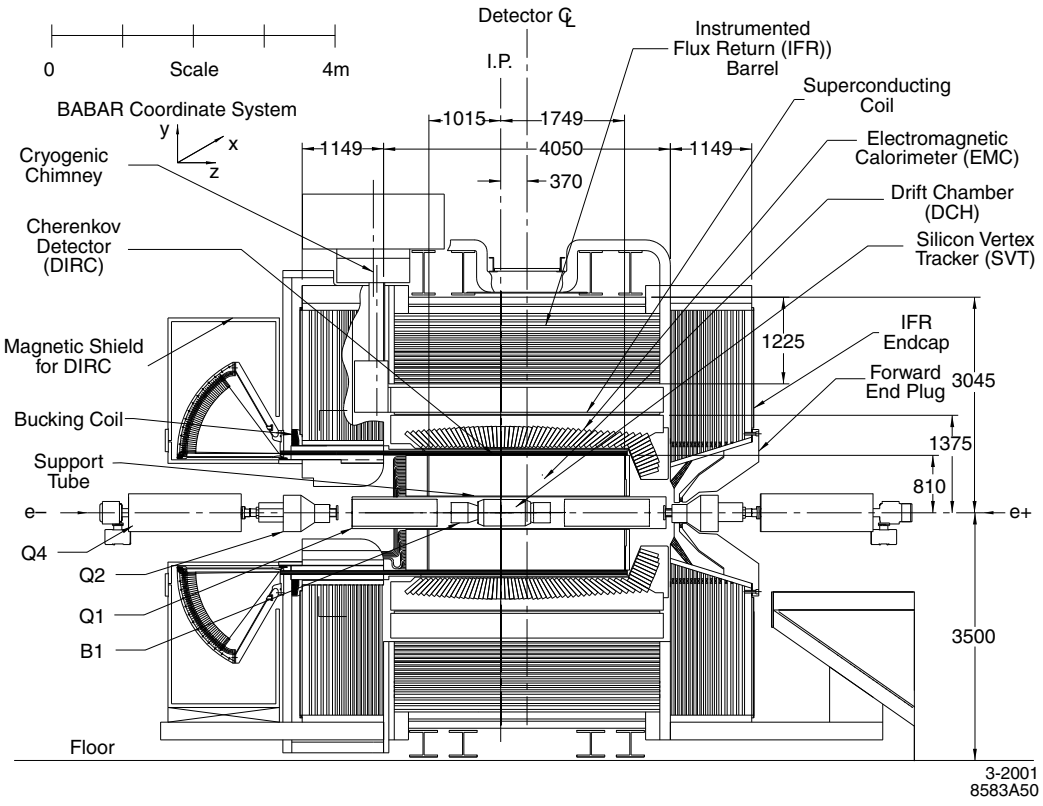

Figure 2.1: Scale drawing of the *BABAR* detector, showing the locations of the sub-detectors, supports, and nearby accelerator magnets.

advantages for charm physics. The use of a boost negatively impacts the study of charm meson lifetimes and restricts the detector acceptance for all studies.

In addition to the physical layout of the storage rings and detector, high quality detector design and fabrication are important. A silicon detector, drift chamber, and 1.5T superconducting solenoid magnet allow precise reconstruction of B meson decays. Particle identification, provided by $\mathrm{d}E/\mathrm{d}x$ measurements and an excellent quartz Cerenkov ring detector, is important for tagging the B meson flavors and reducing physics backgrounds.

Since the decays of neutral B mesons to CP eigenstates are extremely rare, a large

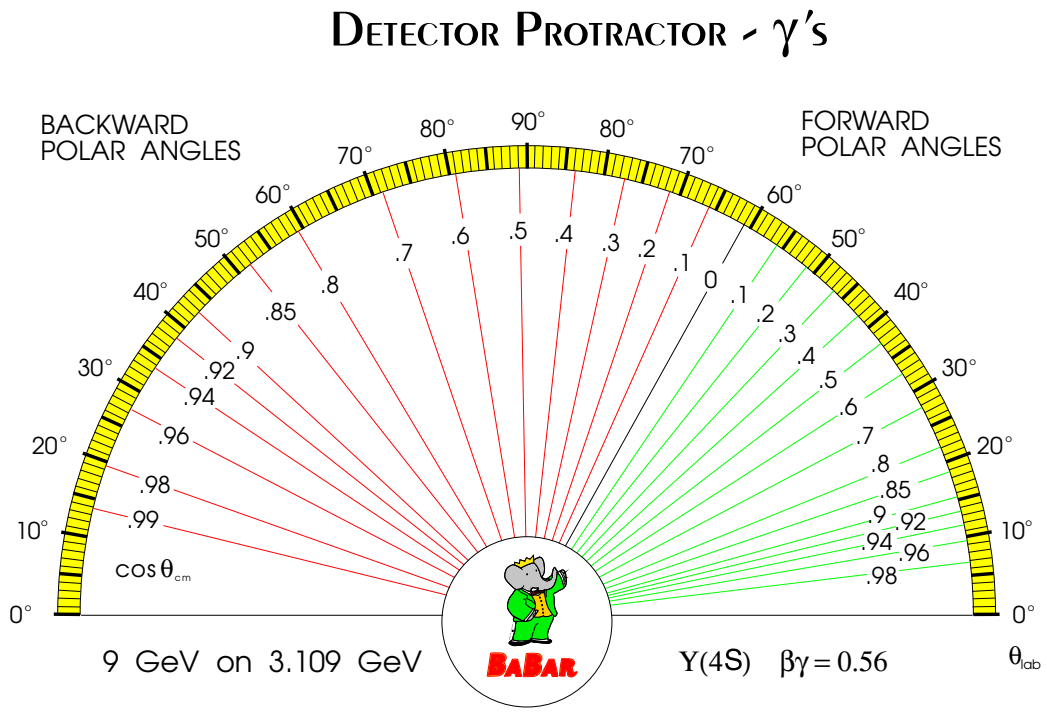

Figure 2.2: Relationship between center-of-mass and *BABAR* laboratory polar angles for massless particles.

sample of data must be collected to perform statistically significant experiments. The PEP-II storage rings and interaction region were engineered specifically to handle the large beam currents necessary for generating many B mesons for study. The design luminosity of PEP-II was $3 \times 10^{33}\,\mathrm{cm}^{-2}\,\mathrm{s}^{-1}$, a value that was attained on October 26, 2000 and was doubled on May 2, 2003. Figure 2.3 shows the integrated luminosity recorded by *BABAR* for the data collecting period covered in this analysis.

All of the optimizations for studying CP violation also permit high precision charm physics, non-CP B meson physics, τ physics, and two-photon physics. This thesis is dedicated to the study of the Λ_c^+ baryon, taking advantage of the large sample of charm baryons provided by the high luminosities of PEP-II.

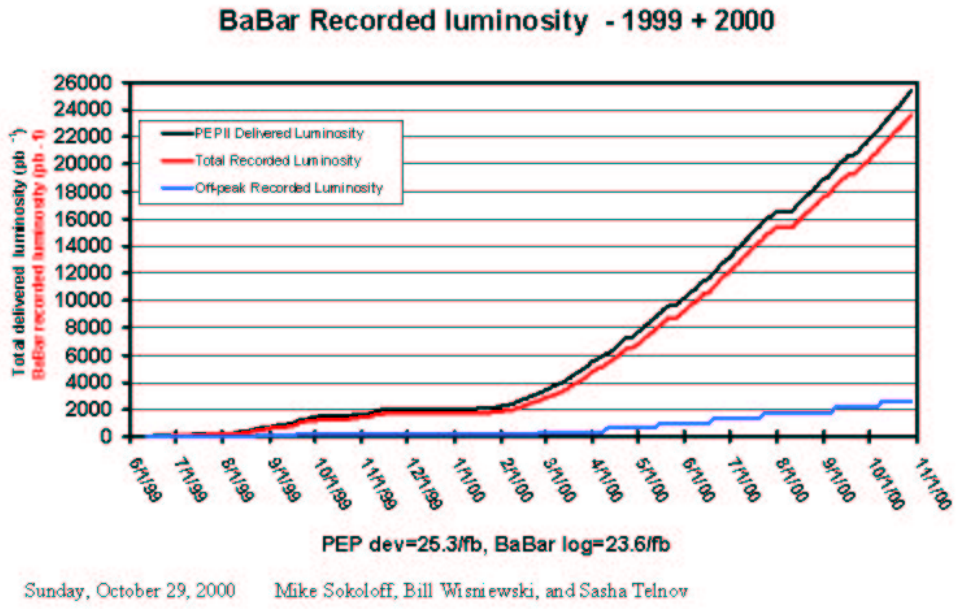

Figure 2.3: Luminosity for the period Oct 1999 through Dec 2001.

2.1 PEP-II

The PEP-II facility, completed in 1998, consists of two independent storage rings stacked one on top of the other in a tunnel with 2.09 km circumference. The rings are independent so that particles in each ring feel different magnetic field strengths. This design allows the rings to guide particles with different momenta. The low-energy ring is planned to carry 2.1A of 3.1- GeV positrons, while the high-energy ring stores up to 0.75A of 9- GeV electrons. PEP-II is designed to maintain up to 1658 bunches of electrons and positrons, spaced at 1.26 m around the rings to give a bunch crossing time of 4.2 ns. The beams are injected using the low-emittance SLC beams via special bypass lines.

The interaction region, shown in Figure 2.4, is a complicated structure constrained by many engineering and physics requirements. Bringing together two beams of particles of different energies requires a complex arrangement of magnets. The final bending and focusing magnets (B1 and QD1) must be extremely close to the interaction region to be able to direct the beams head-on into each other, then separate them into their independent beam pipes. Because the region occupied by these magnets, especially the forward region, is also important for physics purposes, the magnets were not made superconducting to save room.

2.2 Silicon Vertex Tracker

The main purpose of the Silicon Vertex Tracker (SVT) is to provide precise vertex reconstruction, with an average resolution below 80 μm. The SVT consists of 5 layers of silicon microstrip detector wafers arranged in cylindrical-shaped pattern around the beampipe, as shown in Figure 2.5. The inner three layers are at radii of 3.3 cm, 4.0 cm, and 5.9 cm, giving crucial position information near the interaction point. The outer two layers are at radii of 12.7 cm and 14.6 cm, providing information at larger distances while keeping material to a minimum.

In addition to vertex reconstruction, the SVT is important for charged-particle tracking. For tracks with $40\,\mathrm{MeV}/c < p_T < 100\,\mathrm{MeV}/c$, the SVT provides stand-alone tracking. For tracks with $p_T > 100\,\mathrm{MeV}/c$, the SVT is used in conjunction with the the Drift Chamber (see Section 2.3).

The silicon wafers are 300 μm thick, reflecting a trade-off between minimizing the multiple scattering and generating a discernible signal. The pitch of the strips varies between 50-100 μm. A charged particle incident normally to a wafer will create 24,000 electron-hole pairs on average, or 3.6 fC. Particles at other angles will create larger signals, but will also traverse multiple neighboring strips. Both the signal size and

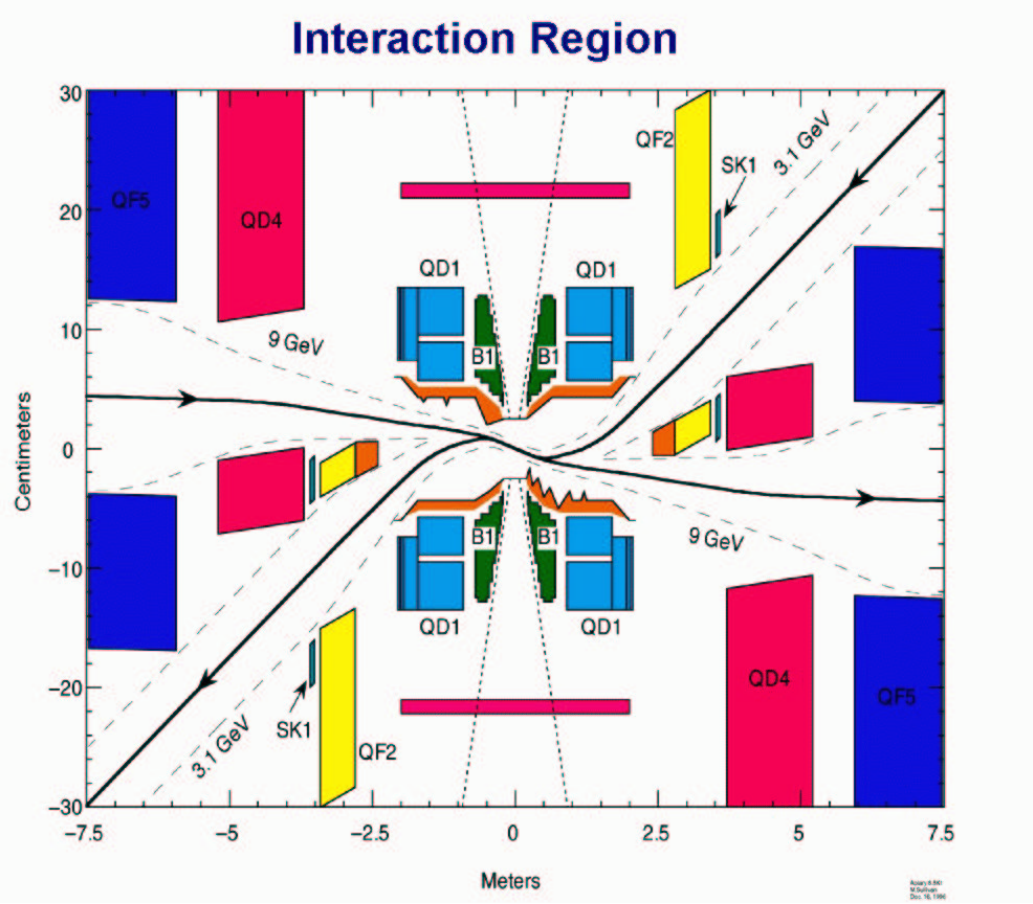

Figure 2.4: Schematic of the PEP-II interaction region where *BABAR* is built. Shown is the complicated arrangement of bending and quadrapole (starting with "B" and "Q", respectively) magnets which bring together the low- and high- energy beams. Engineering was a trade-off between increasing *BABAR*'s acceptance, lowering the crossing angle, and minimizing radiation exposure of the sensitive detector materials.

the pattern of hits are used for tracking calculations. Figure 2.6 shows the resolution of hits on a reconstructed track for the innermost SVT layer.

The data acquisition system records both the time and size of the charge deposition, provided it is larger than 0.4 fC. There are a total of 52 double-sided silicon

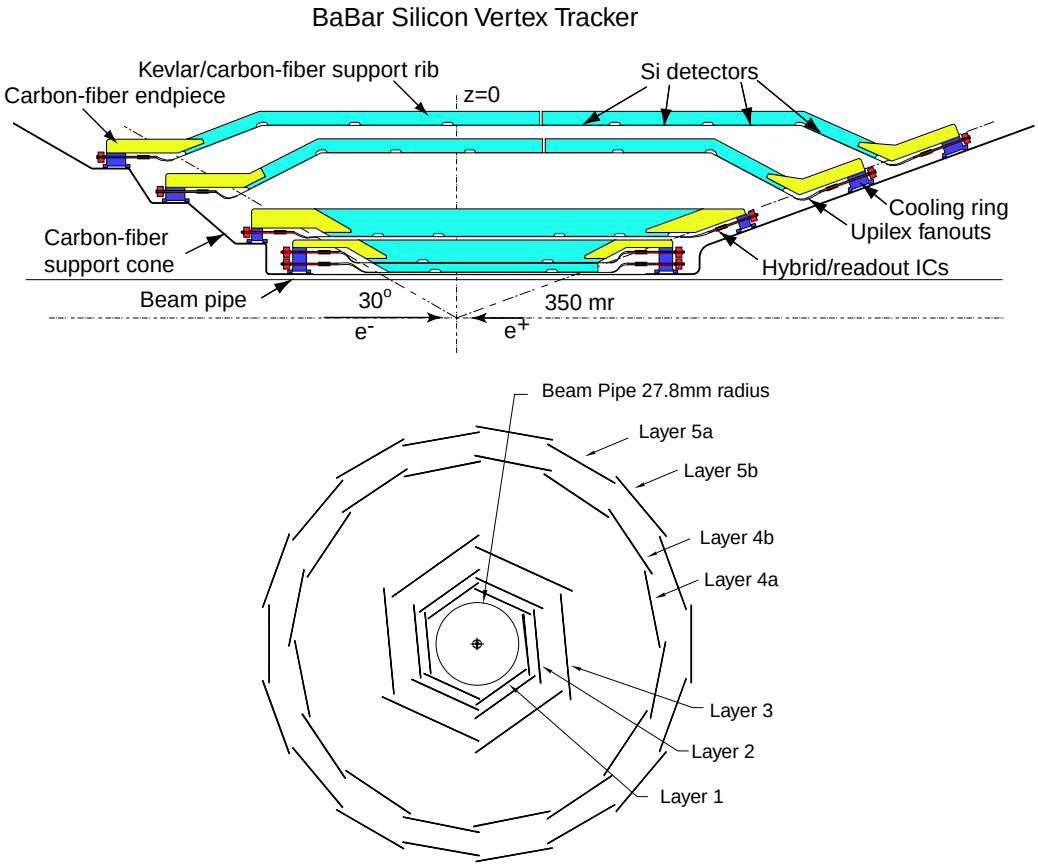

Figure 2.5: Z (top) and r-ϕ (bottom) views of the SVT wafers.

modules with approximately 150,000 AC-coupled readout channels. Signals are digitized on the detector and stored in buffers until a signal comes from the trigger to indicate an interesting event.

A hit is registered if a channel goes above threshold within the 6.3 μs of an event. The 0.4 fC thresholds are adjusted on a chip by chip basis in order to maximize efficiency of detecting a particle while keeping occupancy due to random noise at a minimum. Thresholds are set to allow 0.5-3.0% occupancy. High occupancy increases the combinatorics of the track find algorithms (see Section 3).

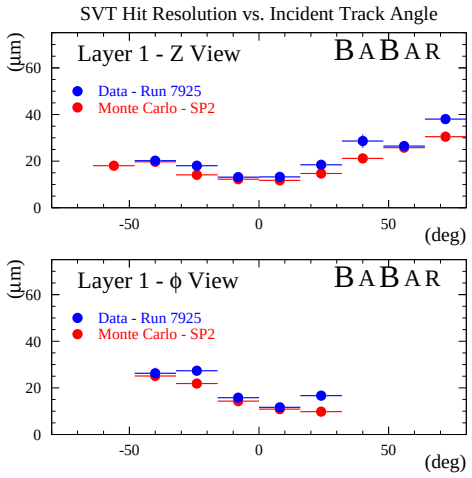

Figure 2.6: Measured resolution of SVT hits as a function of incident track angle with respect to the wafer normal. Residuals for the innermost layer in both z (upper) and phi (lower) wafers are shown in blue. Monte-Carlo, using perfect detector alignment, is overlaid in red.

Being only centimeters from the beampipe, the inner SVT layers are exposed to high levels of radiation. This radiation is detrimental to the performance of both the bulk detector and the on-detector electronics. The silicon used for the detector and the electronics is radiation hard, built to withstand an average 10 krad dose (100 krad in the most exposed areas).

To protect and monitor the system, PIN diodes have been placed just outside the detector acceptance but close to the silicon itself. These diodes are read out using two complementary electronics systems. The first system is a fast readout, which measures the instantaneous radiation levels near the detector. The fast system aborts PEP-II operations whenever levels become too high. The second system is a slow readout which logs average radiation dose over long periods of time. The slow readout system provides feedback to PEP-II operations on the longer-term effects of their operations decisions.

2.3 Drift Chamber

The Drift Chamber (DCH) is the main tracking system for *BABAR*. It is 275 cm in length and spans radially from 22.5 cm to 80 cm. The DCH provides efficient tracking for charged particles with $p_T > 120\,\mathrm{MeV}/c$, as well as $\mathrm{d}E/\mathrm{d}x$ information for particle identification.

The DCH is comprised of approximately 30,000 wires arranged into more than 7,100 hexagonal 1.2×1.9 cm drift cells. The hexagon is formed by a set of 6 gold-plated aluminum field wires, all set to a voltage of approximately 1900V. In the center of each cell is a gold-plated tungsten-rhenium sense wire.

The cells are arranged into 40 cylindrical layers, grouped into sets of four to form 10 super-layers. Each super-layer contains from 96 to 256 cells. The super-layers differ in orientation, alternately aligned as axial, U-stereo, and V-stereo. The stereo angle varies from 45 mrad on the innermost layer to 76 mrad on the outermost layer. The use of stereo layers provides better resolution of the z-position of tracks. The better z-positioning is gained with a slight compromise in the phi resolution of the tracks. In addition, rough z information can be used in the trigger to cleanly distinguish full tracks in an event.

The gas of the DCH is a 80%:20% mix of helium:isobutane. Using a low mass gas like helium minimizes multiple scattering, allowing a precise measurement of the radius of curvature of the track. The compromise is a smaller number of produced electrons (6× less than Argon), though this is a tolerable effect for the *BABAR* detector. For a minimum ionizing particle passing through the widest part of the cell, 6 electrons are ionized in a given cell. In the high field region near the sense wire, secondary ionization is very rapid, creating an avalanche with a gain near 5×10^4. The isobutane is an organic gas with a high absorption rate for photons. The isobutane provides a quenching mechanism which keeps the avalanche from spreading.

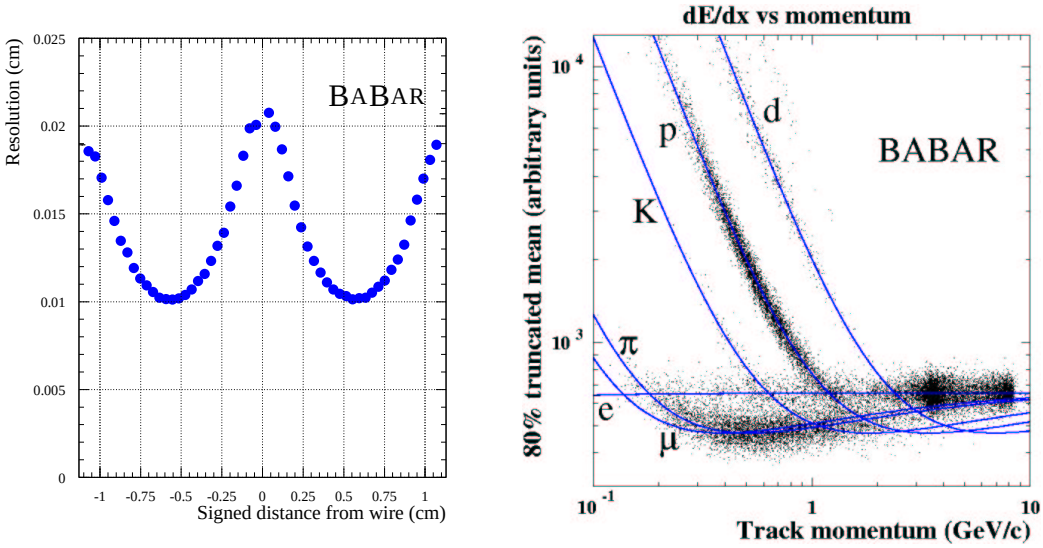

Figure 2.7: Drift chamber performance plots. Left plot shows the resolution of DCH hits. Right plots shows the DCH dE/dx versus momentum for all particles.

The DCH can also facilitate discrimination among particle types as seen in the Bethe-Bloch relation between energy loss and momentum for a given particle mass [19]:

$$\frac{dE}{dx} = 4\pi r_e^2 m_e c^2 N_A \frac{Z}{A}\frac{1}{\beta^2}\left[\frac{1}{2}\ln\left(\frac{2m_e c^2\gamma^2\beta^2 T_{max}}{I^2} - \frac{\delta}{2}\right)\right] \tag{2.1}$$

r_e and m_e are the electron's classical radius and mass, c is the speed of light, N_A is Avogadro's number, z is the charge of the incoming particle, A is the atomic weight of the absorber, β and γ are the relativistic quantities of the incoming particle, I is mean excitation energy, and δ is the density effect correction.

The amount of charge collected in the DCH when a track passes through is proportional to the energy loss. Figure 2.7 shows the measured dE/dx for tracks passing through the DCH. The tracks separate into discernible bands based on particle type.

2.4 Detector of Internally Reflected Cerenkov Light

Just outside the Drift Chamber lies the Detector of Internally Reflected Cerenkov Light (DRC), which is designed to provide excellent particle identification information. The DRC is composed of quartz bars, approximately $1.7 \times 3.5 \times 490\,\mathrm{cm}^3$ in size. The bars are arranged in 12 flat boxes in a hexagonal structure inside *BABAR*. The boxes come as close as 84 cm to the beamline, covering polar angles down to 0.445 rad in the forward direction and 2.47 rad in the backward direction.

The improved coverage in the forward region is to gain as much acceptance for particles traveling in the boost direction as possible. In the backward region, the acceptance is compromised for the readout system. A large tank, holding 6,000 liters of ultra-pure water, is positioned at the backward end of the bars to guide light emitted from the bars to an array of 10,750 2.9 cm diameter photomultiplier tubes (PMTs).

As a charged particle traverses a quartz bar, it can emit a cone of Cerenkov light if it travels fast enough. In quartz ($n = 1.473$), the Cerenkov threshold is

$$p_{thresh} = \frac{mc}{\sqrt{n^2 - 1}} = 0.925 \times mc \tag{2.2}$$

On average, a particle from a *BABAR* event emits about 150 photons per centimeter of quartz traversed. Some of the light will exit the quartz, but a portion of it will be internally reflected down the length of the quartz bar. The quartz bars are machined to extreme flatness, permitting much of the Cerenkov light to be internally reflected without loss of angle. On average, 20 photons will reach the PMTs to form a reconstructible ring.

The light cone will then be imprinted on the PMT arrays, allowing a measurement of the opening angle of the Cerenkov cone. Figure 2.8 portrays a typical two-prong

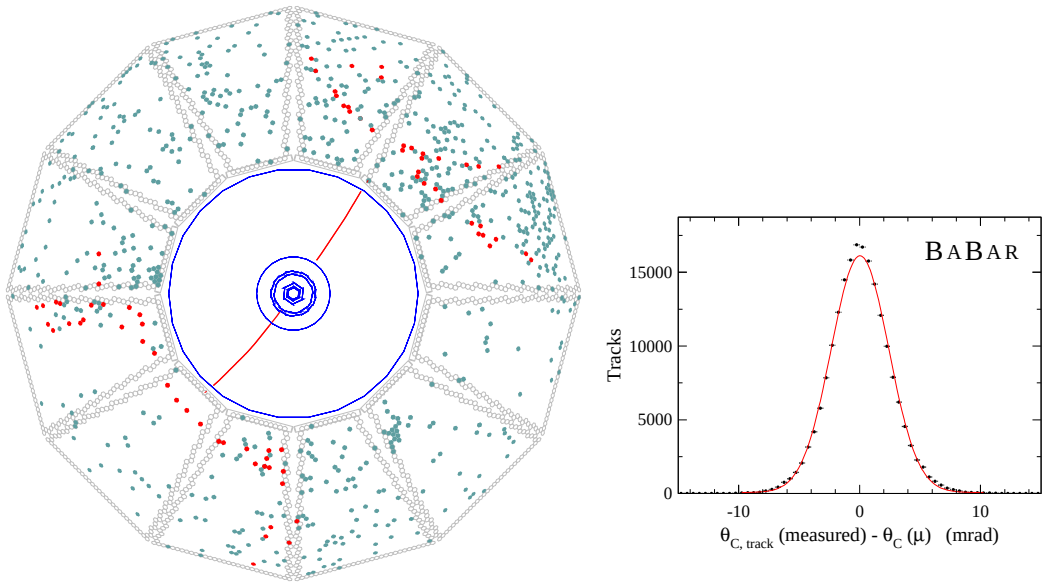

Figure 2.8: Left plot shows a physics event leaving ring images on the DRC PMT array. PMT hits occurring within 7.5 ns of the event trigger are shown in red. Right plot shows the angular resolution of Cerenkov photons emitted in di-muon events.

event and shows the resolution of the reconstructed Cerenkov cone angle. The resolution is typically limited by three main factors. One factor is the single photon resolution of 10 mrad per photon, due to the finite geometry of the bars and PMTs, as well as a the chromatic aberration from dispersion. Another factor affecting resolution is the uncertainty that stems from the tracking systems, making it more difficult to resolve then entry point of the track into the quartz. The third factor which degrades resolution is multiple scattering in the material between the active volumes of the DCH and DRC ($4\% \cdot X_o$).

A particle's mass can be estimated using the reconstructed angle of the Cerenkov light. Figure 2.9 shows the improvement in the D^0 mass peak that is gained by requiring one of the tracks to have a Cerenkov angle close to that of a kaon. A dramatic decrease can be seen in the background level without a substantial loss in efficiency. The red curve along the bottom of the right plot shows the requirement

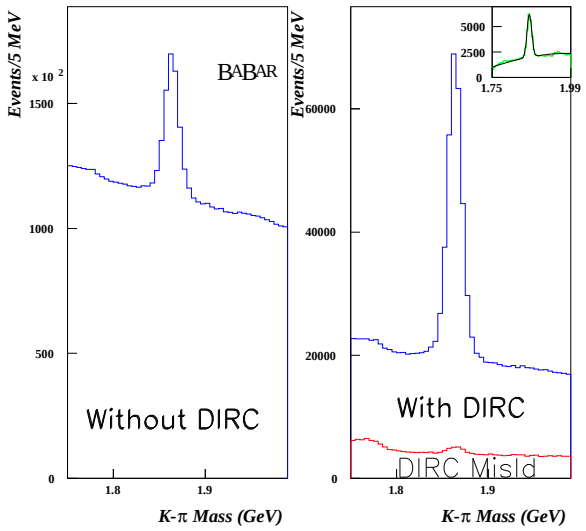

Figure 2.9: Improvement in the D^0 mass peak using DRC for particle identification.

that both tracks in the D^0 decay be consistent with the kaon hypothesis, which demonstrates the low level of mis-identification. The inset in the upper right is the peak for the Cabibbo-suppressed $D^0 to K^+\pi^-$ decay.

2.5 Electromagnetic Calorimeter

The Electromagnetic Calorimeter (EMC) is the primary detector for neutral particles, particularly low-energy photons. It is constructed using crystals doped with thallium. The crystals are arranged in two sections: a cylindrical barrel covering the main portion of the detector and an end-cap situated over the forward region.

About 5800 crystals make up the barrel, which extends radially from approximately 89 cm to 146 cm. The forward end-cap houses around 900 crystals. A crystal face is approximately $5 \times 5\,\mathrm{cm}^2$, with the body broadening slightly to the outer part of the detector. The crystal length ranges from 16 to 17.5 radiation lengths.

Figure 2.10 shows the energy and position resolution of the EMC. The energy

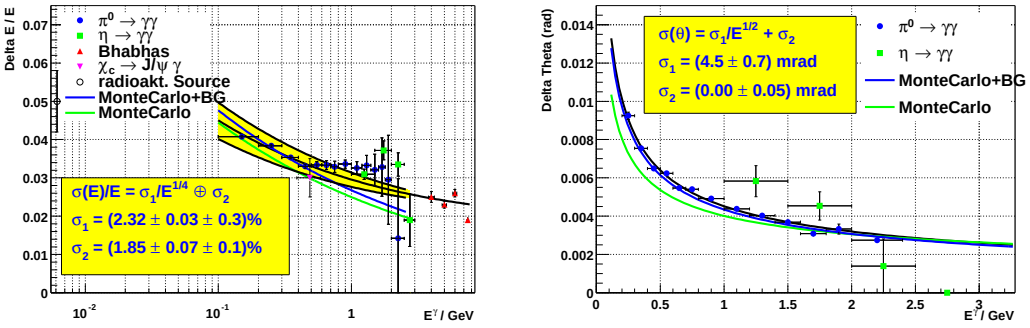

Figure 2.10: Energy(left) and position(right) resolution of the calorimeter.

resolution is better than 7% down to 50 MeV, while the resolution drops to 4% near 1 GeV. Noise in the electronics limits resolution at the lower end of the spectrum, whereas leakage limits resolution for high energy showers. The resolution is modeled with the empirical equation shown in the figure.

2.6 Instrumented Flux Return

The Instrument Flux Return (IFR) provides the main means for identifying muons with high purity and serves as a neutral hadron detector. The IFR is the outermost and largest of the *BABAR* sub-detectors. It consists of a hexagonal shaped steel support structure, segmented to contain resistive plate chambers (RPCs).

The steel is sectioned to allow large amounts of material in front of the RPCs, while still providing enough information to identify muons and hadrons. The IFR has three regions: a barrel region encompassing the bulk of the detector, and 2 endcaps to encompass the low angular regions. The barrel region has 19 layers of RPCs and the endcaps have 18. In addition, two extra layers of RPCs are installed between the EMC and the magnet.

The RPCs consist of a 2 mm gap formed between two 2 mm thick bakelite strips. The gap is constructed using PVC spacers and is filled with an Argon/Freon/Isobutane gas mixture. Just outside each of the bakelite strips, two thin sheets of graphite are held at a potential difference of 8 kV to produce an electric field through the gas mixture. As a charged particle traverses the gas, its ionization trail creates a low resistance pathway across which a 100 pC spark is discharged in 20-30 ns. Outside the graphite is a layer of insulator followed by rows of aluminum strips. The aluminum strips capacitively pick up the movement of charge within the spark as a 300 mV signal. The strip pitch ranges from 2-4 cm with 0.2 cm gaps between strips. If a single strip registers a signal, the position resolution is $\frac{pitch}{\sqrt{12}}$, or about 1 cm. The signal is read out digitally using threshold discriminators.

The IFR is efficient at detecting particles with $p_T > 0.4\,\mathrm{GeV}/c$. In order to penetrate completely through the detector, a particle must have $p_T > 0.7\,\mathrm{GeV}/c$. The majority of tracks entering the IFR are muons, though pions may punch through the calorimeter and fake a muon signal. The IFR's inner layers can also detect showers resulting from hadrons.

The efficiency of selecting muons and the probability of mis-identifying a pion as a muon are shown in figure 2.11. Inefficiencies are mainly due to the degradation over time of the detector components.

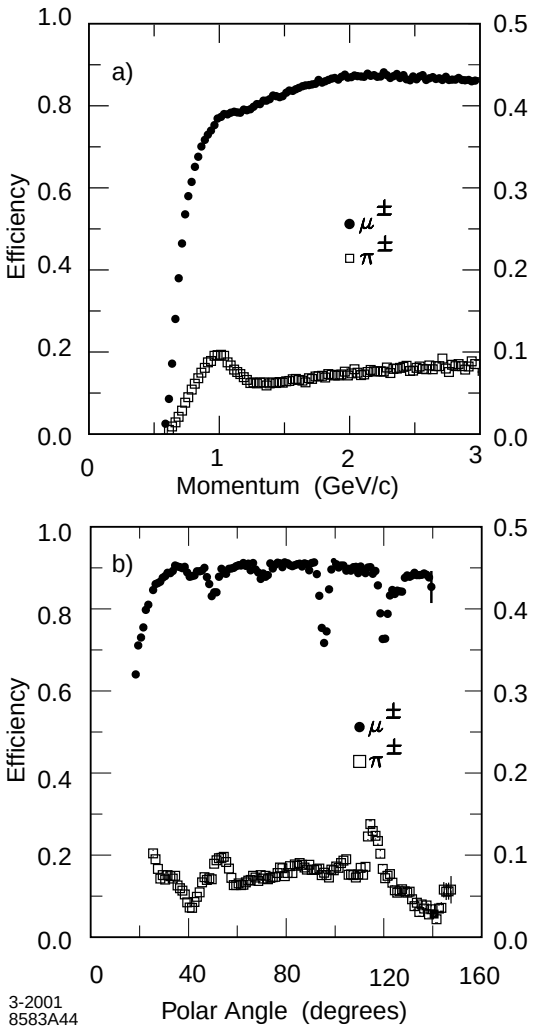

Figure 2.11: Muon efficiency (left scale) and pion misidentification probability (right scale) as a function of a) the laboratory track momentum, and b) the polar angle (for $1.5 < p < 3.0\,\mathrm{GeV}/c$ momentum), obtained with loose selection criteria.

2.7 Trigger

The Trigger system's primary requirement is to select events for physics studies, for use in either analysis, diagnostic, or calibration studies. The current *BABAR* trigger configuration consists of two levels: Level 1 trigger (L1) and Level 3 trigger (L3). The missing Level 2 trigger may be implemented in the future if the load on the trigger system warrants it. Each level has two main independent components, one based on the DCH and one based on the EMC. L1 also has a component based on the IFR, mainly to select cosmic ray muons for calibration and diagnostics.

Raw information is used by L1 to form rough tracks and energy clusters. If an event has several tracks in the DCH, especially tracks that are back-to-back, or several clusters in the EMC, it will pass L1. Additionally, if clusters are found in the same azimuthal region as tracks, an event is more likely to pass. Cuts are very loose in L1, resulting in an efficiency greater than 90% for physics events ($> 99\%$ for hadronic events). Typical event rates out of L1 are 1 kHz, with a latency of about $12\,\mu$s.

L3 takes information from L1 and performs higher quality track finding, track fitting, and clustering. Better information regarding the timing and the z positions of hits and clusters allows discrimination against out-of-time noise and beam background tracks. One high p_T track or two low p_T tracks originating from the luminous are required for the DCH trigger. For the EMC trigger, either a large number of clusters or a large amount of deposited energy throughout the detector is required for acceptance. The average event processing time in L3 is 8.5 ms. The final output of the trigger system is roughly 120 Hz, The efficiency for selecting events for analysis varies from 90% for $\tau^+\tau^-$ events to 99% for $B\overline{B}$ events.

Chapter 3

Charged Particle Tracking

3.1 Track Selection

Charged particles are reconstructed as tracks in the Drift Chamber (DCH) and Silicon Vertex Tracker (SVT). Tracks are selected for analysis based on three requirements. First, a track should have a minimum number of hits in the detector so an accurate momentum measurement can be made. The two main variables used to identify well measured tracks are the number of DCH hits used in the track fit and the transverse momentum of the track. Tracks that have large values for these variables will have penetrated further into the detector and will leave enough information to have a suitable fit of their trajectory.

The second requirement is that a track originate from the luminous region, where the e^+e^- beams collide. By requiring the track reconstructed in the detector to extrapolate close to the beamspot, tracks resulting from interactions of the beams with residual gas in the PEP-II vacuum system or with the beampipe's beryllium walls will be eliminated. Cuts on the track's distance of closest approach (DOCA) to the beamspot are made in both the plane transverse to the beam direction (DOCA_{xy})

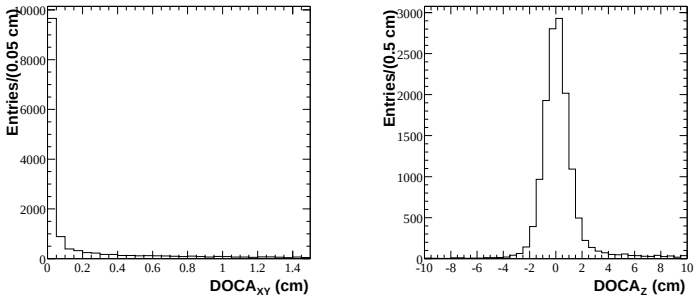

(a) DOCA$_{xy}$ (b) DOCA$_z$

Figure 3.1: Distance of closest approach in the (a) xy-plane and (b) z-direction for tag protons opposite a D^0 meson candidate in data.

and along the direction of beam travel (DOCA$_z$), conventionally termed the xy plane and the z direction. The two separate cuts are made because the luminous region is significantly larger in z than in the xy directions. Figure 3.1 shows the DOCA$_{xy}$ and DOCA$_z$ for a representative sample of tracks.

The final requirement is that a track should not be near the edge of the detector's active area so as to avoid any edge effects at the detector boundaries where efficiencies for reconstructing a track can rapidly vary. Because the resolution on a track's parameters is not perfect, it can be difficult to understand efficiency of detection in these areas.

The cuts used to select tracks with the above criteria are standard within *BABAR* analysis. These cuts are

- a minimum of 12 DCH hits,
- $p_T > 0.1$ GeV/c,
- DOCA$_{xy} < 1.5$ cm,

- $\mathrm{DOCA}_z < 10$ cm,
- $-0.824 < \cos\theta_{LAB} < 0.917$.

The efficiency for finding tracks that pass the above specifications is called tracking efficiency. There are two main effects that can cause tracking efficiency to fall below 100%. The first is an inefficiency in the detector response. Detector response may be degraded due to permanent defects, such as damaged materials, or temporary defects, such as nonoptimal voltage settings. It is also possible to have low response in the detector if a small amount of energy is deposited by a particle in the detector due to a statistical fluctuation.

The second inefficiency is attributed to mistakes made by the track fitting algorithms. If a large number of noisy channels are present, or if a considerable number of tracks occur in an event, the algorithms are not as efficient in finding tracks. As the number of charged particles in an event increases, there is a larger number of DCH cells that register hits in the event. The increased combinatorics can lead to inefficiencies in the tracking algorithms, which have to sift through all the hits to find potential tracks. Additionally, multiple tracks passing through the same cell can lead to ambiguities, further degrading the performance of the tracking system. Average event multiplicities for events used in this analysis are shown in Figure 3.2. As seen in Figure 3.2, the tracking efficiency can vary by 5-10% between events with average multiplicity to events in the tails of the multiplicity distribution.

There are two main methods used for measuring the efficiency of detecting the charged tracks used in this analysis. The first method uses $\tau^+\tau^-$ events. The τ^+ is a singly charged particle, so it must decay into an odd number (usually 1 or 3) of charged particles (usually electrons, muons, or pions) plus any number of neutral particles. Tracking efficiency is easily measured using $\tau^+\tau^-$ events in which one τ decays into one charged particle, while the other decays into 3 charged particles. This

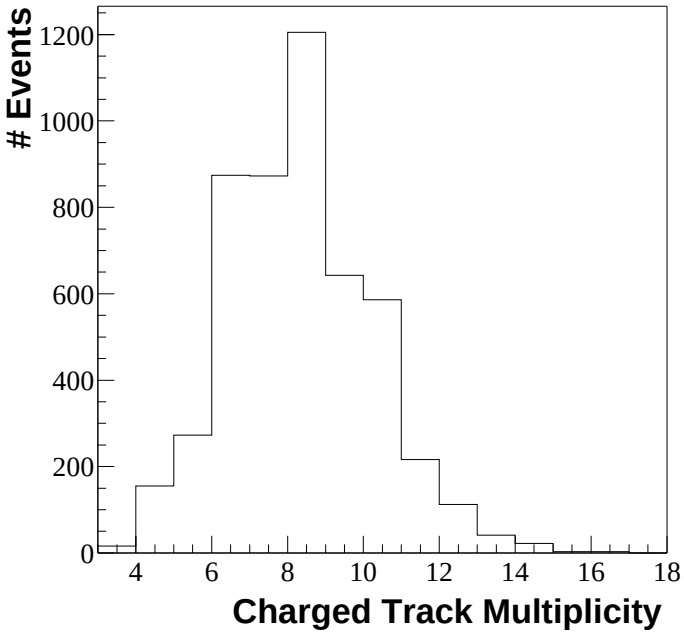

Figure 3.2: Number of charged tracks per event found for events used in this analysis.

is done by selecting events in which one hemisphere has a single charged particle and the other hemisphere has at least two charged particles. The fraction of time that the third charged particle is detected for the second τ decay is a measure of the tracking efficiency multiplied by the detector acceptance. Since the detector acceptance is well known, the tracking efficiency can be determined by this measurement.

A shortcoming of the $\tau^+\tau^-$ method is that it calculates tracking efficiencies for events with low multiplicities - only 3 or 4 charged particles per event. A complementary method to measure efficiency uses tracks reconstructed using only the SVT and tracks reconstructed using only the DCH. The SVT-only tracks are extrapolated into the DCH. The percentage of the extrapolated tracks that match a DCH-only track is a measure of the DCH efficiency. Since 12 DCH hits are required for a track to

Table 3.1: Transverse momentum required to reach the inner radius of each subdetector in *BABAR*, assuming no energy loss in the detector material.

Detector Region	r_{max} (cm)	p_T (GeV/c)
SVT Layer 1	3.3	0.007
SVT Layer 5	15.0	0.034
DCH inner wall	23.6	0.053
DRC quartz	83.7	0.188
EMC crystals	92.0	0.207
IFR Layer 1	150.0	0.338

be used in this analysis, tracking efficiency is dominated by the DCH. Consequently, this measurement is a good approximation of the actual efficiency.

3.2 Performance

Tracking efficiency is measured as a function of a particle's transverse momentum (p_T), polar angle, and azimuthal angle. Transverse momentum is used because tracking efficiency is correlated with how far a particle penetrates into the detector. A track with large p_T will traverse many subdetector elements and have a better track fit. Table 3.1 lists the minimum transverse momentum required for a track to reach various subdetectors, assuming no energy loss in the detector material.

The data for this analysis were taken at two different high voltage settings in the DCH. Therefore, the tracking efficiency is measured separately for the two disjoint subsets. The higher voltage of Block # 2 allowed a greater efficiency for detecting a charged particle in the DCH gas, but at the expense of a potentially shorter lifespan of the detector.

Measured tracking efficiencies for both data samples are shown in Figure 3.2 as a function of transverse momentum and polar angle for event multiplicities of 5,

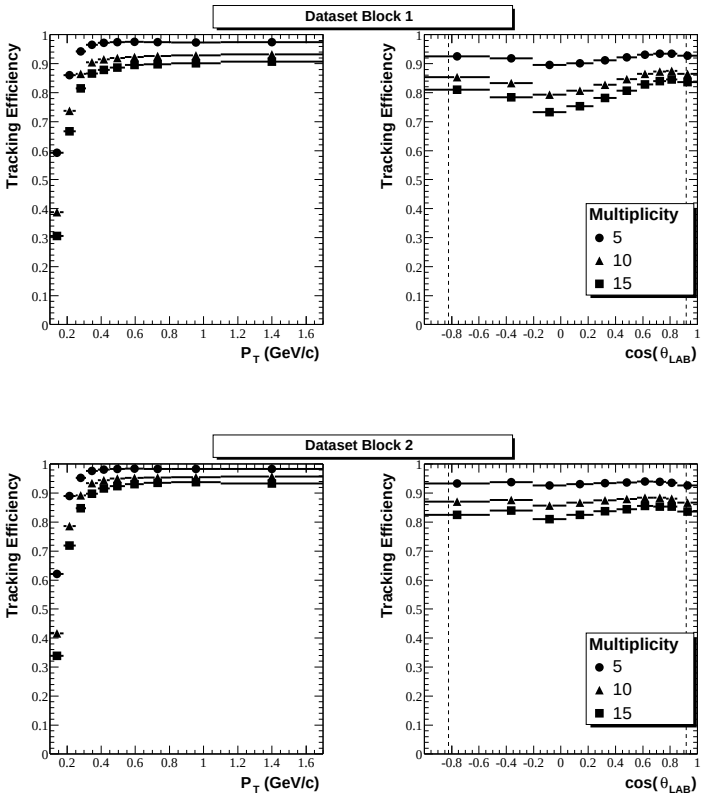

Figure 3.3: Tracking efficiency in data as a function of transverse momentum and polar angle for event multiplicities of 5, 10, and 15 tracks per event. The upper (lower) plots show the efficiencies for data block 1 (2) with a DCH high voltage setting of 1900V (1960V). The region between the dashed lines on the polar angle plots indicates the angular acceptance used in this analysis.

10, and 15 tracks per event. Above 1.7 GeV/c, the efficiency does not depend on transverse momentum. Figure 3.4 displays the ratio of tracking efficiencies measured in Monte Carlo simulated events to the efficiencies in data. The ratio is not 1.0 for most bins since the Monte Carlo simulation incorrectly models the data. The ratio is usually above 1.0, indicating that the Monte Carlo does not take into account all the inefficiencies of the actual detector.

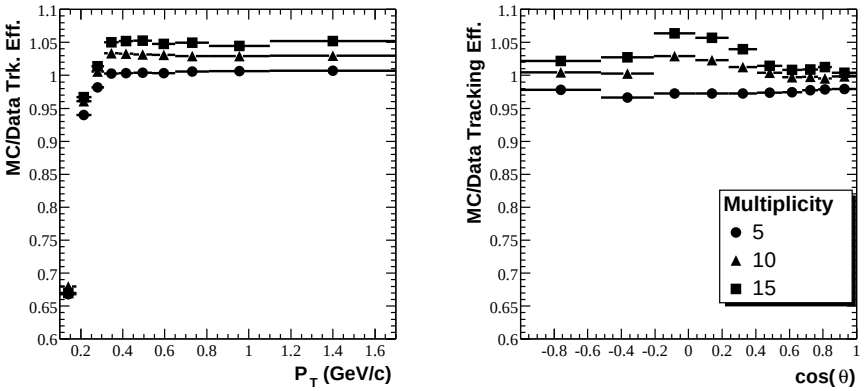

Figure 3.4: Ratio of Monte Carlo tracking efficiency to that measured in data. Efficiency ratio is plotted versus transverse momentum and polar angle for event multiplicities of 5, 10, and 15 tracks per event.

3.3 Corrections for Decays and Interactions

The methods for measuring tracking efficiency described in the previous section use samples of tracks that are predominantly pions. Additional inefficiencies arise when tracking particles other than pions due to decays in flight and physical interactions with detector material.

3.3.1 Kaon Decays

Kaons are both heavier and have a shorter lifespan than pions. Therefore, for a given momentum, kaons will travel a much shorter distance before decaying. Some of the short-lived kaons may decay before penetrating deep enough into the detector to be reconstructed. Monte Carlo simulation is used to determine the number of kaons that do not produce tracks that pass the analysis cuts. A correction factor is calculated and applied to tracking efficiency calculations so that the calculations can be appropriately applied to kaon candidates. Figure 3.5 shows the efficiency for

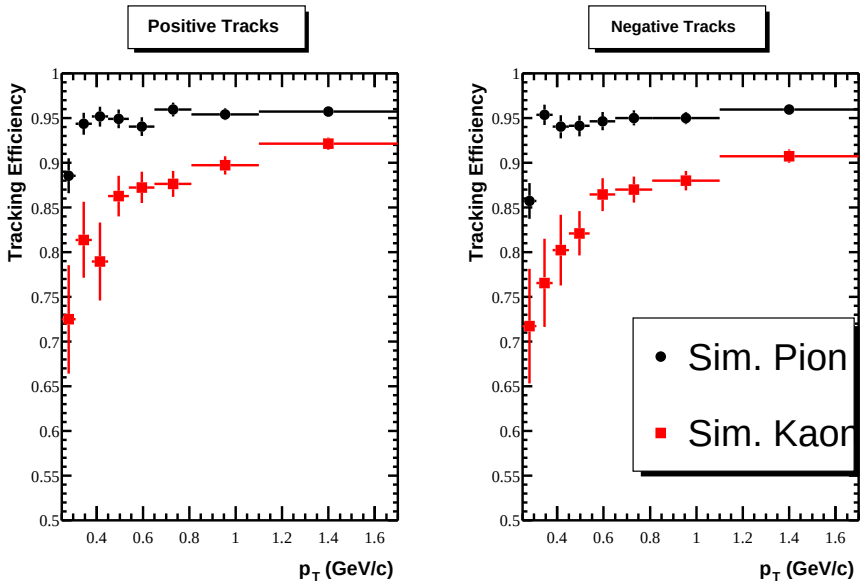

Figure 3.5: Tracking efficiency for pions and kaons in Monte Carlo simulation.

detecting pions and kaons. Kaons have a lower efficiency for detection since a small percentage of them decay before being recognized by the tracking algorithms. A slight charge asymmetry in the tracking efficiency is expected due to the higher cross section for K^- over K^+ to interact in the detector material. However, this is a smaller effect than the decay in flight correction.

The minimum radius a particle must traverse to be tracked is found by examining the efficiency of the tracking algorithms as a function of p_T. Figure 3.6 shows the efficiency of simulated pions that pass the tracking cuts as a function of p_T. Tracks with p_T above 0.15 GeV/c are reconstructed with greater than 50% efficiency. Assuming negligible energy losses in the detector material, 0.15 GeV/c corresponds to a track reaching a maximum radius of 66 cm in *BABAR*'s 1.5 T magnetic field.

The fraction of particles of a given particle species that will decay before reaching 66 cm is determined by the particle's p_T and lifetime. The bending radius of a

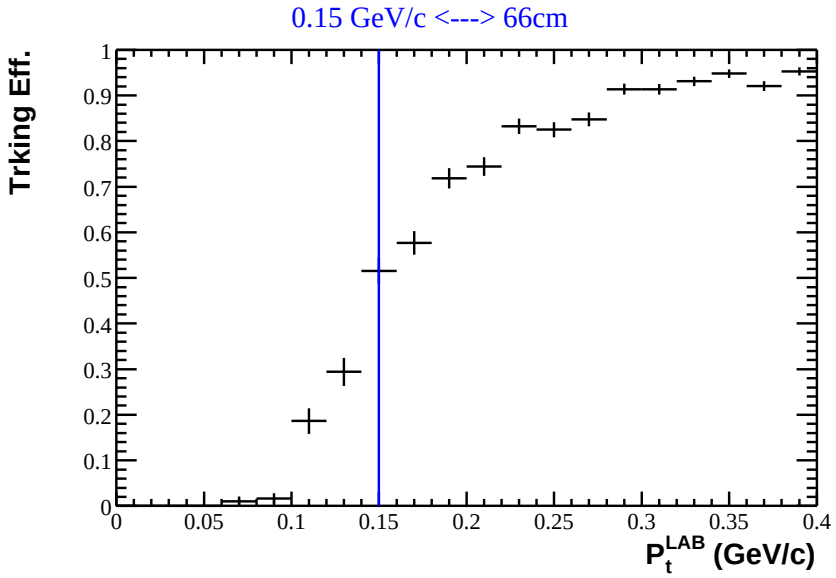

Figure 3.6: Tracking efficiency as a function of p_T for simulated pions. The efficiency crosses 50% at approximately 0.15 GeV/c, corresponding to a maximum attained radius of 66 cm in the detector.

particle's helical trajectory is

$$r = \frac{p_T}{0.3 \cdot B} \frac{\mathrm{m} \cdot \mathrm{T}}{\mathrm{GeV}/c}. \tag{3.1}$$

Using the magnetic field strength of 1.5 T in *BABAR*, the angle swept out by the particle's helical trajectory to reach a radius of 66 cm can be calculated. Looking at the projection of the trajectory in the x-y plane as a circle, this angle is defined as the angle subtended by a 66 cm chord:

$$\theta = 2 \sin^{-1}\left(\frac{0.66\,\mathrm{m}}{2 \cdot r}\right). \tag{3.2}$$

The proper time required for the particle to reach the angle θ is given as the

distance traveled divided by the velocity and the relativistic time dilation factor,

$$t = \frac{\theta \cdot r}{\beta_T \cdot c \cdot \gamma_T}, \tag{3.3}$$

where θ and r are defined above; β_T and γ_T are the usual relativistic quantities defined using the transverse momentum, p_T. Only the transverse quantities are needed since any effect of velocity and dilation resulting from longitudinal momentum are exactly canceled by the extra longitudinal distance traveled along the full 3-dimensional helix.

Once the proper time t required for a particle to travel to a radius of 66 cm is determined, the fraction of particles surviving this amount of time is given by a decaying exponential with the i'th particle's lifetime τ_i as the decay parameter

$$f_i = e^{-t/\tau_i}. \tag{3.4}$$

As a function of p_T, the fraction of kaons and pions surviving to 66 cm is shown in Figure 3.7.

Figure 3.8 shows the simulated kaon tracking efficiency overlaid with the simulated pion tracking efficiency multiplied by $\frac{f_K}{f_{pi}}$. The agreement is adequate, but not perfect. It is concluded that some of the inefficiency is explained by the decay of kaons in flight, though it may be sensitive to the momentum distribution of particles in the region of Figure 3.6 where the efficiency rapidly varies. The difference could also be the result of material interactions not taken into account in this model. Monte Carlo is expected to model all effects, so the final correction applied is the ratio of the simulated efficiencies, f_K/f_π, shown in Figure 3.5.

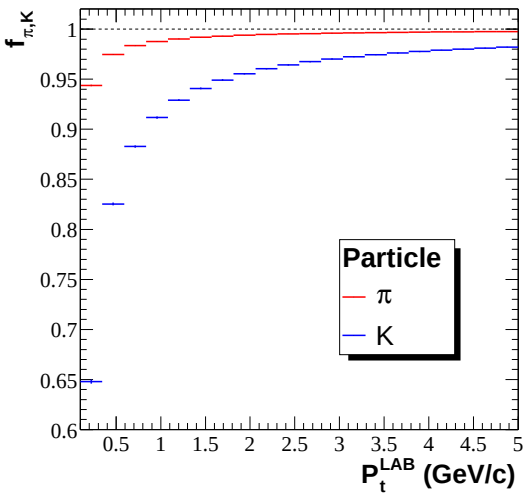

Figure 3.7: Fraction of kaons and pions which reach 66 cm before decaying as a function of p_T.

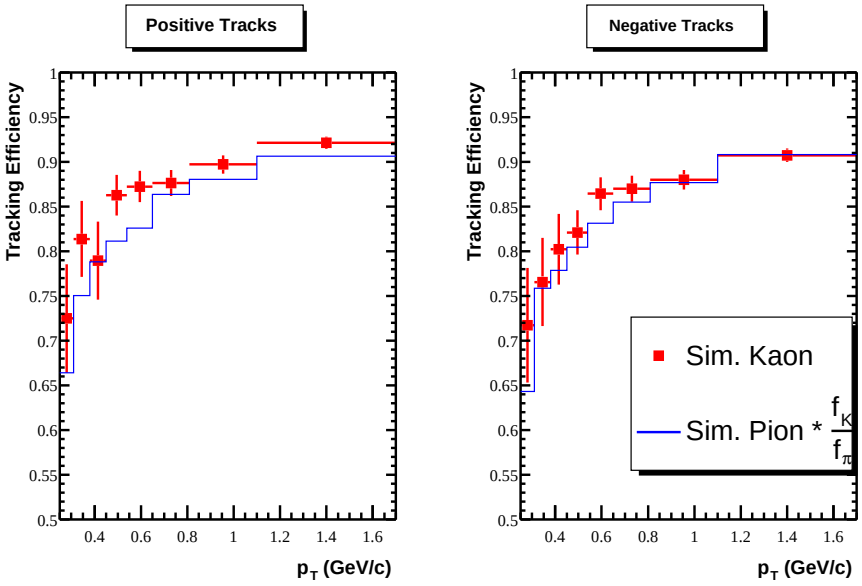

Figure 3.8: Comparison of simulated kaon tracking efficiency with the pion tracking efficiency corrected for kaon decays in flight.

3.3.2 Interactions of protons and antiprotons with matter

Protons can interact through elastic or inelastic scattering off detector material. Antiprotons can also interact through the same scattering mechanisms as protons or by annihilating with nuclei in the detector material. Particles that interact are lost from this analysis since they either will not be detected or will not pass tracking cuts. Interaction losses cause additional inefficiencies that must be calculated.

Monte Carlo simulation is applied to estimate the size of these inefficiencies. Detector simulation is done with the standard *BABAR* Monte Carlo, which uses the GHEISHA simulator in GEANT to calculate hadronic interactions. Figure 3.9 shows tracking efficiencies for protons and antiprotons used in this analysis relative to the pion efficiencies. The additional inefficiencies relative to the pions are used in the analysis to correct the tracking efficiencies for protons and antiprotons.

To check the validity of the Monte Carlo estimates, GHEISHA's assumptions regarding interaction lengths are compared against a naive calculation. The calculation uses the proton and antiproton scattering cross sections for protons and neutrons to determine the total nuclear interaction length for detector materials:

$$\lambda = \frac{A}{(Z \cdot \sigma_P + (A - Z) \cdot \sigma_N) \cdot d \cdot N_A}, \tag{3.5}$$

where A is the atomic weight (g/mole), Z is the atomic number, σ_P and σ_N are the antiproton scattering cross sections for protons and neutrons (cm^2), d is the material density ($\mathrm{g/cm}^3$), and N_A is Avogadro's number (particles/mole). The cross sections are functions of the incoming particle's energy, which are interpolated from data in the Review of Particle Physics [1].

The equation is valid in the limit that the protons and neutrons in the material scatter particles independently. Because the protons and neutrons are tightly bound inside nuclei, leading to screening, the naive model is expected to underestimate the

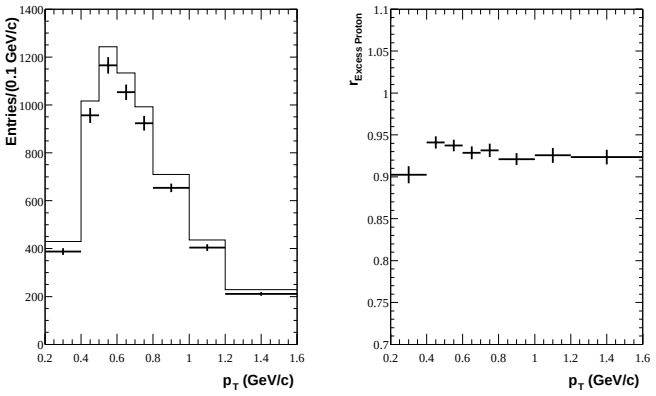

(a) Protons

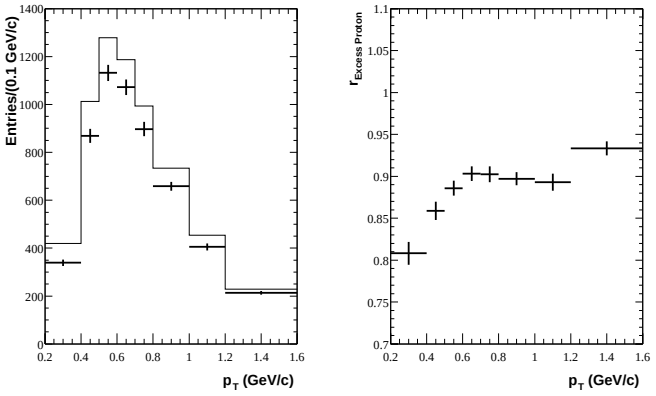

(b) Antiprotons

Figure 3.9: Ratio of tracking efficiencies for protons and antiprotons relative to tracking efficiencies for pions in Monte Carlo. The extra inefficiency is due to elastic scattering, inelastic scattering, or annihilations (antiprotons only). The efficiency is averaged over all track multiplicities.

interaction length and overestimate the amount of scattering.

Comparison with GHEISHA was done for each of the four main inner-detector materials: beryllium, used in the beampipe and DCH inner wall; water, used for cooling the beampipe; and silicon and carbon, used in the SVT active regions and support structures. Figure 3.10 shows a plot of interaction length versus antiproton lab momentum for both the calculation and the GHEISHA simulator. For comparison, the interaction length versus energy is also shown for the FLUKA hadronic simulator. It is evident that simple calculation does not agree with the simulation.

In addition to sources of inefficiency, there is one source of excess protons that affects this analysis. Occasionally, a pion or other particle will inelastically interact with a nucleus in the detector material and produce a proton. If the proton is ejected in such a way that it seems to originate near the beamspot, it can be reconstructed and accepted for analysis. Excess protons will lead to an overestimation of the number of baryonic events present in the data sample. This effect plagues the tag proton sample and not the tag antiproton sample, so charge conjugates are not implied throughout the remainder of this discussion.

To mitigate the effect of excess protons, an attempt is made to identify these protons and reject them from the analysis. One feature of the inelastic collisions that produce the protons is that they also produce several other particles. By finding the proton candidates that have a common vertex with another track inside the detector material, the excess protons can be identified with high efficiency. A cut of $\text{prob}(\chi^2) > 0.001$ is used to identify approximately 80% of the excess protons, while eliminating less than 1% of the signal. Figure 3.11 shows the momentum distribution of protons from e^+e^- collisions with the momentum distribution of all protons overlaid, as well as the ratio of the two distributions. In the bottom figure, the excess protons are suppressed, showing that a large fraction of the excess protons can be removed.

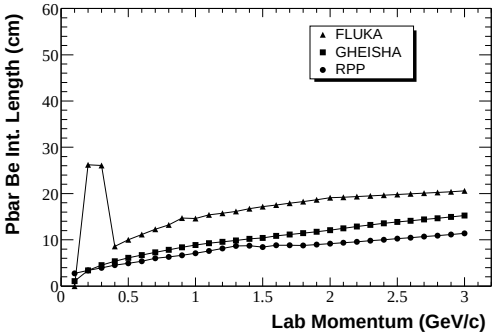

(a) Antiproton on beryllium

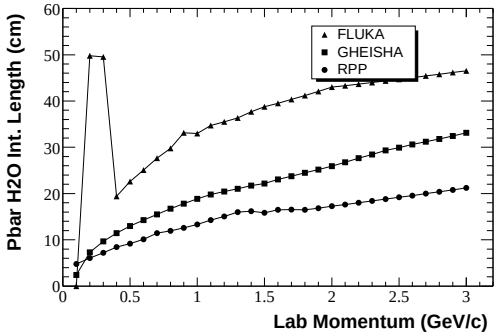

(b) Antiproton on water

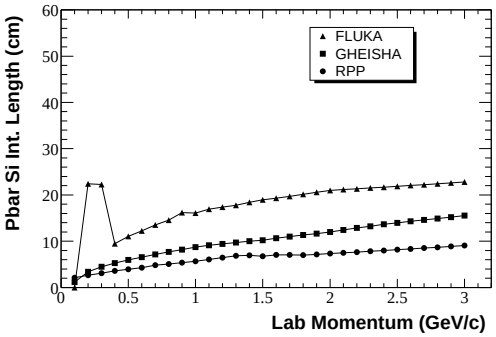

(c) Antiproton on silicon

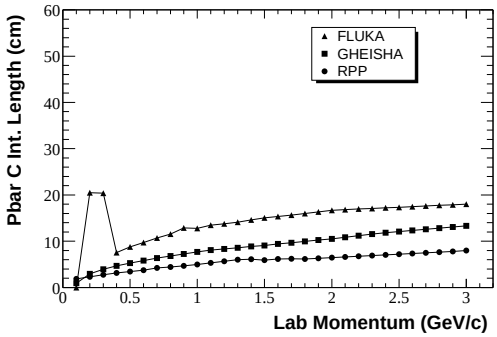

(d) Antiproton on carbon

Figure 3.10: Interaction length versus antiproton momentum for GHEISHA, FLUKA, and a naive calculation from RPP cross sections for antiproton scattering.

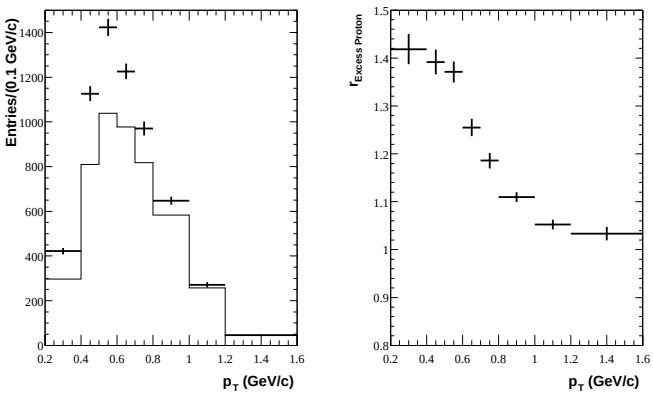

(a) Before rejection of excess protons.

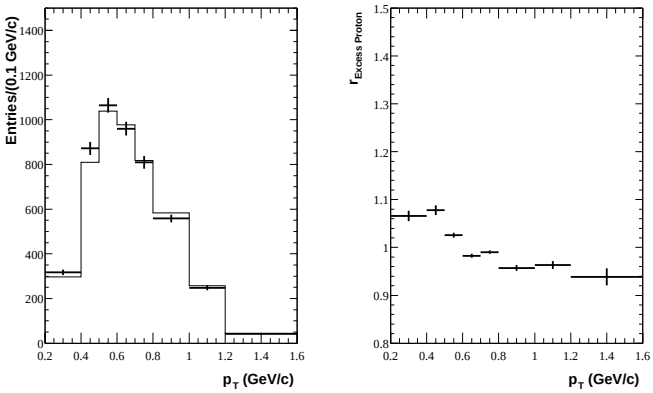

(b) After rejection of excess protons.

Figure 3.11: Distribution of selected protons originating from e^+e^- collisions in Monte Carlo simulation (histograms) overlaid with the momentum distribution of selected protons accepted in the analysis (points). The difference between the histogram and the points are the protons selected in the analysis which are not resultant from the e^+e^- collision. The right hand figures show the ratio of the two distributions. The distributions are shown (a) before and (b) after rejecting proton candidates that are consistent with intersecting another charged particle in the beam pipe or detector material.

Chapter 4

Particle Identification

Particle identification plays a key role in the analysis of $\mathcal{B}(\Lambda_c^+ \to pK^-\pi^+)$. Efficient identification of the $\overline{D}^0$, D^-, and D_s^- mesons used to determine the number of produced Λ_c^+ baryons requires accurate kaon identification. To correctly count the number of $\Lambda_c^+ \to pK^-\pi^+$ decays reconstructed, proton and kaon identification are necessary. More importantly, correct identification of lone antiproton candidates is needed to select events in which a second baryon will be present. This chapter describes the procedure used to determine selection efficiencies and misidentification rates.

4.1 Control Samples

In order to understand the efficiency of each selector to identify particular types of particles, pure samples of known particle types must be collected. These control samples are identified using particles from particular physics processes that can be isolated with only kinematic cuts. To avoid biasing the sample, no particle identification information is used for this selection. Since large data samples are ideal, control

samples are based on common physical processes. A well selected control sample contains particles over a large region of phase space so the momentum or position dependence of the selection is understood.

Occasionally two-track samples, such as Bhabha events or di-muon events, can be identified using kinematic constraints, but this method alone does not allow these types of events to be selected with high purity. To purify these samples, loose particle identification (PID) criteria is applied with care. To ensure an unbiased sample, cuts using PID variables are used to identify only one of the tracks as a potential electron or muon. If the track passes selection, the other track is admitted to the relevant control sample. It is possible for both tracks to pass the PID criteria, in which case both tracks are chosen for the control sample. Using this method, the control sample of tracks is selected cleanly and without bias.

In the control samples for hadrons, track candidates come from either the decays of Λ or D hadrons. After initial cuts, the samples are of varying purity. In all cases, mass-sideband subtraction is performed to estimate the sample yields for efficiency and misidentification calculations. Plots of momentum and polar angle distributions are also done with mass-sideband subtraction.

4.1.1 $\Lambda \to p\pi$

The $\Lambda \to p\pi$ control sample is used to select a clean sample of protons and antiprotons. A significant number of Λ s are produced at *BABAR*, either directly from $s\overline{s}$ continuum production or through the decay of heavier hadrons. Approximately 64% of all Λ s decay to $p\ \pi^-$ [1], so a large fraction of the Λ s are detected easily.

The lifetime of the Λ is 0.26 ns, which means it can travel many cm before decaying. To search for Λ s, the point of closest approach (poca) between all pairs of oppositely charged tracks is calculated. Pairs that have a poca at least 0.5 cm and

less than 40 cm from the event vertex are then kinematically fit to a common decay point. The probability of the χ^2 for the two tracks to originate from a common vertex is required to be at least 0.5%. To remove combinatoric background, the sum of the tracks' momenta at the decay point is required to lie within a 10 mrad cone around the vector between the event vertex and the candidate Λ vertex.

After the above selection criteria are applied, the sample is clean of combinatoric background, but is contaminated by two additional processes: $K^0_S \to \pi^+\pi^-$ and γ conversions to e^+e^-. To eliminate of the first background, the invariant mass of the track pair is calculated under the assumption that both tracks are pions. If the mass is within 15 MeV of the RPP K^0_S mass [1], the candidate is rejected. To remove the γ conversions, the momentum vector of the p in the Λ rest frame is determined. In general, the rest frame under the p π^- hypothesis is not the center-of-mass frame for a conversion. Therefore, the incorrect boost will cause conversions to have tracks traveling nearly parallel or anti-parallel to the Λ flight candidate direction because of the low invariant mass of the conversions. Conversions are rejected by requiring the cosine of the angle between the boosted proton and the Λ candidate flight direction to fall between -0.85 and 0.6.

Figure 4.1 shows the invariant mass of Λ candidates in data. The solid and dashed lines denote the signal and sideband regions of the final mass distribution, respectively. The signal region has a purity of $\sim$ 99%. The p π^--mass-sideband subtracted momentum and polar angle distributions of protons and antiprotons in this control sample are shown in Figure 4.2.

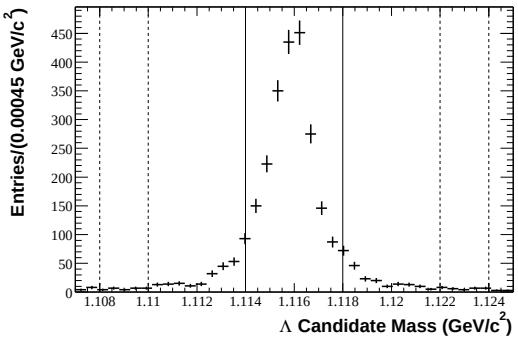

Figure 4.1: $\Lambda \to p\pi^-$ candidate mass in data. The solid lines denote the signal region. The dashed lines indicate the sideband regions.

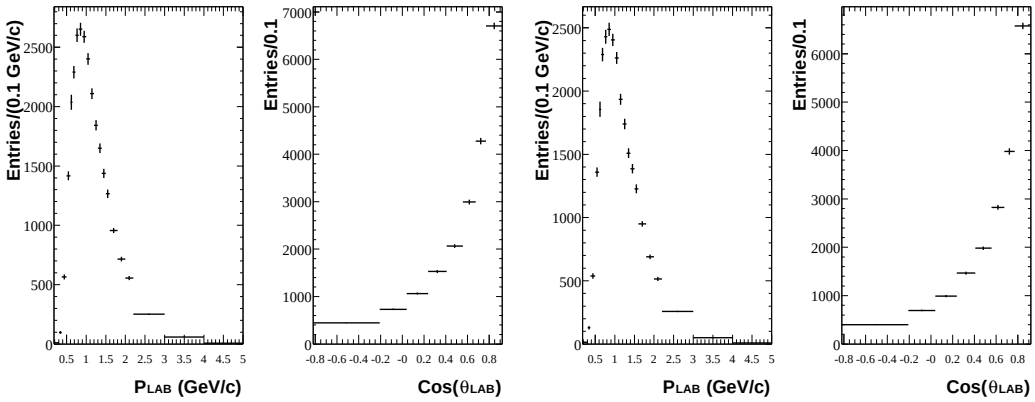

Figure 4.2: p π^--mass-sideband subtracted distribution of momentum and polar angle for protons(left) and antiprotons(right) in the $\Lambda \to p\pi$ data sample.

4.1.2 $D^{*+} \to D^0\pi^+; D^0 \to K^-\pi^+$

Th $D^{*+} \to D^0\pi^+; D^0 \to K^-\pi^+$ control sample is used to select a sample of kaons and pions from the decay of D^0 mesons. The soft pion from the D^{*+} decay suppresses combinatoric background in reconstructing the D^0 decay by allowing cuts on the D^{*+}-D^0 mass difference. The charge of the soft pion allows identification of the kaon and pion up to backgrounds resulting from doubly-Cabibbo-suppressed decays. D^0 candidates are selected in a two-step process. First, all pairs of charged tracks with a combined invariant mass between 1.40 and 2.32 GeV are chosen. The pair of tracks is then kinematically fit to a common decay vertex. If the fit converges, the pair is accepted for the D control sample. In the second step, candidates are only accepted if their invariant mass lies between 1.70 and 2.02 GeV. Candidates are rejected if the sum of the kaon and pion distances of closest approach to the fitted decay vertex is greater than 0.6 cm.

To find the D^{*+} candidates, a common vertex is fit for a D^0 ($\overline{D}^0$) with all positively (negatively) charged tracks having a laboratory momentum less than 0.5 GeV and passing within 0.3 cm of the event vertex. A candidate D^{*+} is required to have a mass between 1.93 and 2.09 GeV and must have a difference in mass with its daughter D^0 meson between 0.10 and 0.17 GeV. Additional background rejection is gained by requiring that the cosine of the angle between the kaon and the D^{*+} direction, in the D^{*+} rest frame, is greater than -0.9. Figure 4.3 shows the distributions of D^0 mass and the D^{*+}-D^0 mass difference with all cuts applied except the one on the displayed variable. The signal and sideband regions of the D^0 mass candidate are shown as solid and dashed lines, respectively. The final cuts on the D^{*+}-D^0 mass difference are shown as solid lines.

The $K^-\pi^+$-mass-sideband subtracted momentum and polar angle distributions of positive and negative kaons are shown in Figure 4.4 and that of positive and negative

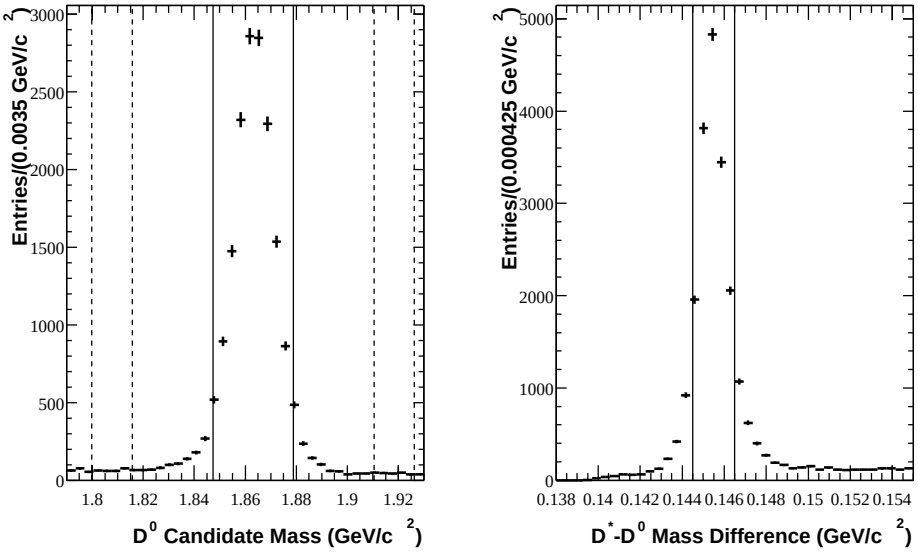

Figure 4.3: Distributions of D^0 candidate mass and D^{*+}-D^0 mass difference in the $D^{*+} \to D^0\pi^+; D^0 \to K^-\pi^+$ data sample. All cuts are applied except the one on the displayed variable. The signal and sideband regions of the D^0 mass candidate are shown as solid and dashed lines, respectively. The final cuts on the D^{*+}-D^0 mass difference are shown as solid lines.

pions in Figure 4.5.

4.1.3 $e^+e^- \to \mu^+\mu^-\gamma$

For the selection of a pure sample of muons, the relatively prolific and easy to identify $\mu^+\mu^-\ \gamma$ events are used. The γ is required so that the muon candidate sample will have a range of momenta for each polar angle in the lab frame.

An event is identified as a $\mu^+\mu^-\ \gamma$ event using kinematic constraints and applying particle identification to one of the two tracks. In order to have an unbiased sample of muons, only the track without particle identification cuts applied is included in the

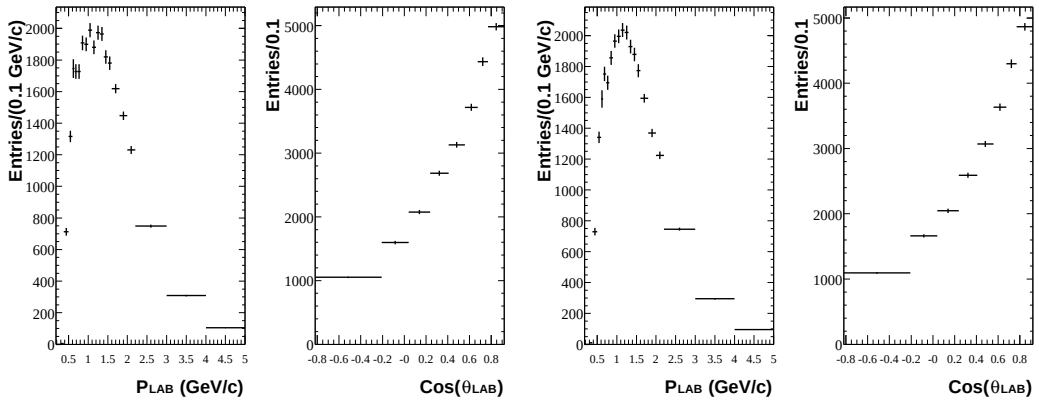

Figure 4.4: $K^-\pi^+$-mass-sideband subtracted distributions of momentum and polar angle for positive kaons (left) and negative kaons (right) in the $D^{*+} \to D^0\pi^+; D^0 \to K^-\pi^+$ data sample.

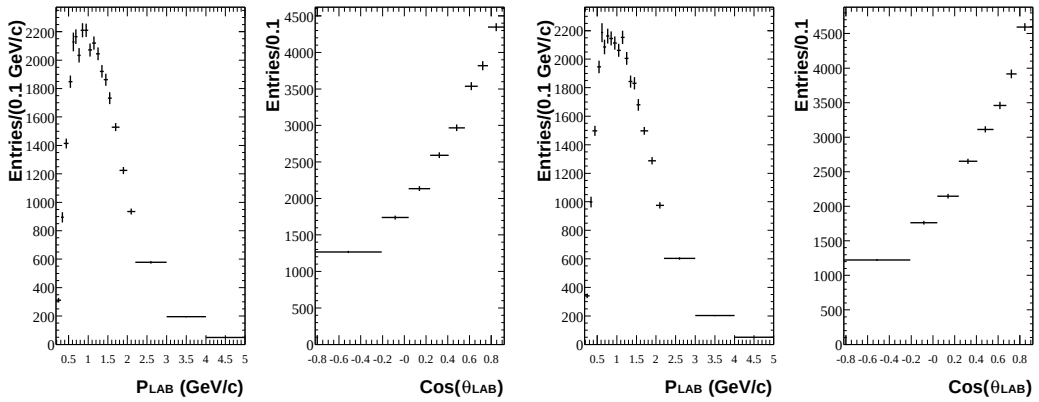

Figure 4.5: $K^-\pi^+$-mass-sideband subtracted distributions of momentum and polar angle for positive pions (left) and negative pions (right) in the $D^{*+} \to D^0\pi^+; D^0 \to K^-\pi^+$ data sample.

control sample. Using this technique, it is possible that both tracks may be selected for our sample, if they are selected by alternately applying the PID cuts to one track and then the other.

The first stage of selection makes cuts using basic event information. There must be exactly two tracks of opposite charge found in the event, and they both must pass the tracking requirements. The track's energy, with the muon hypothesis assumed, must combine with the most energetic photon's energy to be at least 5 GeV. In addition, the highest energy photon candidate must have an energy of at least 100 MeV.

If a candidate event passes first stage of cuts, a further requirement on event kinematics is applied. The highest momentum neutral cluster is required to have an energy of at least 500 MeV. Using only the two tracks in the event, the missing momentum of the event is determined. If the missing momentum is more that 0.451 mrad from the most energetic neutral cluster, the event is rejected. Using the two tracks and the most energetic cluster, the missing four-momentum of the event is reconstructed. The missing p_T must be less than 400 MeV/c, the missing energy must be less that 500 MeV and the square of the missing invariant mass must be less than 500 MeV/c^2.

Once an event passes the kinematic cuts, it must also have one track identified as a muon. The track must register in the calorimeter as a minimum ionizing particle with at least 50 MeV but no more than 400 MeV of deposited energy. The track must, on average, leave signals in no more than 10 IFR strips per IFR layer it traverses. Finally, the track must also traverse a minimum number of IFR layers. This minimum number varies with polar angle and is summarized in Table 4.1. If a track passes all these cuts, the other track in the event is selected for the unbiased control sample. The momentum and polar angle distributions of selected positive and negative muons are shown in Figure 4.6.

Table 4.1: Number of hit IFR layers, as a function of theta, required for identification as a muon for the $\mu^+\mu^-$ γ control sample.

Range	# Layers
$0.0 < \theta < 0.7$	17
$0.7 < \theta < 1.0$	13
$1.0 < \theta < 2.0$	17
$2.0 < \theta < \pi$	10

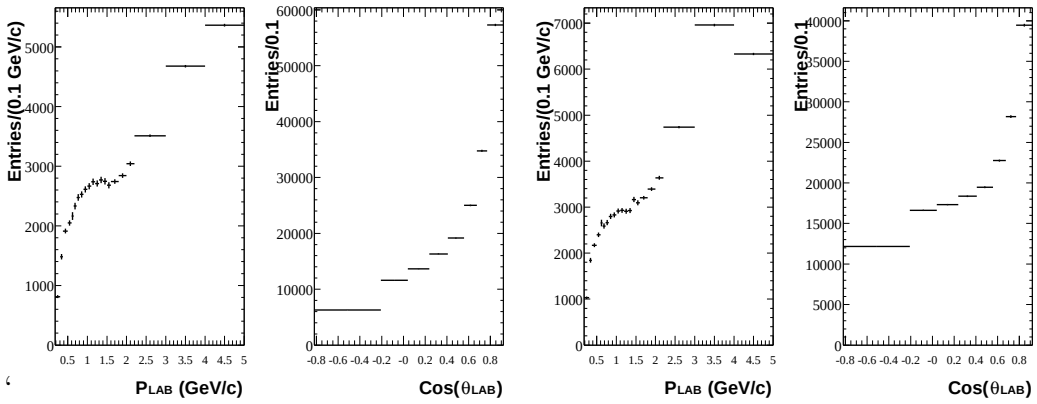

Figure 4.6: Momentum and polar angle distributions for positive muons (left) and negative muons (right) in the $e^+e^- \to \mu^+\mu^-\gamma$ data sample.

4.1.4 $e^+e^- \to e^+e^-e^+e^-$

A sample of electrons comes from four-electron events. These are events in which both the initial state electron and positron emit virtual photons that interact to produce two electrons. The initial state electrons scatter very slightly and proceed down the beampipe without interacting in the detector. The remaining electrons have balanced p_x and p_y, but not p_z: the virtual photons travel very close to the beam direction but with potentially very different energies.

Table 4.2: Acollinearity and aplanarity event cuts (top) and PID cuts (bottom) for the four-electron control sample. The discriminating variables are described in Section 4.2

Acollinearity$_{LAB} > 0.1$
Acollinearity$_{CM} > 0.1$
Aplanarity< 0.05
$\mathrm{d}E/\mathrm{d}x_{DCH} > 450$
$\mathrm{d}E/\mathrm{d}x_{SVT} < 5$
Number of EMC crystals in shower > 5
$\frac{E_{EMC}}{p} > 0.8$
$0.1 < LAT_{EMC} < 0.7$
$Z_{42} < 0.2$
No IFR strips hit

To be selected as a four-electron candidate, an event must have exactly two tracks and they must be of opposite charge. Since a large fraction of energy is carried down the beampipe, a requirement is imposed that the missing momentum of the event must lie within 8 mrad of the beam direction. Additionally, the two detected electrons must have momentum magnitudes that sum to less than 3 GeV in the center of mass frame and their total transverse momentum must be greater than 200 MeV.

Finally, the electrons are required to pass certain cuts on acollinearity and acoplanarity to reject e^+e^- and $\mu^+\mu^-$ events. The cuts are listed in Table 4.2. Once an event is selected as a four-electron candidate, one of the detected tracks is used in the control sample if the other track satisfies a set of electron identification requirements. These cuts are also summarized in Table 4.2. The momentum distribution of selected positive and negative electrons is shown in Figure 4.7. Section 4.2 will describe the discriminating variables.

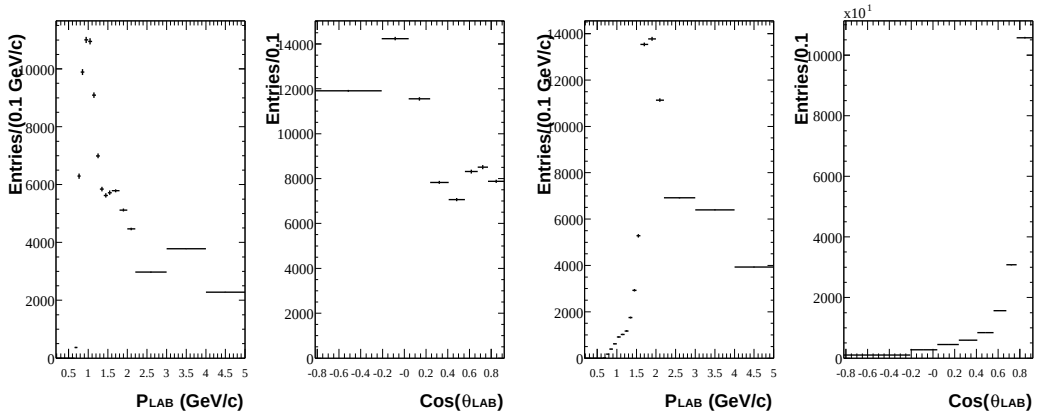

Figure 4.7: Momentum and polar angle distributions of positrons (left) and electrons (right) in the $e^+e^- \to e^+e^-e^+e^-$ sample.

4.2 Discriminating Variables

4.2.1 $\mathrm{d}E/\mathrm{d}x$ in the SVT and DCH

In addition to providing information about the location of a charged particle as it travels through the detector, the SVT and DCH also supply a measurement of the ionization the particle causes, $\mathrm{d}E/\mathrm{d}x$. The Bethe-Bloch equation [19] describes the amount of ionization produced as a function of the particle's kinematic properties and the detector make-up.

$$\frac{dE}{dx} = 4\pi r_e^2 m_e c^2 N_A \frac{Z}{A}\frac{1}{\beta^2}\left[\frac{1}{2}\ln\left(\frac{2m_e c^2\gamma^2\beta^2 T_{max}}{I^2} - \frac{\delta}{2}\right)\right] \tag{4.1}$$

where x is a density-corrected length with units g/cm^2, r_e and m_e are the electron's classical radius and mass, c is the speed of light, N_A is Avogadro's number, z is the charge of the incoming particle, A is the atomic number of the absorber, β and γ are the relativistic quantities of the incoming particle, I is the mean excitation energy, and δ is the density effect correction. Each hit in the SVT or DCH is due to

collected charge that was ionized by the particle. The *BABAR* reconstruction software determines the length of the particle's path over which the charge was liberated.

The $\mathrm{d}E/\mathrm{d}x$ measurements are roughly Gaussian distributed for very thick detectors, but the distributions tend to have large tails at high $\mathrm{d}E/\mathrm{d}x$ for the *BABAR* sub-detectors that have been designed to minimize multiple scattering. The large upward fluctuations, called Landau fluctuations, can lead to a broad distribution for the average $\mathrm{d}E/\mathrm{d}x$ for a small number of measurements. In order to remove the Landau fluctuations, high measured values of $\mathrm{d}E/\mathrm{d}x$ are not used when averaging measurements to determine a mean measured value. The averages found using this "truncated mean" behave approximately like those from a Gaussian distribution.

The SVT provides two measurements of $\mathrm{d}E/\mathrm{d}x$ for each layer that a particle traverses. As a track passes through each layer of the SVT, it creates electron-hole pairs. The bias voltage on the silicon causes the electrons and holes to separate - producing small currents on the electrodes. The number of electron-hole pairs is measured and, when combined with the knowledge of the flight length in the silicon, provides an estimate of $\mathrm{d}E/\mathrm{d}x$. Similarly, the DCH provides a measurement of $\mathrm{d}E/\mathrm{d}x$ for each cell the particle traverses. As the particle travels through the gas volume inside a cell, the track ionizes the gas of the DCH. A particle traveling near the edge of a cell tends to liberate a smaller amount of charge, whereas those traveling near the center of a cell can ionize 10's of atoms.

4.2.2 θ_c and Number of Photons in the DIRC

If a charged particle is traveling faster than the local phase velocity of light in a material, it will emit Cerenkov radiation in a cone around the particles path with an opening angle θ_C

$$\theta_C = \cos^{-1}(\frac{1}{\beta n}) \tag{4.2}$$

where $\beta = \frac{v}{c}$ is the velocity of the particle and n is the index of refraction of the material. Combined with a measurement of the particle's momentum from the SVT and DCH, the Cerenkov opening angle can provide information about the particle's mass through the determination of β, since $m = \frac{p}{\gamma\beta}$.

For the quartz of the DIRC, $n = 1.473$, the minimum β for production of Cerenkov radiation is $\beta = 0.679$ and the maximum angle ($\beta = 1$) is $\theta_C = 824\,\text{mrad}$. The momentum threshold for production of Cerenkov radiation differs for each particle species:

$$\begin{aligned} e &\quad 0.29\,\text{MeV}/c \\ \mu &\quad 60\,\text{MeV}/c \\ \pi &\quad 79\,\text{MeV}/c \\ K &\quad 280\,\text{MeV}/c \\ p &\quad 532\,\text{MeV}/c \end{aligned}$$

As seen above, almost any particle reaching the DIRC ($p_t > 0.4\,\text{GeV}/c$) will be above the threshold for production of Cerenkov radiation.

In addition to the opening angle of the Cerenkov cone, the number of detected photons provides information on the particle type. This dependence is also based on the variation of β with particle mass for a given momentum [1]:

$$\begin{aligned} \frac{d^2N}{dEdx} &= \frac{\alpha z^2}{r_e m_e c^2}\sin^2(\theta_C) \\ &\approx 370\left(1 - \frac{1}{\beta^2 n^2}\right)\,\text{eV}^{-1}\,\text{cm}^{-1}. \end{aligned} \tag{4.3}$$

N is the number of produced photons, E is the energy of the photon, x is the distance traveled by the particle, α is the fine structure constant, r_e and m_e are the electron's classical radius and mass, and c is the speed of light. Approximately 150 photons are produced by a particle traversing normally through a bar of quartz in *BABAR*, though only 10-20 are internally reflected and detected by the DIRC.

4.2.3 Deposited Energy in the EMC

The EMC is the main detector for finding neutral particles, specifically photons, produced in a physics event. Photons are identified as showers in the EMC that do not have any reconstructed track directed at them.

The shape of the shower in the EMC is also used for particle discrimination. The simplest discrimination to make is that between muons, electrons, and hadrons. Muons do not shower in the EMC, but rather ionize as they do in the SVT or DCH. Muons are thus visible as tracks pointing to EMC showers with very low energy.

The energy deposited in the EMC by a particle provides discrimination between electrons and hadrons. The charged particles fully captured within the EMC deposit all of their energy:

$$E_{meas} = (\gamma - 1)mc^2. \tag{4.4}$$

For relativistic particles like the electron, this equates to a deposited energy nearly equal to the particle's momentum times the speed of light. Hadrons are heavier and less relativistic, leading to a deposited energy that can be less than the particle's momentum times the speed of light. In addition, hadrons are more likely to penetrate the EMC and have showers that are not fully contained in the EMC. Thus, be will tend to have $E/p < 1$, while electrons will have $E/p \sim 1$.

4.2.4 IFR

The outermost detector, the IFR, is predominantly used for the identification of muons, since the majority of muons will not interact heavily with any of the other subdetectors. By matching hits in the IFR to tracks found by the tracking algorithms, it is possible to detect probable muons.

Occasionally, pions do not interact in the EMC or in the magnet, so they appear

as hits in the IFR. However, pions are expected to interact in the iron of the IFR. To discriminate against pions, the number of hit layers and the average number of hits per layer can be computed. Since pions are more likely to be absorbed than muons, they will not travel through all the layers of the IFR. Also, pions are expected to produce wide showers, leading to a large number of hit strips per layer.

4.3 Proton Identification

4.3.1 Proton Selection

Proton selection is based on likelihoods calculated for each of the five subdetectors: SVT, DCH, DRC, EMC, and IFR. Each subdetector is assigned a likelihood for each of the five possible particle hypotheses (proton, kaon, pion, muon, electron). A subdetector's set of likelihoods is re-scaled such that the most likely hypothesis is given a likelihood of unity. After normalization, any likelihood below a minimum value, the floor value, is set to the floor value. The floor value is assigned per detector, and it acts to limit a detector's ability to discriminate too strongly against a hypothesis. The floor values are shown in Table 4.3. In essence, the floor does two things: it protects against detector malfunctions that might give unreasonably small likelihoods for any hypotheses, and it adds tails to the idealized likelihood functions used to calculate the likelihoods. The five likelihoods for subdetectors d for a given hypothesis h are multiplied together, along with an apriori likelihood for each hypothesis:

$$\mathcal{L}(h) = \mathcal{L}^{apriori}(h) \cdot \prod_{d=SVT}^{IFR} max(\mathcal{L}^{floor}(d), \mathcal{L}^{opr}(d,h)) \tag{4.5}$$

A proton candidate is then selected if the likelihood for the proton hypothesis is

Table 4.3: Floor and likelihood parameters used by the proton selector.

Quantity	Loose Value	Tight Value
$\mathcal{L}^{floor}(SVT)$	0.0040	0.0040
$\mathcal{L}^{floor}(DCH)$	0.0018	0.0018
$\mathcal{L}^{floor}(DRC)$	0.0100	0.0100
$\mathcal{L}^{floor}(EMC)$	0.0150	0.0150
$\mathcal{L}^{floor}(IFR)$	0.0200	0.0200
$\mathcal{L}^{apriori}(e)$	1.0	20.0
$\mathcal{L}^{apriori}(\mu)$	1.0	20.0
$\mathcal{L}^{apriori}(\pi)$	1.0	400.0
$\mathcal{L}^{apriori}(K)$	1.0	400.0
$\mathcal{L}^{apriori}(p)$	1.0	1.0

greater than the likelihood for any other particle:

$$\mathcal{L}(p) > max(\mathcal{L}(K), \mathcal{L}(\pi), \mathcal{L}(\mu), \mathcal{L}(e)) \tag{4.6}$$

This is effectively a cut on the likelihood ratios of the proton hypothesis to the four other hypotheses. The strength of the cut is determined by the values of the apriori likelihoods. Table 4.3 shows the apriori likelihoods used for the Loose and Tight selectors.

4.3.2 Likelihood Calculation

This section describes the likelihood calculations for those detectors most sensitive for hadron selection: SVT, DCH, and DRC. The likelihood for the SVT is calculated from an asymmetric Gaussian function of the logarithm of $\mathrm{d}E/\mathrm{d}x$:

$$e^{\left(\frac{(ln(\mathrm{d}E/\mathrm{d}x_{meas}) - ln(\mathrm{d}E/\mathrm{d}x_{th}))^2}{2\sigma\sqrt{5/N}}\right)}, \tag{4.7}$$

with $\sigma = \sigma_L$ for $\mathrm{d}E/\mathrm{d}x_{meas} < \mathrm{d}E/\mathrm{d}x_{th}$ and $\sigma = \sigma_R$ for $\mathrm{d}E/\mathrm{d}x_{meas} > \mathrm{d}E/\mathrm{d}x_{th}$. The left-side and right-side standard deviations of the asymmetric Gaussian are fixed parameters. These standard deviations are calculated for five measured $\mathrm{d}E/\mathrm{d}x$ samples, and they are inflated slightly for tracks with fewer samples to account for a wider spread in the truncated mean.

A minimum of three of the five SVT layers is required to provide $\mathrm{d}E/\mathrm{d}x$ information; otherwise, the SVT likelihood is not calculated. In order to mitigate the effects of Landau fluctuations, only the smallest 60% of the $\mathrm{d}E/\mathrm{d}x$ values are used to calculate the mean $\mathrm{d}E/\mathrm{d}x$ value for a track. For five samples, the lowest 3 values are used for the average; in the case of four samples, the 3rd lowest value is given a weight of 40% when averaged with the lowest two values. The expected $\mathrm{d}E/\mathrm{d}x$ is found from a five-parameter Bethe-Bloch equation, using the momentum of the fit to the considered hypothesis:

$$\mathrm{d}E/\mathrm{d}x_{th} = a \cdot (\beta^{-b}) \cdot (c - b^2 - \log(d + (\gamma\beta)^{-e})). \tag{4.8}$$

The DCH likelihood for a particle is calculated using a symmetric Gaussian function of the mean measured $\mathrm{d}E/\mathrm{d}x$:

$$e^{(\frac{(\mathrm{d}E/\mathrm{d}x_{meas} - \mathrm{d}E/\mathrm{d}x_{th})^2}{2\sigma})}. \tag{4.9}$$

The $\mathrm{d}E/\mathrm{d}x$ in the DCH is measured in arbitrary units because a direct calibration is tedious and not necessary for analysis. For reference, tracks with momenta between 0.5 and 5.0 GeV have $\mathrm{d}E/\mathrm{d}x$ measurements between 400 and 1500 in these arbitrary units. A $\mathrm{d}E/\mathrm{d}x$ measurement in a cell is used if the track passes through the inner 95% of the cell area. A minimum of eight usable cell samples is required in order to calculate a reliable likelihood. To mitigate the effects of Landau fluctuations, only

the smallest 80% (rounding down) of the samples are used. The expected $\mathrm{d}E/\mathrm{d}x$ is calculated from a calibrated Bethe-Bloch equation, using the reconstructed value of the momentum in the DCH for a given hypothesis. The uncertainty on the measured $\mathrm{d}E/\mathrm{d}x$ is a complicated function of the measured mean, the number of samples, the RMS of the $\mathrm{d}E/\mathrm{d}x$ values, and the track hypothesis. If the error is found to be less than 0.1 units, the calculation is flagged as non-physical and the result is excluded in likelihood comparisons.

The DIRC likelihood is calculated using the number of photons detected in the Cerenkov ring and the angle of the Cerenkov cone with respect to the track direction as it enters the DIRC. The expected number of photons, N^{exp}, is taken from a calibration table created using a large number of reconstructed tracks.

The expected Cerenkov angle, θ_C^{exp}, is determined using the track momentum at the entrance to the DIRC, the track mass hypothesis, $\cos(\theta_C) = \frac{1}{n\beta}$,, and $\beta = \frac{p}{\sqrt{(pc)^2+(mc^2)^2}}$. The measured Cerenkov angle, θ_C^{meas}, and its error, σ_C, are calculated from fitting the ring of photons observed in the DIRC PMTs.

The final likelihood is found by multiplying a Poisson distribution for the measured number of photons and a Gaussian distribution for the measured Cerenkov angle:

$$\mathcal{L} = \frac{1}{\sqrt{2\pi}\sigma_C} e^{\frac{(\theta_C^{exp}-\theta_C^{meas})^2}{2\sigma_C}} \cdot \frac{e^{-N^{exp}}(N^{exp})^{N^{obs}}}{N^{obs}!}. \tag{4.10}$$

4.3.3 Performance

The figures in this section show the proton identification efficiency as a function of momentum and polar angle for positive and negative tracks. There are two noticeable regions where the efficiency decreases significantly. The drop in efficiency for negative tracks just above 1 GeV is due to the difficulty in discriminating against e showers and $\overline{p}$ annihilation showers in that momentum range. The tight selector nearly vetoes

this region completely in order to deal with this similarity.

The other region of low efficiency occurs for $\cos\theta \approx 0$, due to alignment of the particle within the detector. At $\cos\theta = 0$, particles have the smallest path length through each layer of the detector. In the SVT and DCH, this translates to a smaller amount of deposited charge, whereas in the DRC this leads to a smaller number of Cerenkov photons. In all these detectors, the shorter path length leads to poorer resolution. In the DRC, the effect is mitigated to some extent – due to the geometry of internal reflection, more photons are captured in the bars for tracks at these angles.

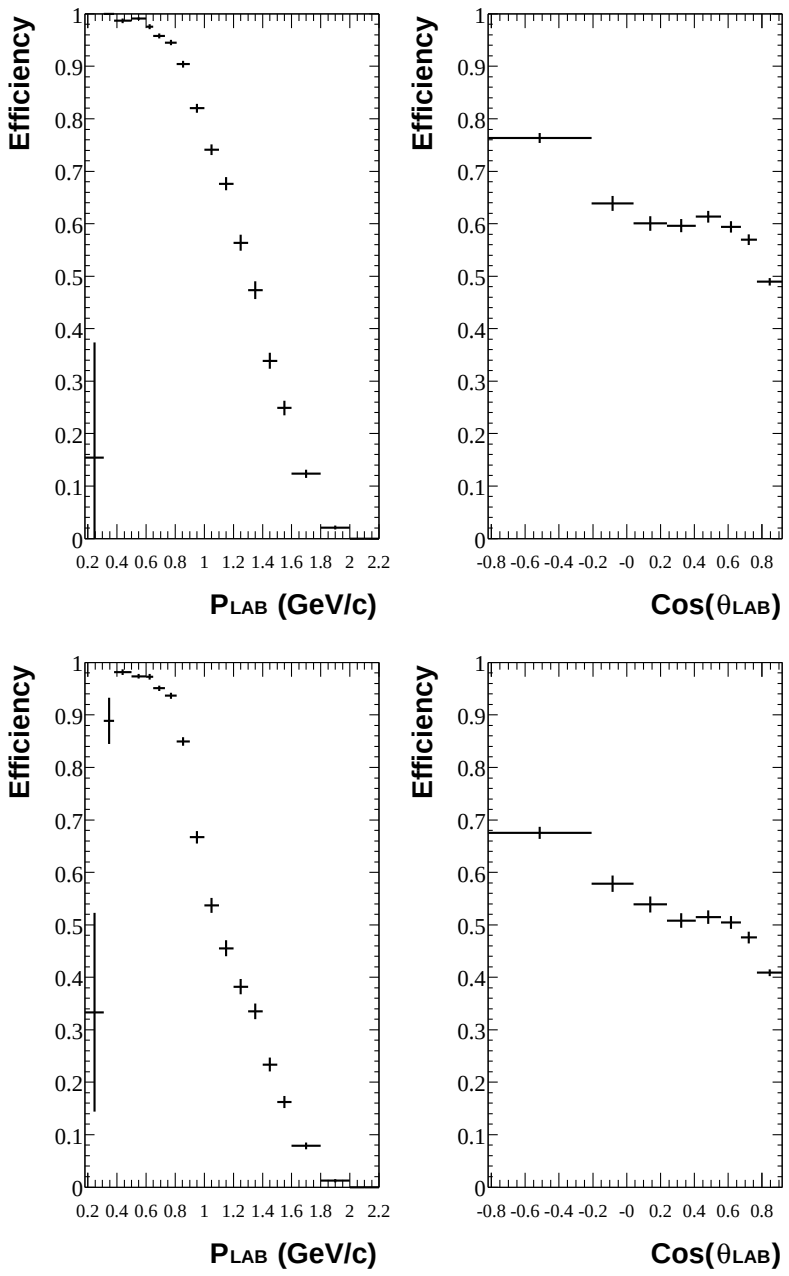

Figure 4.8: Tight proton selector efficiency for the proton control samples in data block #1.

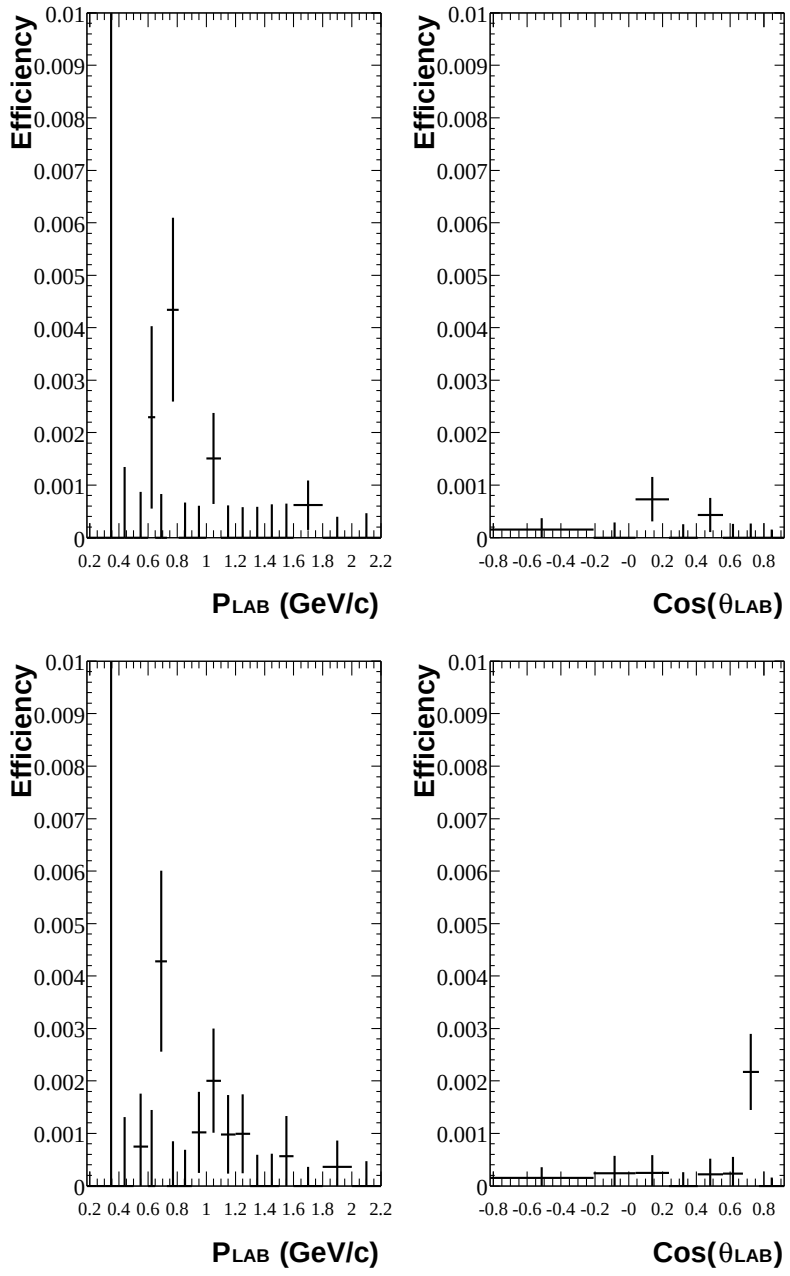

Figure 4.9: Tight proton selector efficiency for the kaon control samples in data block #1.

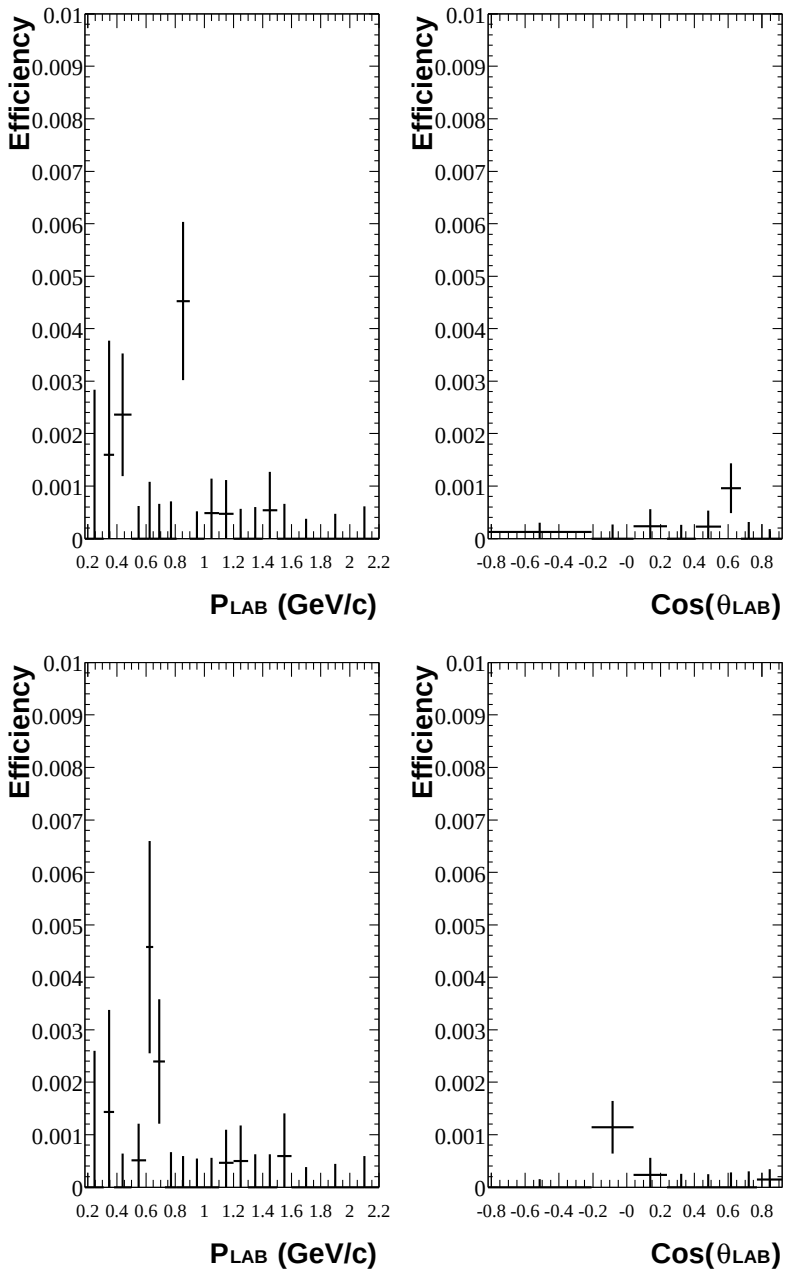

Figure 4.10: Tight proton selector efficiency for the pion control samples in data block #1.

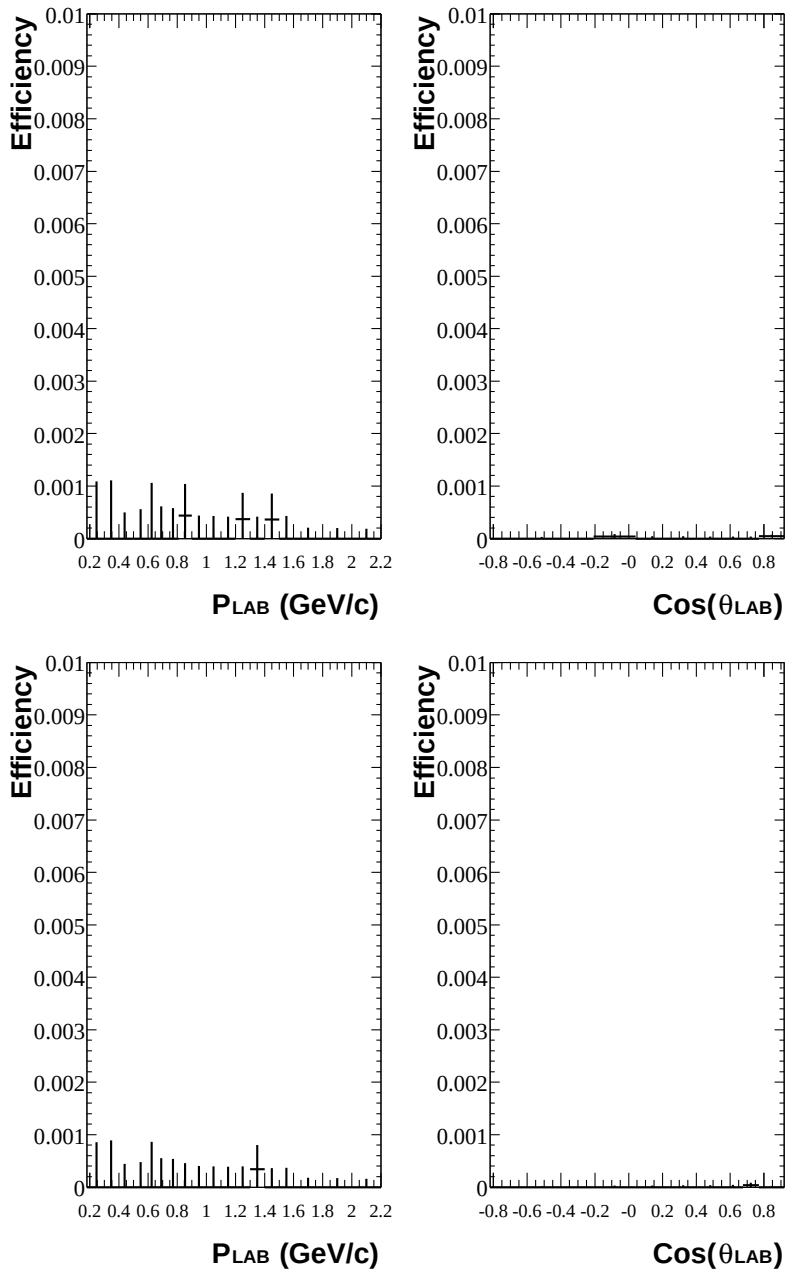

Figure 4.11: Tight proton selector efficiency for the muon control samples in data block #1.

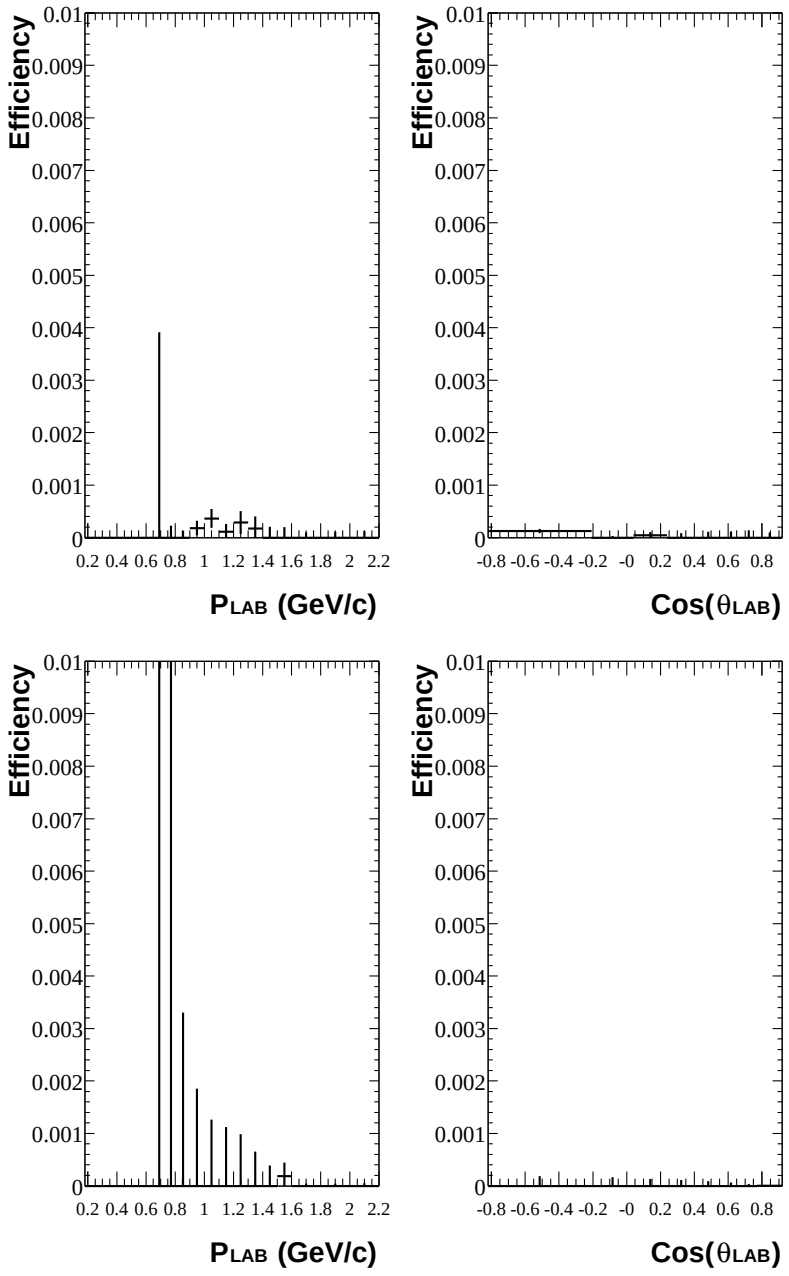

Figure 4.12: Tight proton selector efficiency for the electron control samples in data block #1.

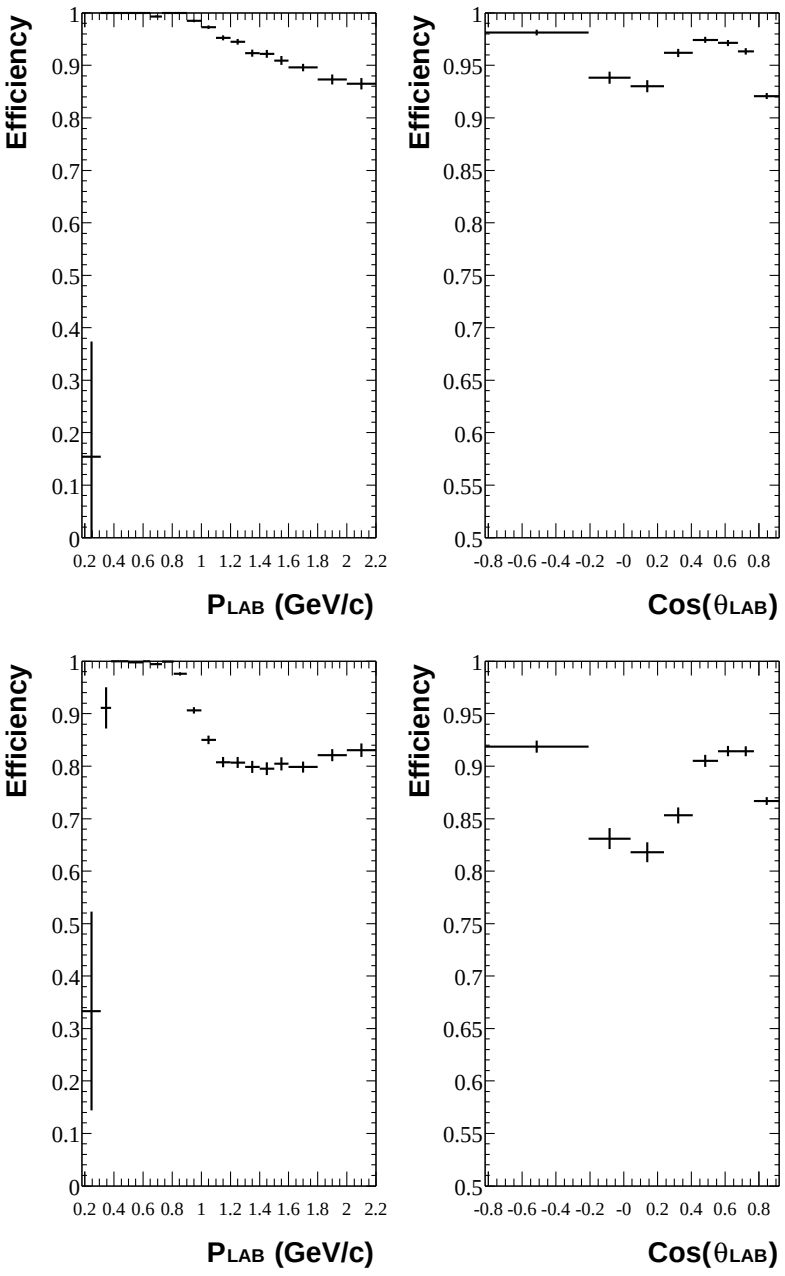

Figure 4.13: Loose proton selector efficiency for the proton control samples in data block #1.

4.4 Kaon Identification

4.4.1 Kaon Selection

Kaon selection applies information from the SVT, DCH, and DIRC. The information for each subdetector is used only in the momentum range where it will provide the best discrimination. Outside a subdetector's useful momentum range, the likelihood value is assigned the value one. In the case of the DIRC, a further restriction exists. At momenta below 1 GeV/c^2, kaons are just starting to cross the threshold to produce Cerenkov radiation. To mitigate this effect, the DIRC is not used, i.e. assigned a likelihood value of one, if the measured Cerenkov angle θ_C satisfies the following constraint:

$$\theta_C > (0.31 \cdot p + 0.48), \tag{4.11}$$

where p is expressed in GeV/c. The region in the $\theta_C - p$ plane covered by this exclusion is shown in Figure 4.14.

For reconstructing charm hadrons, a pion veto is used to reject pions while keeping a large percentage of kaons. In order to select a fake-PID sample enriched in pions and kaons but void of protons, a tight selection criteria is applied with a veto of loose protons. The loose proton selection used in the veto is described in Section 4.3.

Likelihood ratio cuts vary as a function of momentum. Table 4.4 summarizes the parameters of the kaon selectors.

4.4.2 Likelihood Calculation

The likelihood calculations for the SVT, DCH, and DRC are completed as described in Section 4.3.2. The EMC and IFR are not used.

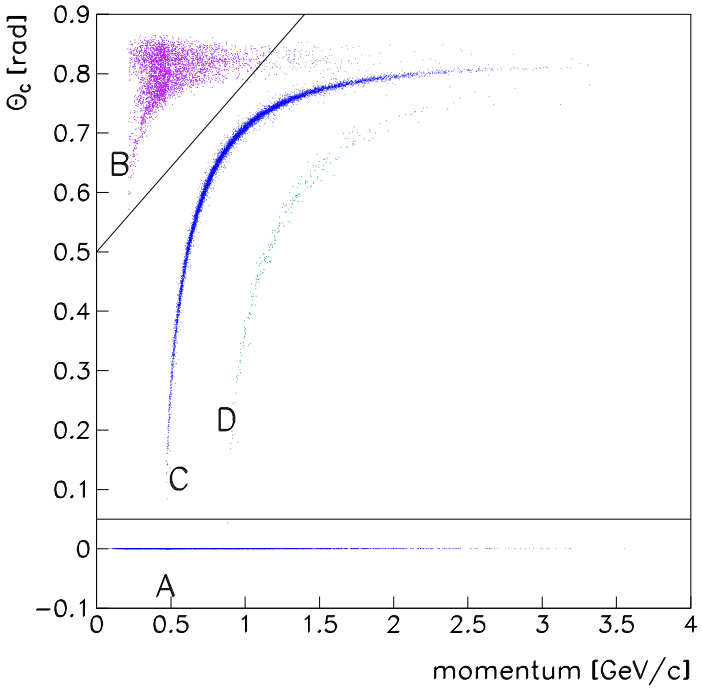

Figure 4.14: Plot of θ_C versus momentum in data showing DRC exclusion region for likelihood calculation.

Table 4.4: Parameters used by the kaon selectors.

Quantity	Pion Veto	Tight Selection
SVT p range	$< 0.5\,\mathrm{GeV}$	$< 0.7\,\mathrm{GeV}$
DCH p range	$< 0.6\,\mathrm{GeV}$	$< 0.7\,\mathrm{GeV}$
DRC p range	$> 0.6\,\mathrm{GeV}$	$> 0.6\,\mathrm{GeV}$
criteria	$\mathcal{L}_K > r \cdot \mathcal{L}_\pi$ or $\mathcal{L}_p > r \cdot \mathcal{L}_\pi$ $p < 0.5\,\mathrm{GeV}/c \quad r = 0.1$ $p > 0.5\,\mathrm{GeV}/c \quad r = 1$	$\mathcal{L}_K > r \cdot \mathcal{L}_\pi$ and $\mathcal{L}_K > \mathcal{L}_p$ $p < 0.5\,\mathrm{GeV}/c \quad r = 1$ $0.5 < p < 0.7\,\mathrm{GeV}/c \quad r = 15$ $0.7 < p < 2.7\,\mathrm{GeV}/c \quad r = 1$ $p > 2.7\,\mathrm{GeV}/c \quad r = 80$

4.4.3 Performance

The figures in this section show the kaon identification efficiency as a function of momentum and polar angle for positive and negative tracks. The notable variations in efficiency occur in the 0.5-0.7 GeV/c momentum range. In this range, the SVT and DCH become less useful and are ignored for momenta higher than 0.7 GeV/c in either the Pion Veto or the Tight Selection mode. Also, in this region the DRC is beginning to provide identification of kaons.

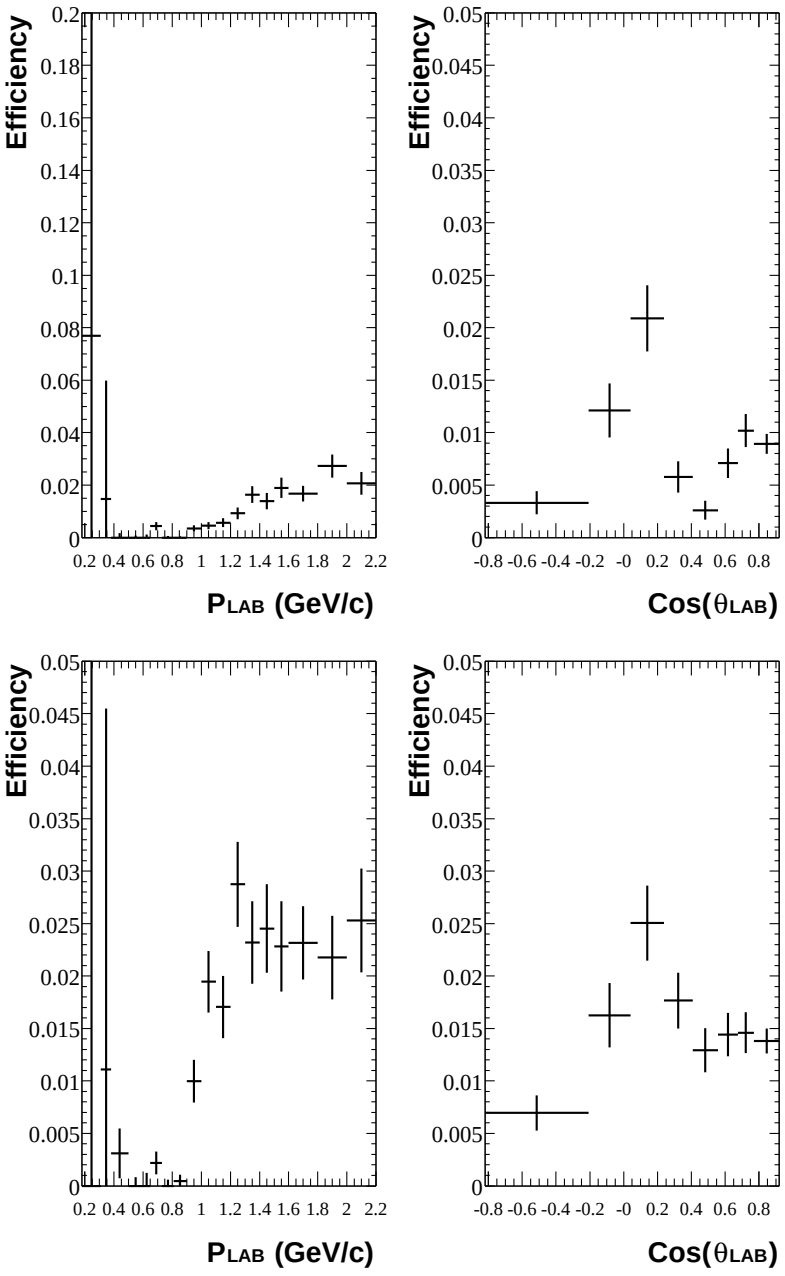

Figure 4.15: Fake selector efficiency on the proton control samples in data block #1.

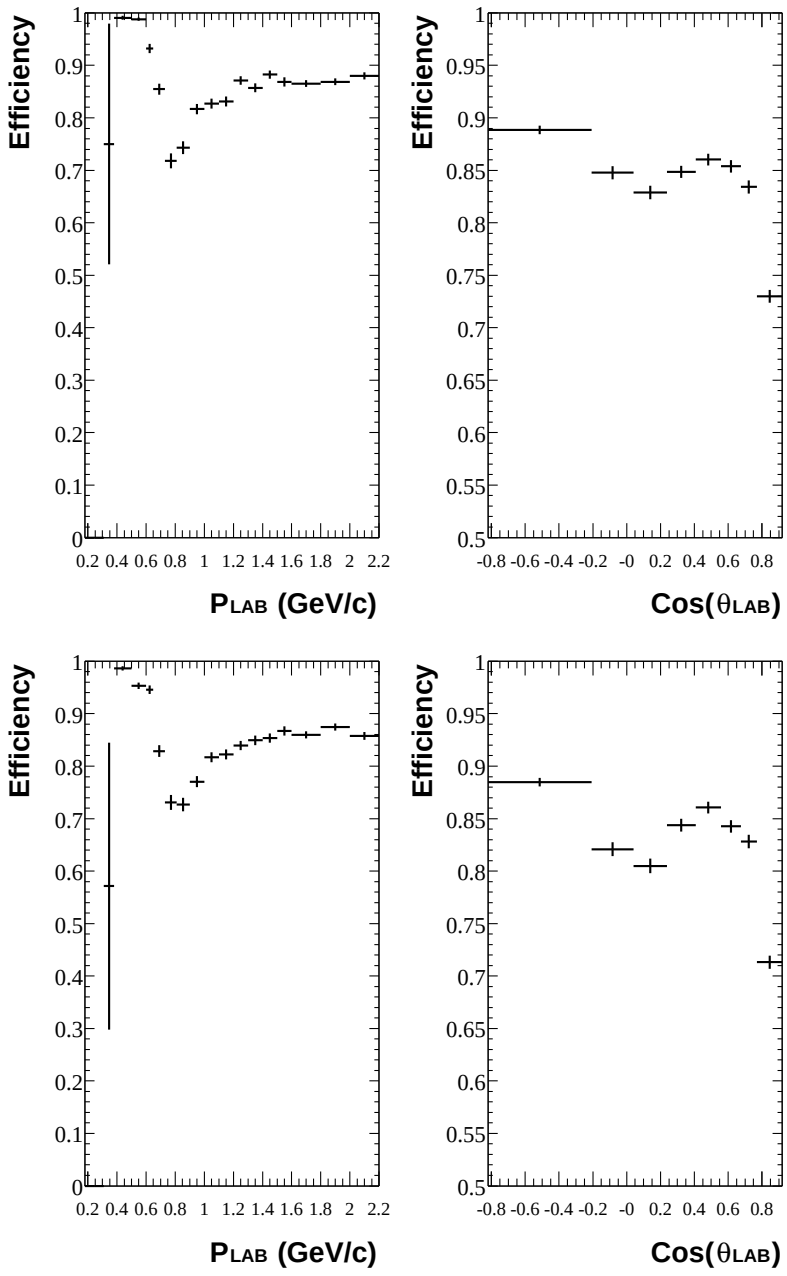

Figure 4.16: Fake selector efficiency on the kaon control samples in data block #1.

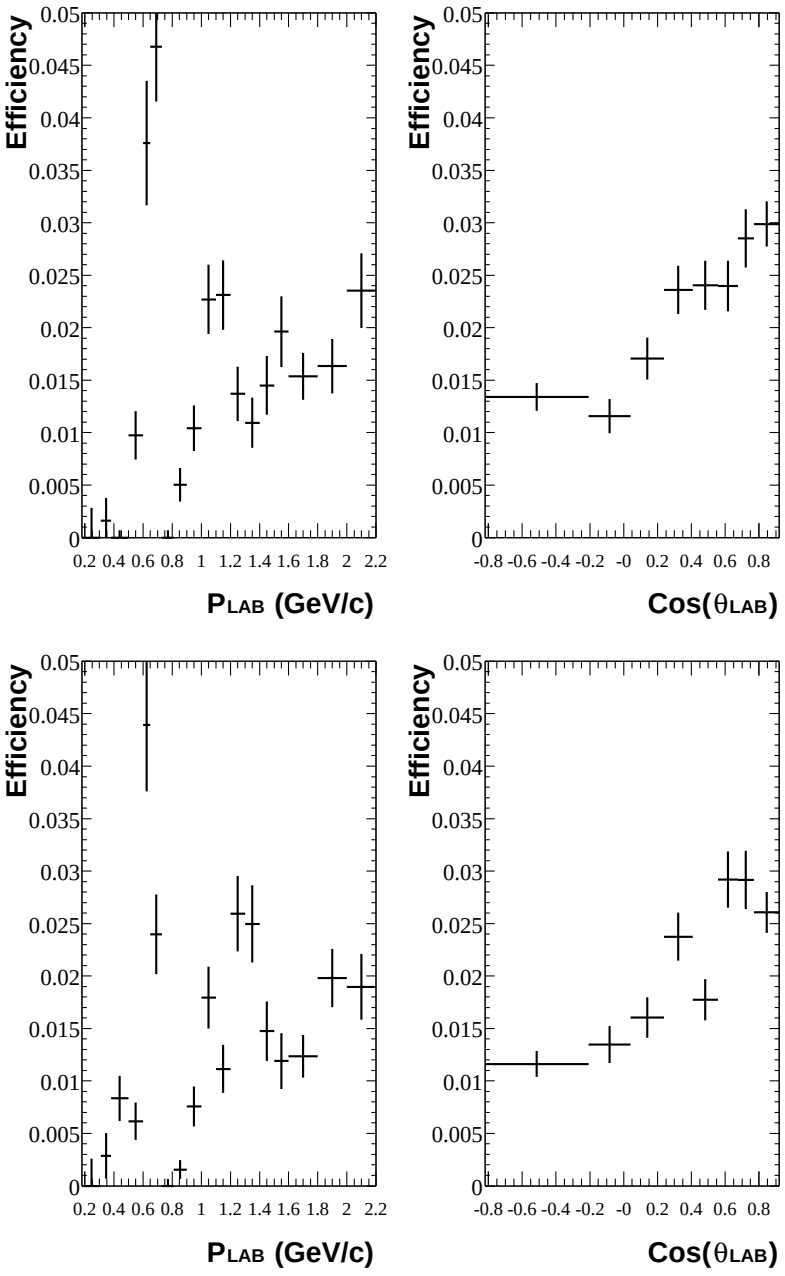

Figure 4.17: Fake selector efficiency on the pion control samples in data block #1.

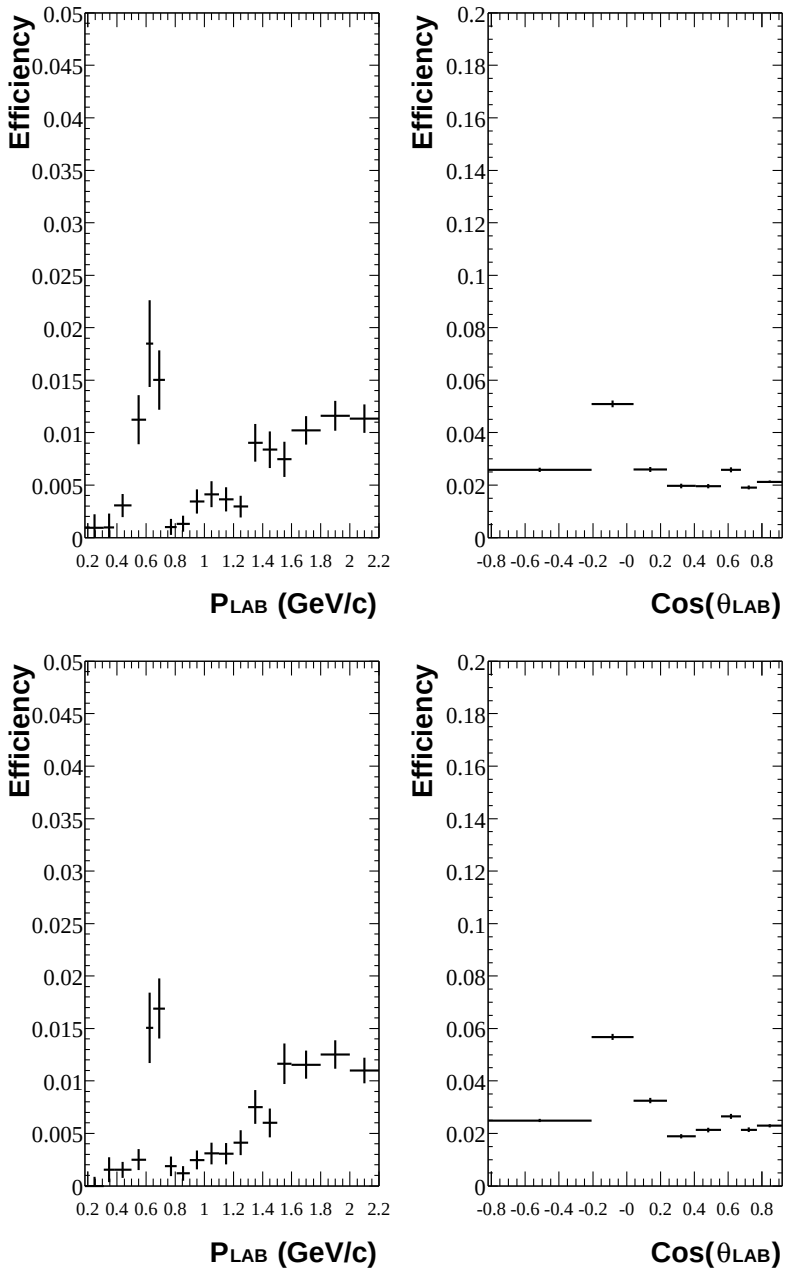

Figure 4.18: Fake selector efficiency on the muon control samples in data block #1.

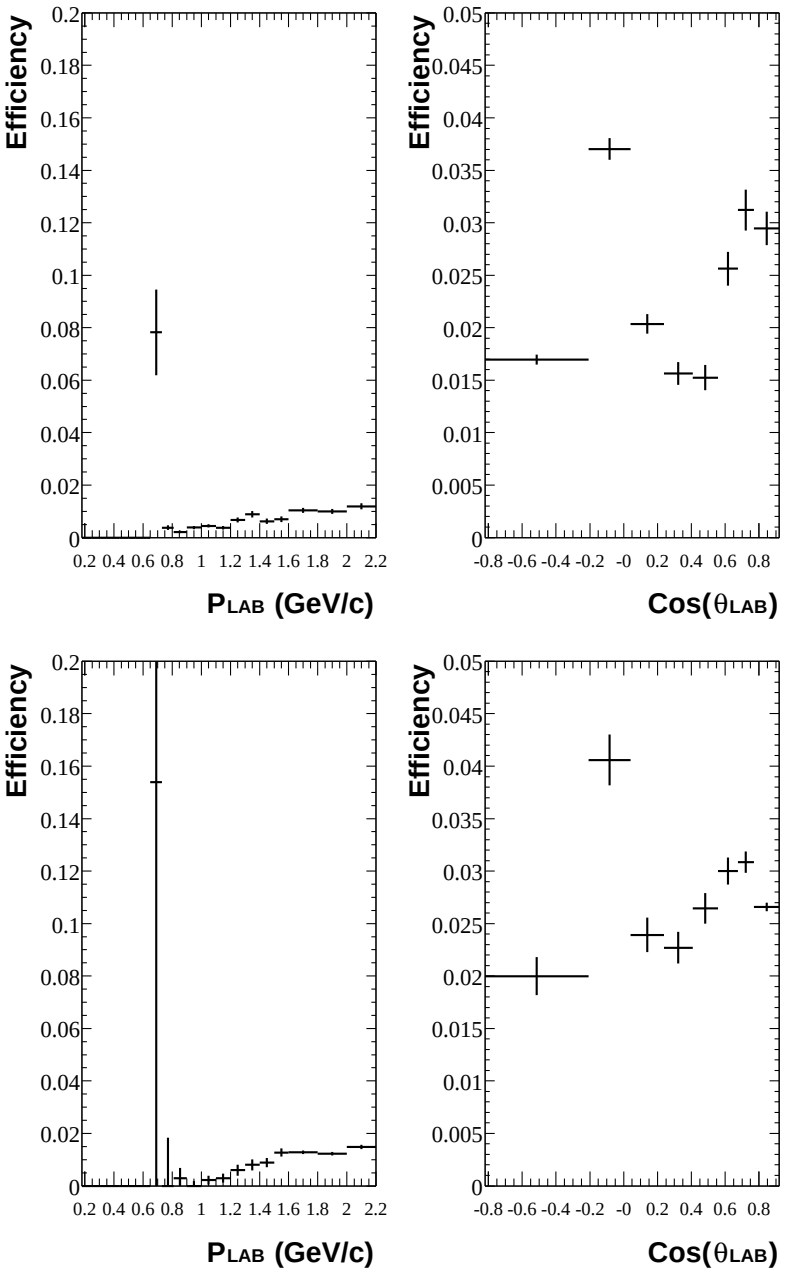

Figure 4.19: Fake selector efficiency on the electron control samples in data block #1.

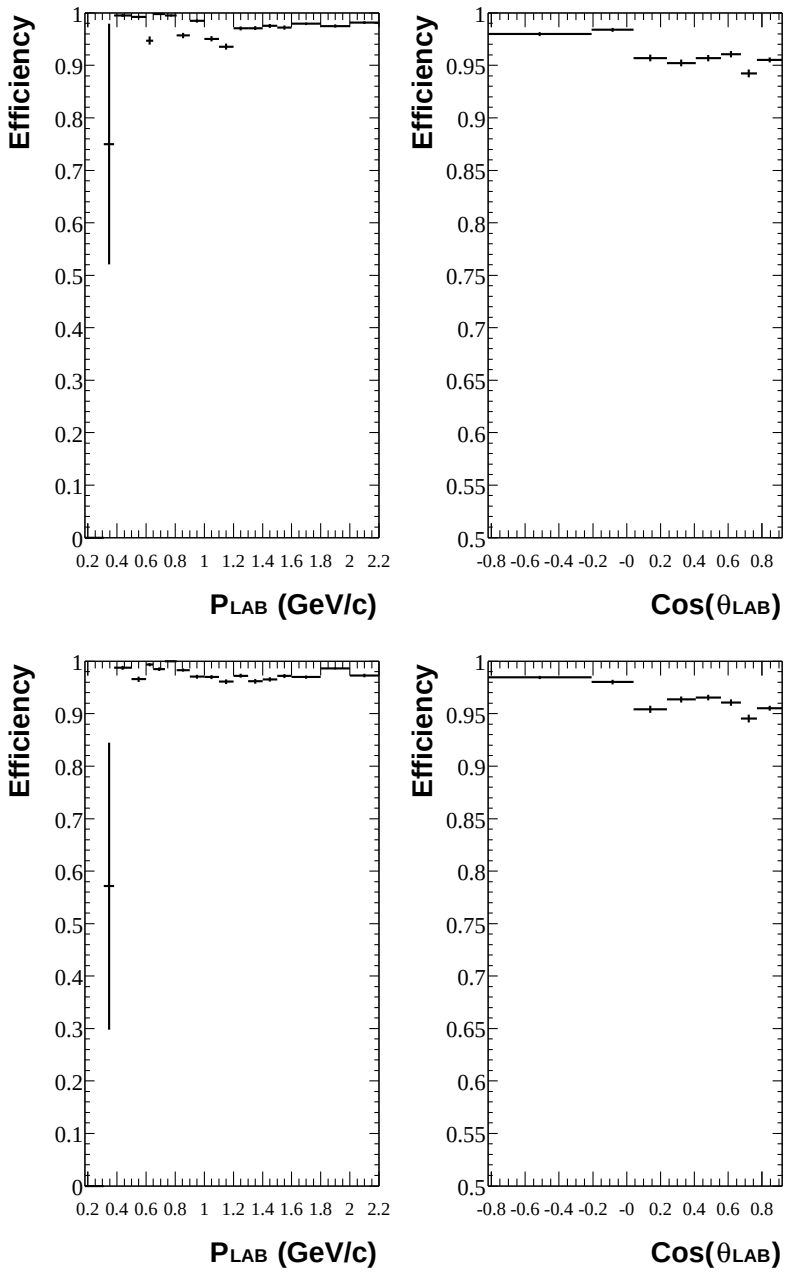

Figure 4.20: NotAPion kaon selector efficiency on the kaon control samples in data block #1.

Chapter 5

Analysis Procedure

5.1 Event Selection

The data in this analysis was collected in 1999 and 2000. The Monte Carlo samples were reconstructed with the same version of *BABAR* reconstruction software as the data. In the first half of the data set, Block #1, the DCH high voltage was set to 1900V. In the second half of the data set, Block #2, the DCH high voltage was adjusted to 1960V. Because of the effect of DCH high voltage on tracking efficiency, the blocks are analyzed independently. Table 5.1 shows both the luminosity of the data sample and the equivalent luminosity of Monte Carlo simulation.

Table 5.1: Luminosity used in this analysis.

Sample	Luminosity
Data – Block 1	$11.8\,\mathrm{fb}^{-1}$
Data – Block 2	$10.8\,\mathrm{fb}^{-1}$
$c\bar{c}$ generic Monte Carlo	$9.2\,\mathrm{fb}^{-1}$

To be selected for analysis, events must pass the hardware trigger and satisfy

hadronic-event selection. The event must contain a charm hadron with momentum in the center of mass frame of 2.5 GeV. The remainder of this section is dedicated to understanding the efficiencies of the trigger and hadronic-event selection. The charm hadron cuts are described in more detail in Section 5.3.

For this analysis, we use Monte Carlo simulation to study the trigger and hadronic event selection efficiencies. Since the final result is a ratio of numbers of events, systematic errors in the determination of these efficiencies tend to cancel.

The hadronic-event selection is based on two cuts and is designed to flag events that might contain hadronic particles. The first cut requires the number of reconstructed tracks to be at least three, rejecting low multiplicity events such as di-muon or Bhabha events. The second cut requires that the 2^{nd} Fox-Wolfram moment be less than 0.98, rejecting very collinear events that might have three or more tracks, such as radiative Bhabha events in which the photon converts to e^+e^-.

With the sample of Monte Carlo events listed in Table 5.1, the efficiency for passing the trigger selection and the hadronic-event selection is calculated. Monte Carlo events are selected in each configuration (see Figures 1.9, 1.10, and 1.11). The efficiency for passing each stage is then the percentage of events that satisfy the trigger or hadronic-event selection requirements for each configuration. The combined efficiency is evaluated by calculating the percentage of events that satisfy both selections. The results are tabulated in Table 5.2. Notice that the combined efficiency is not equal to the product of the individual efficiencies. This behavior is expected; it is known that the two selections are correlated since the trigger is designed to be highly efficient at selecting hadronic events. If the trigger was 100% efficient at selecting hadronic events, the combined efficiency would be equal to the hadronic-event selection efficiency. In actuality, the combined efficiency is close, but slightly lower, than the hadronic-event selection efficiency.

Table 5.2: Efficiency of the different event configurations to pass the hardware trigger, the hadronic-event selection, and the combination of the two. The efficiency for passing both selections takes into account any correlation between the selections. Efficiencies are based on Monte Carlo simulation.

Event Configuration	$\varepsilon_{trigger}$	$\varepsilon_{hadronic}$	$\varepsilon_{trigger+hadronic}$
$\overline{p}\Lambda_c^+ \to pK^-\pi^+ \Longleftrightarrow$	0.9940 ± 0.0004	0.9757 ± 0.0007	0.9736 ± 0.0007
$\Lambda_c^+ \to pK^-\pi^+ \Longleftrightarrow p$	0.9697 ± 0.0040	0.9223 ± 0.0063	0.9135 ± 0.0066
$\overline{p} \Longleftrightarrow \overline{D}$	0.9942 ± 0.0003	0.9710 ± 0.0007	0.9693 ± 0.0007
$\Longleftrightarrow p\overline{D}$	0.9947 ± 0.0008	0.9681 ± 0.0018	0.9667 ± 0.0019

5.2 Antiproton tags

Tag antiprotons are selected with tight proton identification. Below a momentum of $\sim 400\,\mathrm{MeV}/c$, the control samples have limited statistics, leading to large uncertainties in efficiencies and misidentification rates. To avoid this problematic low momentum region, a cut is used requiring tag candidates have $p_{LAB} > 500\,\mathrm{MeV}/c$. No upper cut is applied to the track momentum since the efficiency naturally drops to zero above $2\,\mathrm{GeV}/c$.

Misidentification of tag antiprotons needs specific attention because it can lead to an enhancement in the estimated number of signal and background events. This is in contrast to particle misidentification in charm hadron reconstruction, which will add to the combinatoric background under the charm hadron signal. Data samples enriched in fake antiprotons, called fake-PID samples, are used to determine the contamination in the tag antiproton sample (see Section 5.3). Events in the fake-PID samples are those in which the tag particle fails the loose proton selection and passes the tight kaon selection. Candidates from the fake-PID samples are denoted as "fake-$\overline{p}$ tags", while those from the original particle selection are termed "real-$\overline{p}$

tags." Chapter 4 contains detailed information on the tight kaon, tight proton, and loose proton selection criteria.

Throughout this analysis, tag protons are paired with reconstructed charm hadron candidates. No assumptions are made that the tagged particles should have the same momentum, polar angle, or azimuthal angle distribution in pairings with all types of charm hadrons. Separate efficiencies are evaluated for each charm hadron type, for real- and fake- $\overline{p}$ tags, and for signal and background event topologies. Expected momentum spectra for each event topology are taken from Monte Carlo simulations with JETSET. Particle selection and tracking efficiencies from data are then applied to the simulated spectra to estimate the observed momentum and polar angle distributions of the tag particles.

The procedure described above ensures the analysis relies upon only the shapes and relative normalizations of the Monte Carlo, not on the absolute normalization. The Monte Carlo predictions can be checked later against the final sideband-subtracted distributions from data.

5.3 Charm Hadron Selection

Four different charm hadrons are used in this analysis. The decay modes that are reconstructed are chosen to give high yields. Modes are chosen that have large branching fractions and high efficiency for detection. The following modes have branching fractions of (3-9)% and have only charged particles in the decay chain.

- $\overline{D}^0 \to K^+\pi^-$
- $D^- \to K^+\pi^-\pi^-$
- $D_s^- \to \phi\pi^-, \phi \to K^+K^-$

Table 5.3: Efficiency for a reconstructed D (Λ_c^+) candidate to have a reconstructed vertex with prob(χ^2) > 0.001 (prob(χ^2) > 0.005).

Hadron	$\varepsilon_{p(\chi^2)}$		
	Data Block #1	Data Block #2	M.C.
D^0	0.9958 ± 0.0002	0.9966 ± 0.0002	0.9823 ± 0.0004
$\overline{D}^0$	0.9957 ± 0.0002	0.9968 ± 0.0002	0.9819 ± 0.0004
D^+	0.9829 ± 0.0005	0.9865 ± 0.0004	0.9438 ± 0.0010
D^-	0.9806 ± 0.0005	0.9783 ± 0.0005	0.9475 ± 0.0009
D_s^+	0.9791 ± 0.0016	0.9813 ± 0.0015	0.9412 ± 0.0028
D_s^-	0.9847 ± 0.0013	0.9666 ± 0.0020	0.9520 ± 0.0026
Λ_c^+	0.9565 ± 0.0019	0.9552 ± 0.0020	0.9211 ± 0.0035
$\overline{\Lambda}_c^-$	0.9617 ± 0.0019	0.9583 ± 0.0021	0.9312 ± 0.0035

- $\Lambda_c^+ \to pK^-\pi^+$

The tracks used in reconstruction must satisfy the criteria outlined in Chapter 3. For the $\overline{D}^0$ and D^- reconstruction, the kaon must satisfy the loose kaon selection. For D_s^- reconstruction, at least one of the kaons from the ϕ decay must satisfy loose kaon selection. Furthermore, the proton in the Λ_c^+ decay is required to satisfy the loose proton selection.

Track candidates that pass the tracking and particle identification criteria and have the correct charges are fit to a common vertex. A cut on the probability of the vertex fit is used to further purify the sample. A cut of prob(χ^2) > 0.001 for D candidates and prob(χ^2) > 0.005 for Λ_c^+ candidates removes poorly reconstructed vertices without a substantial loss of efficiency. The efficiency of the cut is determined by fitting the full mass distributions of the hadrons prior to and after applying the cut. Figure 5.1 shows the the hadron candidate mass distributions for candidates that pass and fail the cut. The fit to distribution that passes the cut is shown. The final efficiencies $\varepsilon_{p(\chi^2)}$ are displayed in the plots and summarized in Table 5.3.

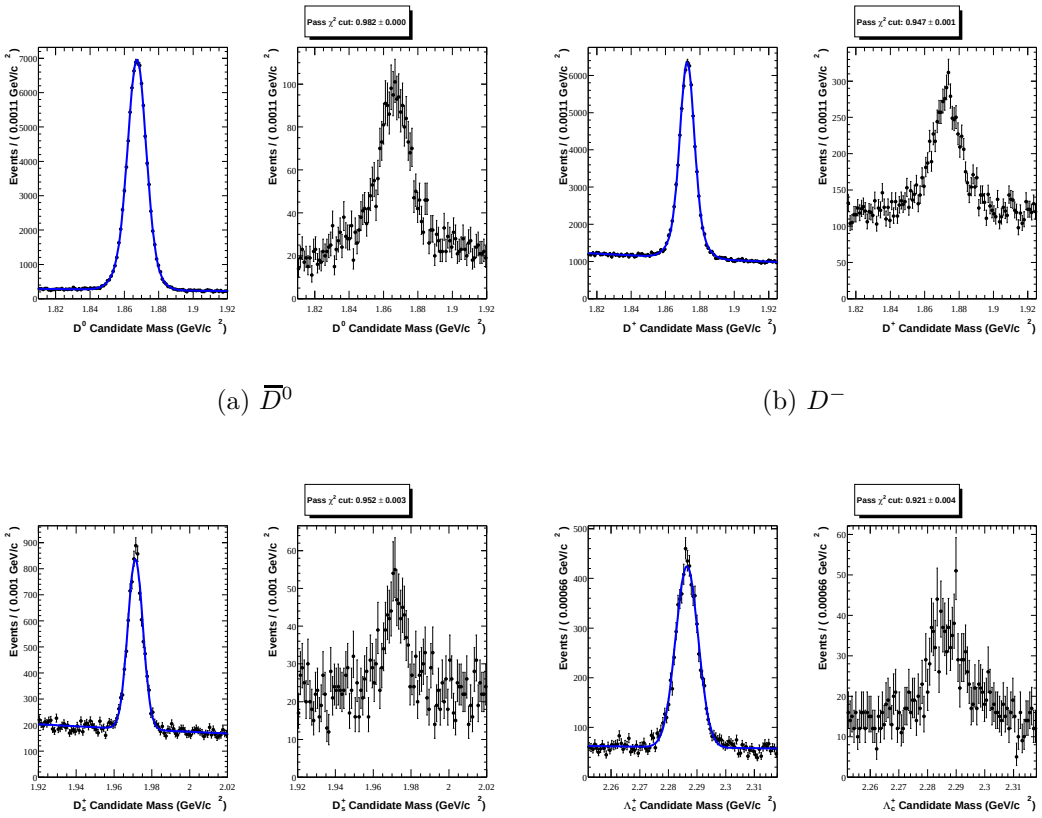

(a) $\overline{D}^0$ (b) D^-

(c) D_s^- (d) Λ_c^+

Figure 5.1: Mass distributions for charm hadron candidates that pass (left) and fail (right) the cut on the prob(χ^2) of the reconstructed decay vertex, in data.

In order to eliminate charm hadrons from B meson decays, as well as to reduce combinatorial background, the charm hadron candidates are required to have momentum in the $\Upsilon(4S)$ rest frame, p_{COM} greater than 2.5 GeV/c. A comparison between data and Monte Carlo show that the Monte Carlo simulation poorly models the center-of-mass momentum spectrum of charm hadrons with tag $\overline{p}$. The data sample is not large enough to independently determine the p_{COM} cut efficiency. Therefore, a technique using a combination of data and Monte Carlo is used. First, the absolute

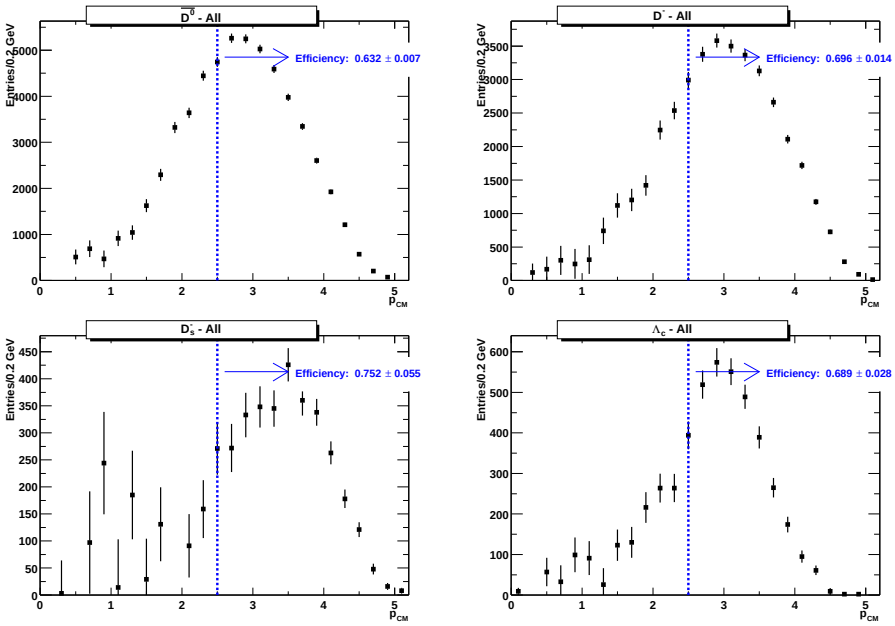

Figure 5.2: Hadron-mass-sideband subtracted center-of-mass momentum distributions of the charm hadron candidates in off-peak data. The cut at 2.5 GeV/c is shown, as well as the efficiency of the cut.

efficiency of the $p_{COM} > 2.5\,\mathrm{GeV}/c$ cut is determined using off-peak data. Figure 5.2 shows the center-of-mass momentum spectrum for the four charm hadrons and efficiency of the $p_{COM} > 2.5\,\mathrm{GeV}/c$ cut. Monte Carlo simulation is then used to determine the efficiency of the cut for a true charm hadron accompanied by a true tag $\overline{p}$ relative to an unaccompanied hadron. Table 5.4 summarizes the relative efficiencies and the final efficiency of the center-of-mass momentum cut for each hadron.

To extract the charm hadron yields from a fit to the candidate mass distributions, the signal mass distribution is assumed to be either a single Gaussian (D_s^-) or the sum of two Gaussians ($\overline{D}^0$, D^-, Λ_c^+). In the D^- case, the two Gaussians are fixed to have the same mean value since it is found that the two means are statistically compatible if the means are fit independently. In all cases, the background mass distribution is

Table 5.4: Calculation of efficiency of $p_{CM} > 2.5\,\mathrm{GeV}/c$ cut for hadrons with tag $\overline{p}$. The first column shows the efficiency of the cut for all hadrons in data, regardless of whether they are accompanied by a tag $\overline{p}$. The second column shows the relative efficiency of the cut for events with and without a tag $\overline{p}$ in Monte Carlo simulation. The background type events, which have a tag $\overline{p}$ opposite a $\overline{D}$ meson or on the same side as a Λ_c^+ baryon, have lower relative efficiencies because those events have extra particles and less kinetic energy available than signal events. The third columns shows the final efficiency obtained by multiplying the numbers in the first two columns.

Event Type	$\varepsilon_{hadron}^{data}$	$\varepsilon_{p+hadron}^{MC}/\varepsilon_{hadron}^{MC}$	$\varepsilon_{p+hadron}$
$\overline{p} \Longleftrightarrow \overline{D}^0 \to K^+\pi^-$	0.632 ± 0.007	0.940 ± 0.005	0.594 ± 0.007
$\Longleftrightarrow \overline{p}D^0 \to K^-\pi^+$	0.632 ± 0.007	0.488 ± 0.009	0.308 ± 0.006
$\overline{p} \Longleftrightarrow D^- \to K^+\pi^-\pi^-$	0.696 ± 0.014	0.906 ± 0.006	0.631 ± 0.013
$\Longleftrightarrow \overline{p}D^+ \to K^-\pi^+\pi^+$	0.696 ± 0.014	0.488 ± 0.009	0.340 ± 0.009
$\overline{p} \Longleftrightarrow D_s^- \to \phi\pi^-$	0.752 ± 0.055	0.957 ± 0.018	0.720 ± 0.054
$\Longleftrightarrow \overline{p}D_s^+ \to \phi\pi^+$	0.752 ± 0.055	0.506 ± 0.034	0.381 ± 0.038
$\overline{p} \Longleftrightarrow \overline{\Lambda}_c^- \to \overline{p}K^+\pi^-$	0.689 ± 0.028	0.771 ± 0.025	0.531 ± 0.028
$\Longleftrightarrow \overline{p}\Lambda_c^+ \to pK^-\pi^+$	0.689 ± 0.028	0.834 ± 0.006	0.575 ± 0.024

assumed to be an exponential.

In the event topologies considered in this analysis, every charm hadron is paired with a $\overline{p}$ or fake-$\overline{p}$ candidate in one of the event hemispheres. In order to study possible systematic effects due to DCH high voltage or charge asymmetries, the sample of hadron-track pairs is then divided into four subsamples based on

- Run block (1 or 2), defined by the DCH high voltage setting;
- Tag track charge (positive or negative).

Because each hadron can be paired with multiple $\overline{p}$ or fake $\overline{p}$ tracks in the same event, care must be taken to use hadron candidates only once to eliminate the possibility of underestimating statistical errors. To avoid multiple counting, the data is subdivided for the fitting procedure. Each hadron candidate is placed into a subsample based on the number of $\overline{p}$ tags and the number of fake $\overline{p}$ tags associated with

Table 5.5: A charm hadron is placed into a subsample based on the number of $\overline{p}$ tags, r, and fake $\overline{p}$ tags, f, associated with it. The yield of each subsample is labeled $Y_{r,f}$

	0 Fake	1 Fake	2 Fakes	...
0 Real	$Y_{0,0}$	$Y_{0,1}$	$Y_{0,2}$	...
1 Real	$Y_{1,0}$	$Y_{1,1}$	$Y_{1,2}$	...
2 Real	$Y_{2,0}$	$Y_{2,1}$	$Y_{2,2}$	...
...	...	...	...	...

it. All subsamples are fit simultaneously for their individual charm hadron yields, and each subsample's yield carries a statistical error from the fit. Because the shape of the peak distribution does not depend on the number of tag particle, the mass distribution shape parameters are shared among the subsamples. Table 5.5 visually shows how the subsample yields can be arranged into a matrix based on the number of $\overline{p}$ and fake $\overline{p}$ tags.

Figure 5.3 displays the final fit to all the charm hadrons in Block #1 of the data. In the joint fit to the subsamples with different numbers of real and fake proton tags, the shape of the signal peak is dominated by the sample with no tag particles. The shape parameters are crucial for determining the signal yields for smaller samples. Table 5.6 summarizes the fitted shape parameters of the signal distributions.

The resulting fit yields can then be added with correct weights to determine the total number of real and fake tagged hadrons:

$$\begin{aligned} N_{obs}^{real} &= \sum_{r=0}^{\infty}\sum_{f=0}^{\infty} r \cdot Y_{rf}, \\ N_{obs}^{fake} &= \sum_{r=0}^{\infty}\sum_{f=0}^{\infty} f \cdot Y_{rf}, \end{aligned} \tag{5.1}$$

where Y_{rf} is the number of signal candidates extracted from the fit to the charm hadron mass distributions for charm hadron candidates associated with r $\overline{p}$ tags and f fake $\overline{p}$ tags. The values of N_{obs}^{real} and N_{obs}^{fake} are then used to calculate the expected number of actual true $\overline{p}$ tags $N_{pid-corrected}^{\overline{p}}$ by inverting the following equation:

$$\begin{pmatrix} N_{obs}^{real} \\ N_{obs}^{fake} \end{pmatrix} = \begin{pmatrix} \varepsilon_{\overline{p}\to real} & \varepsilon_{!\overline{p}\to real} \\ \varepsilon_{\overline{p}\to fake} & \varepsilon_{!\overline{p}\to fake} \end{pmatrix} \begin{pmatrix} N_{pid-corrected}^{\overline{p}} \\ N_{pid-corrected}^{!\overline{p}} \end{pmatrix}. \tag{5.2}$$

The efficiencies in the matrix are described in Section 5.2. The numbers $N_{pid-corrected}^{\overline{p}}$ are the size of the various event subsamples used throughout Sections 7.1- 7.2.

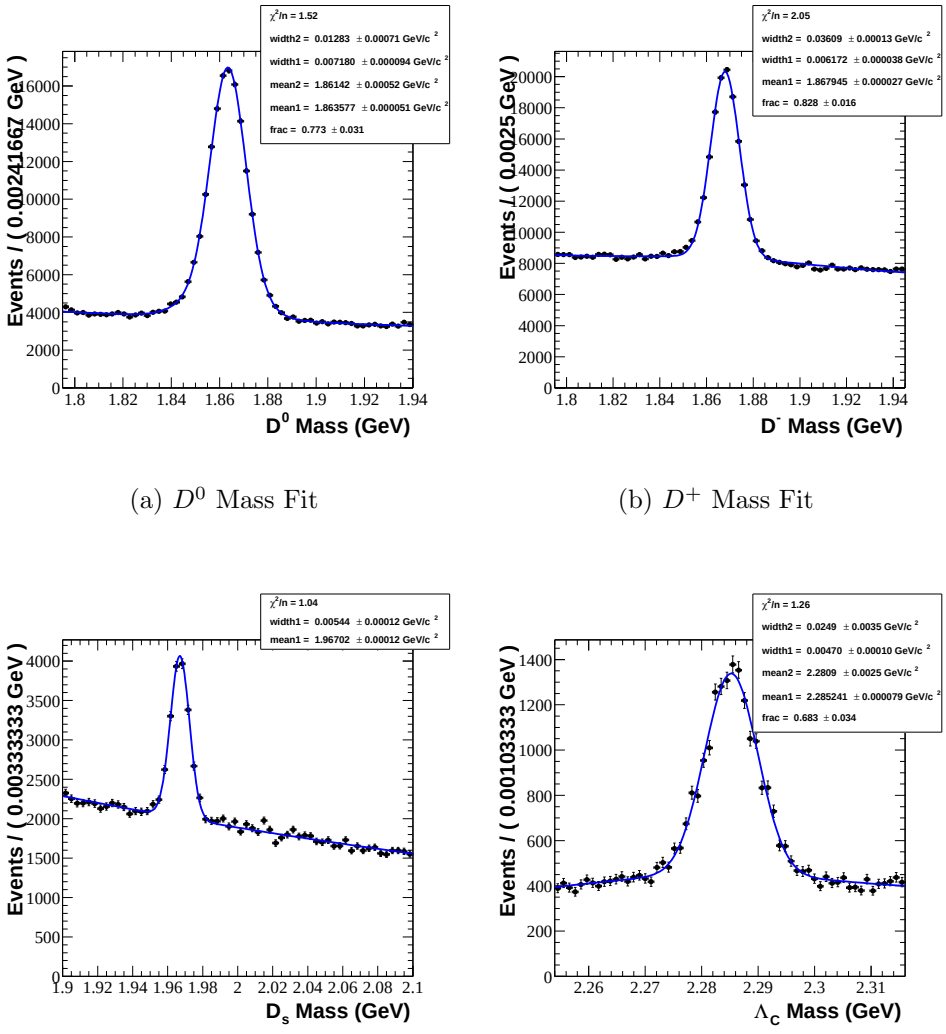

(a) D^0 Mass Fit

(b) D^+ Mass Fit

(c) D_s^+ Mass Fit

(d) Λ_c^+ Mass Fit

Figure 5.3: Fits to full hadron mass distributions for charm hadrons in Block #1 of the data. The parameters for all fits are summarized in Table 5.6. These plots show the combined fit to all the subsample with different numbers of real and fake tag $\overline{p}$.

Table 5.6: Shape parameters from fits to charm hadron mass distributions for candidates used in this analysis.

Particle	Block	mean1 (GeV/c^2)	mean2 (GeV/c^2)	width1 (GeV/c^2)	width2 (GeV/c^2)	frac
D^0	1	1.86358 ± 0.00005	1.8614 ± 0.0005	0.00718 ± 0.00009	0.0128 ± 0.0007	0.77 ± 0.03
D^0	2	1.86347 ± 0.00004	1.8621 ± 0.0003	0.0063 ± 0.0001	0.0114 ± 0.0006	0.71 ± 0.04
$\overline{D}^0$	1	1.86380 ± 0.00005	1.8622 ± 0.0004	0.0071 ± 0.0001	0.0126 ± 0.0008	0.73 ± 0.04
$\overline{D}^0$	2	1.86372 ± 0.00004	1.8614 ± 0.0006	0.00659 ± 0.00009	0.0122 ± 0.0007	0.77 ± 0.03
D^+	1	1.86794 ± 0.00003		0.00617 ± 0.00004	0.0361 ± 0.0001	0.83 ± 0.02
D^+	2	1.86809 ± 0.00004		0.00579 ± 0.00004	0.0379 ± 0.0001	0.88 ± 0.02
D^-	1	1.86887 ± 0.00003		0.00623 ± 0.00003	0.0369 ± 0.0001	0.87 ± 0.02
D^-	2	1.86851 ± 0.00004		0.00580 ± 0.00003	0.0387 ± 0.0001	0.89 ± 0.02
D_s^+	1	1.9670 ± 0.0001		0.0054 ± 0.0001		
D_s^+	2	1.9674 ± 0.0001		0.0052 ± 0.0001		
D_s^-	1	1.96818 ± 0.00006		0.0054 ± 0.0001		
D_s^-	2	1.96751 ± 0.00008		0.0049 ± 0.0001		
Λ_c^+	1	2.28524 ± 0.00008	2.281 ± 0.002	0.0047 ± 0.0001	0.025 ± 0.004	0.68 ± 0.03
Λ_c^+	2	2.28540 ± 0.00008	2.2852 ± 0.0003	0.0038 ± 0.0005	0.006 ± 0.001	0.5 ± 0.3
$\overline{\Lambda}_c^-$	1	2.28560 ± 0.00009	2.283 ± 0.003	0.00470 ± 0.00010	0.020 ± 0.003	0.71 ± 0.03
$\overline{\Lambda}_c^-$	2	2.28558 ± 0.00008	2.287 ± 0.004	0.00448 ± 0.00006	0.034 ± 0.001	0.73 ± 0.03

Chapter 6

Monte Carlo Validation

6.1 Tracking and PID Efficiency Validation

The analysis procedure is validated using Monte Carlo simulated samples described in Section 5.1. The important objective is to verify that the value of $\mathcal{B}(\Lambda_c^+ \to pK^-\pi^+)$ used to generate the Monte Carlo events is the value obtained when applying the full analysis on the simulated events. Additionally, all efficiency calculations are verified using Monte Carlo truth to ensure the analysis can be applied to the data with confidence.

To evaluate the tracking efficiencies for this study, Monte Carlo simulated events are used. Tracking efficiencies are determined by the techniques presented in Section 3. Validation is done by comparing two sets of distributions. The method for validation is described in the following two paragraphs.

First, distributions of particle momentum and polar angle prior to detector simulation are constructed from signal events. These distributions are then weighted according to efficiencies for the particles to pass acceptance, momentum, and tracking cuts. Acceptance and kinematic weights equal one for particles that pass these

analysis cuts and zero for particles that fail the cuts. Tracking weights are applied using the calculated tracking efficiencies for Monte Carlo control samples. In addition, corrections are included for excess protons, as described in Section 3. The correction, which inflates efficiencies slightly, is used simultaneously with the tracking efficiency calculation so correlations between the two are accurately modeled.

A second set of particle momentum and polar angle distributions are created after full detector simulation. A true particle is included in the distributions only if it is matched to a reconstructed track. The matching for a simulated particle is done by finding the reconstructed track that is "closest" in phase space to the desired particle. "Closest" is defined by calculating the χ^2 between the particle's true trajectory and the reconstructed track's trajectory. The trajectory's are compared using errors from the reconstructed track fit.

The two distributions should agree if efficiencies are calculated correctly from the control samples. The upper plots of the figures in Appendix B show a comparison of tag antiproton and hadron daughter momentum and polar angle distributions. The Kolmogorov test, which returns a real number between 0 and 1, is used to evaluate whether the distributions are likely to be the same. A value near zero indicates a high probability that the two samples did *not* originate from the same distribution, whereas two samples that *do* originate from the same distribution will have Kolmogorov test values distributed fairly evenly from 0 to 1. The Kolmogorov test value is shown in each plot. The agreement is found to be quite good.

In addition to single particle momenta, efficiencies may depend on correlations between particle momenta within an event. Because the particles in $c\overline{c}$ events are confined to back-to-back cones in the center-of-mass frame, the particles tend to traverse nearby regions of the detector. Consequently, their efficiencies cannot be considered independently. In addition, events with high multiplicities tend to have lower efficiencies for all particles due to the enhanced combinatorics.

Efficiencies are calculated on an event by event basis, rather than measuring the hadron and tag efficiencies independently then multiplying them. This procedure means that correlations within events are properly taken into account. The acceptance weighting is determined by requiring all tracks be within the detector's fiducial volume. Tracking efficiencies are then the product of all the single particle efficiencies for that event. The lower plots in the figures of Appendix B show the validation of the full event tracking efficiencies. In Table 6.1, the second and fourth columns list the per event tracking efficiencies from control sample studies and Monte Carlo truth matching, respectively.

Validation of the particle identification techniques is performed in a similar manner as the validation of tracking efficiencies. Again, particle momentum and polar angle distributions are created from Monte Carlo prior to detector simulation. In addition to acceptance, kinematic, and tracking weights, particle identification weights are applied. The particle identification weights are the efficiencies calculated in Chapter 4.

The second set of momentum and polar angle distributions is created after detector simulation and application of particle identification selection to reconstructed tracks. Applying the same χ^2 truth-matching procedure used in the tracking validation, distributions are produced for those particles found by the reconstruction algorithms that also pass the particle identification criteria.

The figures of Appendix C show a comparison of the single particle (upper plots) and of the full event (lower plots) tracking and particle identification efficiencies. The third and fifth columns of Table 6.1 list the event tracking and particle identification efficiencies from control sample studies and Monte Carlo truth matching, respectively.

The full analysis is applied separately to the tag proton and tag antiproton samples to detect any charge asymmetry. The final branching fraction is calculated from

Table 6.1: Comparison of tracking and particle identification efficiencies found with two different methods. These efficiencies do not include the kinematic and geometric acceptance. The first column lists the sample name. The second and third columns are the tracking and combined tracking/PID efficiencies calculated using control samples. The fourth and fifth columns are the tracking and combined tracking/PID efficiencies calculated using Monte Carlo truth matching.

Sample	Control Samples		Monte Carlo Truth	
	ε_{trk}	$\varepsilon_{trk+pid}$	ε_{trk}	$\varepsilon_{trk+pid}$
$p \Longleftrightarrow D^0 \to K^-\pi^+$	0.79 ± 0.01	0.59 ± 0.01	0.80 ± 0.01	0.56 ± 0.01
$\Longleftrightarrow p\overline{D}^0 \to K^+\pi^-$	0.81 ± 0.02	0.70 ± 0.02	0.76 ± 0.02	0.62 ± 0.03
$p \Longleftrightarrow D^+ \to K^-\pi^+\pi^+$	0.68 ± 0.01	0.50 ± 0.01	0.66 ± 0.01	0.45 ± 0.01
$\Longleftrightarrow pD^- \to K^+\pi^-\pi^-$	0.68 ± 0.03	0.57 ± 0.03	0.68 ± 0.03	0.54 ± 0.03
$p \Longleftrightarrow D_s^+ \to \phi\pi^+$	0.68 ± 0.03	0.49 ± 0.03	0.66 ± 0.03	0.44 ± 0.03
$\Longleftrightarrow pD_s^- \to \phi\pi^-$	0.65 ± 0.11	0.59 ± 0.11	0.68 ± 0.11	0.68 ± 0.11
$p \Longleftrightarrow \Lambda_c^+ \to pK^-\pi^+$	0.62 ± 0.05	0.40 ± 0.05	0.61 ± 0.05	0.40 ± 0.05
$\Longleftrightarrow p\overline{\Lambda}_c^- \to \overline{p}K^+\pi^-$	0.62 ± 0.01	0.43 ± 0.01	0.62 ± 0.01	0.39 ± 0.01
$\overline{p} \Longleftrightarrow \overline{D}^0 \to K^+\pi^-$	0.77 ± 0.01	0.52 ± 0.01	0.77 ± 0.01	0.49 ± 0.01
$\Longleftrightarrow \overline{p}D^0 \to K^-\pi^+$	0.74 ± 0.02	0.59 ± 0.03	0.74 ± 0.02	0.56 ± 0.03
$\overline{p} \Longleftrightarrow D^- \to K^+\pi^-\pi^-$	0.65 ± 0.01	0.42 ± 0.01	0.63 ± 0.01	0.38 ± 0.01
$\Longleftrightarrow \overline{p}D^+ \to K^-\pi^+\pi^+$	0.64 ± 0.03	0.52 ± 0.03	0.62 ± 0.03	0.45 ± 0.03
$\overline{p} \Longleftrightarrow D_s^- \to \phi\pi^-$	0.65 ± 0.03	0.41 ± 0.03	0.62 ± 0.03	0.36 ± 0.03
$\Longleftrightarrow \overline{p}D_s^+ \to \phi\pi^+$	0.60 ± 0.12	0.48 ± 0.12	0.41 ± 0.12	0.29 ± 0.11
$\overline{p} \Longleftrightarrow \overline{\Lambda}_c^- \to \overline{p}K^+\pi^-$	0.60 ± 0.05	0.30 ± 0.05	0.60 ± 0.05	0.30 ± 0.05
$\Longleftrightarrow \overline{p}\Lambda_c^+ \to pK^-\pi^+$	0.58 ± 0.01	0.39 ± 0.01	0.57 ± 0.01	0.33 ± 0.01

the two samples by independently summing the efficiency corrected estimates of reconstructed $\Lambda_c^+ \to pK^-\pi^+$ decays and produced Λ_c^+ baryons:

$$\begin{aligned} N_{produced\ \Lambda_c^+} &= N^p_{produced\ \Lambda_c^+} + N^{\overline{p}}_{produced\ \Lambda_c^+} \\ N_{\Lambda_c^+ \to pK^-\pi^+} &= N^p_{\Lambda_c^+ \to pK^-\pi^+} + N^{\overline{p}}_{\Lambda_c^+ \to pK^-\pi^+} \\ \mathcal{B}(\Lambda_c^+ \to pK^-\pi^+) &= N_{\Lambda_c^+ \to pK^-\pi^+} / N_{produced\ \Lambda_c^+} \end{aligned} \tag{6.1}$$

The final results of the full analysis on the Monte Carlo simulation are summarized

in Table 6.2, which shows the fitted charm hadron yields and efficiencies. The first two columns display the sample name and the fitted yield. The third column lists the efficiency of the vertex cut in the hadron reconstruction, as described in Section 5.3. The fourth column presents the effective particle identification efficiency, defined as $\varepsilon_{PID} = N_{obs}^{real}/N_{pid-corrected}^{\overline{p}}$ from Equation 5.2. The fifth column lists the average tracking efficiency for each sample. In the sixth column, the tracking and particle identification efficiencies are combined taking into account any correlations between the momentum of the particles in an event. The seventh column shows the combined efficiency of the geometric acceptance cuts and the momentum cuts. The final columns list the efficiency corrected yields for each subsample.

The branching fraction results for each tag charge subsample and for the combined Monte Carlo dataset are calculated using the final yields from Table 6.2:

- Tag proton sample: 0.0366 ± 0.0027
- Tag antiproton sample: 0.0305 ± 0.0021
- Combined: 0.0335 ± 0.0017

The input to the Monte Carlo simulation is 0.0365, a number statistically compatible with the tag proton sample. The disagreement in the tag antiproton sample is discussed next.

Table 6.2: Final yields and efficiencies in analysis of Monte Carlo simulated data. Definitions of the table entries is given in the text.

Sample	Fit Result	ε_{vtx}	ε_{PID}	ε_{trk}	$\varepsilon_{trk+pid}$	$\varepsilon_{Acc.}$	Expected
$\overline{p} \Longleftrightarrow \overline{D}^0 \to K^+\pi^-$	1500.4 ± 32.1	0.98	0.75	0.81	0.60	0.26	9627 ± 206
$\Longleftrightarrow \overline{p}D^0 \to K^-\pi^+$	241.6 ± 16.5	0.98	0.86	0.87	0.75	0.10	3314 ± 226
$\overline{p} \Longleftrightarrow D^- \to K^+\pi^-\pi^-$	805.1 ± 41.7	0.94	0.73	0.69	0.51	0.23	7348 ± 381
$\Longleftrightarrow \overline{p}D^+ \to K^-\pi^+\pi^+$	168.0 ± 17.7	0.94	0.85	0.72	0.62	0.09	3278 ± 345
$\overline{p} \Longleftrightarrow D_s^- \to \phi\pi^-$	101.0 ± 12.2	0.94	0.72	0.70	0.50	0.29	750 ± 91
$\Longleftrightarrow \overline{p}D_s^+ \to \phi\pi^+$	18.5 ± 6.6	0.94	0.91	0.68	0.61	0.08	377 ± 135
$\overline{p} \Longleftrightarrow \overline{\Lambda}_c^- \to \overline{p}K^+\pi^-$	42.4 ± 7.5	0.92	0.65	0.62	0.40	0.20	577 ± 102
$\Longleftrightarrow \overline{p}\Lambda_c^+ \to pK^-\pi^+$	725.5 ± 29.7	0.92	0.70	0.62	0.43	0.22	8260 ± 338
$p \Longleftrightarrow D^0 \to K^-\pi^+$	1360.7 ± 28.8	0.98	0.68	0.77	0.52	0.26	10066 ± 213
$\Longleftrightarrow p\overline{D}^0 \to K^+\pi^-$	193.3 ± 14.9	0.98	0.80	0.74	0.59	0.10	3379 ± 260
$p \Longleftrightarrow D^+ \to K^-\pi^+\pi^+$	677.8 ± 38.4	0.95	0.64	0.65	0.42	0.23	7535 ± 427
$\Longleftrightarrow pD^- \to K^+\pi^-\pi^-$	124.0 ± 15.8	0.95	0.82	0.64	0.52	0.09	2836 ± 361
$p \Longleftrightarrow D_s^+ \to \phi\pi^+$	96.5 ± 15.6	0.95	0.64	0.65	0.41	0.29	854 ± 138
$\Longleftrightarrow pD_s^- \to \phi\pi^-$	0.3 ± 3.1	0.95	0.82	0.60	0.48	0.08	8 ± 80
$p \Longleftrightarrow \Lambda_c^+ \to pK^-\pi^+$	24.8 ± 5.6	0.93	0.52	0.60	0.30	0.20	453 ± 102
$\Longleftrightarrow p\overline{\Lambda}_c^- \to \overline{p}K^+\pi^-$	642.1 ± 26.5	0.93	0.67	0.58	0.39	0.22	8066 ± 333

Table 6.3: Effect of tracking efficiency corrections on results for tag proton sample. Descriptions of the rows and columns can be found in the text.

Sample	Analysis	Truth	Δ (# σ)
$p \Longleftrightarrow D^0 \rightarrow K^-\pi^+$	9627 ± 206	9991	-1.77
$\Longleftrightarrow p\overline{D}^0 \rightarrow K^+\pi^-$	3314 ± 226	3461	-0.65
$p \Longleftrightarrow D^+ \rightarrow K^-\pi^+\pi^+$	7348 ± 381	7370	-0.06
$\Longleftrightarrow pD^- \rightarrow K^+\pi^-\pi^-$	3278 ± 345	2905	1.08
$p \Longleftrightarrow D_s^+ \rightarrow \phi\pi^+$	750 ± 91	785	-0.39
$\Longleftrightarrow pD_s^- \rightarrow \phi\pi^-$	377 ± 135	200	1.31
$p \Longleftrightarrow \Lambda_c^+ \rightarrow pK^-\pi^+$	577 ± 102	418	1.56
$\Longleftrightarrow p\overline{\Lambda}_c^- \rightarrow \overline{p}K^+\pi^-$	8260 ± 338	8877	-1.83
	0.0366 ± 0.0027	0.0365	0.03
$\overline{p} \Longleftrightarrow \overline{D}^0 \rightarrow K^+\pi^-$	9481 ± 274	10059	-2.11
$\Longleftrightarrow \overline{p}D^0 \rightarrow K^-\pi^+$	3066 ± 253	3261	-0.77
$\overline{p} \Longleftrightarrow D^- \rightarrow K^+\pi^-\pi^-$	7031 ± 422	7380	-0.83
$\Longleftrightarrow \overline{p}D^+ \rightarrow K^-\pi^+\pi^+$	2744 ± 428	2795	-0.12
$\overline{p} \Longleftrightarrow D_s^- \rightarrow \phi\pi^-$	718 ± 138	737	-0.14
$\Longleftrightarrow \overline{p}D_s^+ \rightarrow \phi\pi^+$	0 ± 65	211	-3.22
$\overline{p} \Longleftrightarrow \overline{\Lambda}_c^- \rightarrow \overline{p}K^+\pi^-$	447 ± 100	404	0.43
$\Longleftrightarrow \overline{p}\Lambda_c^+ \rightarrow pK^-\pi^+$	7784 ± 334	8904	-3.35
	0.0316 ± 0.0023	0.0365	-2.09

Table 6.3 shows a comparison between the final calculated yields and the Monte Carlo truth. The first two columns are the sample name and the yield from Table 6.2. The third column indicates the true number of events in the Monte Carlo simulated sample. The final column lists the difference between the true number and the measured number of events, in sigma.

A discrepancy in the tag antiproton sample is apparent in the table: many samples have underestimated yields. Both the $\Longleftrightarrow \overline{p}\Lambda_c^+ \rightarrow pK^-\pi^+$ and $\Longleftrightarrow \overline{p}D_s^+ \rightarrow \phi\pi^+$ samples have yields which are over 3 sigma lower than expected. For the $\Longleftrightarrow \overline{p}\Lambda_c^+ \rightarrow pK^-\pi^+$ sample, Figure C.4 shows an overestimation of the efficiency at low momentum. The puzzle here is that the individual particle momentum distributions indicate

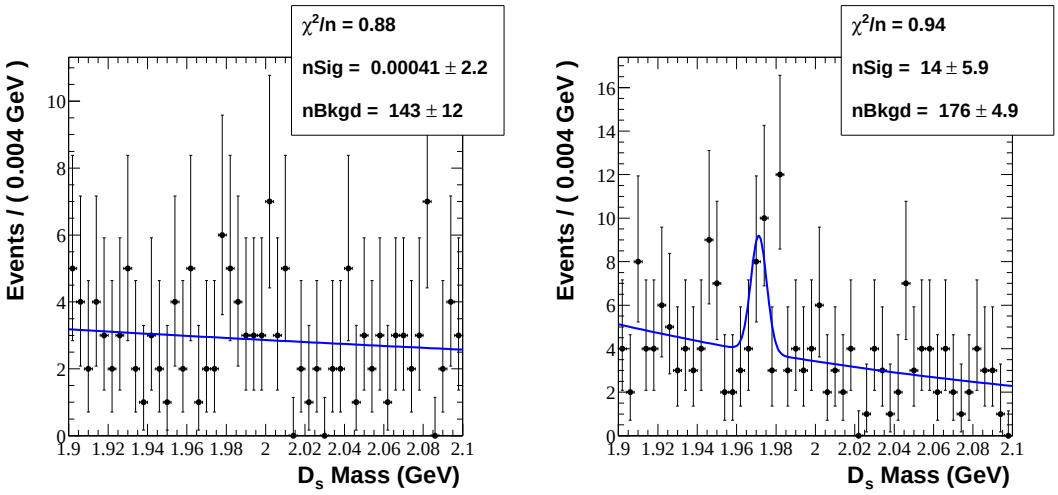

(a) $\Longleftrightarrow \overline{p}D_s^+ \rightarrow \phi\pi^+$ (b) $\Longleftrightarrow pD_s^- \rightarrow \phi\pi^-$

Figure 6.1: Comparison of D_s^+ yield in same side $\overline{p}$ samples from Monte Carlo simulated data. The lack of D_s^+ candidates in the $\overline{p}$ sample is a source of discrepancy between true and estimated yields in the Monte Carlo validation of the analysis.

that tracking and particle identification efficiencies are correct.

In the $\Longleftrightarrow \overline{p}D_s^+ \rightarrow \phi\pi^+$ sample, the missing yield is due to the fact that no events were reconstructed. Monte Carlo truth matching indicates that four events should have passed the analysis criteria. However, this signal is not evident in the large combinatorial background. Figure 6.1 shows this subsample of events and its charge conjugate sample.

The discrepancy in the tag antiproton sample stems from a misunderstanding in either the interactions of antiprotons in matter or in the tracking of antiproton candidates. The analysis in data does not show such a striking difference between tag antiprotons and tag protons, so the cause may be to do problems in the Monte Carlo simulation. An estimation of the systematic effect from poor antiproton simulation

is undertaken in Section 8.4.

Chapter 7

Analysis Results

7.1 Counting Produced Λ_c^+ Baryons

The number of produced Λ_c^+ baryons is determined by studying events that contain a c +baryon system. First, $c\overline{c}$ events are selected that have an $\overline{p}$ in the hemisphere opposite a $\overline{D}$ meson. Since a c +baryon system can be produced with any $\overline{D}$ meson, we need to reconstruct at least one mode for each of the three weakly decaying $\overline{D}$ mesons ($\overline{D}^0$, D^-, D_s^-) to ensure we have a known subsample of produced c +baryon systems. The number of c +baryon systems created in the Λ_c^+ production topology of Figure 1.8 is determined from the following equation.

$$
\begin{aligned}
N_{c+baryon} = & \frac{N^{\overline{p}}_{pid-corrected}(\overline{p} \Longleftrightarrow \overline{D}^0)}{\mathcal{B}(\overline{D}^0 \to K^+\pi^-) \cdot \varepsilon^{\overline{p}\Longleftrightarrow\overline{D}^0}_{EventSelection} \cdot \varepsilon^{\overline{p}\Longleftrightarrow\overline{D}^0}_{reco-D^0}} + \\
& \frac{N^{\overline{p}}_{pid-corrected}(\overline{p} \Longleftrightarrow D^-)}{\mathcal{B}(D^- \to K^+\pi^-\pi^-) \cdot \varepsilon^{\overline{p}\Longleftrightarrow D^-}_{EventSelection} \cdot \varepsilon^{\overline{p}\Longleftrightarrow D^-}_{reco-D^-}} + \\
& \frac{N^{\overline{p}}_{pid-corrected}(\overline{p} \Longleftrightarrow D_s^-)}{\mathcal{B}(D_s^- \to \phi\pi^-) \cdot \mathcal{B}(\phi \to K^+K^-) \cdot \varepsilon^{\overline{p}\Longleftrightarrow D_s^-}_{EventSelection} \cdot \varepsilon^{\overline{p}\Longleftrightarrow D_s^-}_{reco-D_s^-}}
\end{aligned}
\tag{7.1}
$$

Table 7.1: Fit yields and efficiencies for Block #1. A description of each column can be found in the text.

Sample	Fit Result	ε_{vtx}	ε_{PID}	ε_{trk}	$\varepsilon_{trk+pid}$	$\varepsilon_{Acc.}$	Expected
$\overline{p} \Longleftrightarrow \overline{D}^0 \rightarrow K^+\pi^-$	1510.0 ± 53.6	1.00	0.66	0.75	0.50	0.26	11937 ± 424
$\Longleftrightarrow \overline{p}D^0 \rightarrow K^-\pi^+$	210.7 ± 26.7	1.00	0.78	0.81	0.63	0.10	3458 ± 438
$\overline{p} \Longleftrightarrow D^- \rightarrow K^+\pi^-\pi^-$	957.8 ± 64.8	0.98	0.65	0.62	0.41	0.24	9854 ± 666
$\Longleftrightarrow \overline{p}D^+ \rightarrow K^-\pi^+\pi^+$	268.5 ± 38.4	0.98	0.78	0.65	0.52	0.09	5633 ± 806
$\overline{p} \Longleftrightarrow D_s^- \rightarrow \phi\pi^-$	103.2 ± 15.6	0.98	0.65	0.62	0.41	0.31	826 ± 125
$\Longleftrightarrow \overline{p}D_s^+ \rightarrow \phi\pi^+$	21.8 ± 13.9	0.98	0.85	0.61	0.52	0.09	459 ± 292
$\overline{p} \Longleftrightarrow \overline{\Lambda}_c^- \rightarrow \overline{p}K^+\pi^-$	65.8 ± 15.2	0.96	0.58	0.57	0.33	0.20	1032 ± 238
$\Longleftrightarrow \overline{p}\Lambda_c^+ \rightarrow pK^-\pi^+$	1275.7 ± 57.1	0.96	0.61	0.56	0.34	0.23	17555 ± 786
$p \Longleftrightarrow D^0 \rightarrow K^-\pi^+$	983.5 ± 45.4	1.00	0.56	0.72	0.40	0.26	9591 ± 442
$\Longleftrightarrow p\overline{D}^0 \rightarrow K^+\pi^-$	122.8 ± 19.3	1.00	0.71	0.69	0.49	0.10	2628 ± 414
$p \Longleftrightarrow D^+ \rightarrow K^-\pi^+\pi^+$	611.1 ± 42.2	0.98	0.52	0.59	0.30	0.24	8396 ± 579
$\Longleftrightarrow pD^- \rightarrow K^+\pi^-\pi^-$	43.2 ± 17.6	0.98	0.72	0.58	0.42	0.09	1128 ± 459
$p \Longleftrightarrow D_s^+ \rightarrow \phi\pi^+$	48.8 ± 12.6	0.98	0.55	0.58	0.32	0.31	496 ± 128
$\Longleftrightarrow pD_s^- \rightarrow \phi\pi^-$	5.6 ± 5.8	0.98	0.72	0.54	0.38	0.09	160 ± 165
$p \Longleftrightarrow \Lambda_c^+ \rightarrow pK^-\pi^+$	17.9 ± 7.2	0.96	0.41	0.54	0.21	0.20	430 ± 174
$\Longleftrightarrow p\overline{\Lambda}_c^- \rightarrow \overline{p}K^+\pi^-$	1272.1 ± 57.9	0.96	0.55	0.52	0.29	0.23	20218 ± 920

where $N_{pid-corrected}$ are the pid-corrected yields from Equation 5.2, $\varepsilon_{EventSelection}$ are the event-selection efficiencies tabulated in Table 5.2, and ε_{reco-X} are the $\overline{D}$ meson reconstruction efficiencies from the signal configurations in Tables 7.1 and 7.2.

Figure A.1 in Appendix A shows the fits to the invariant mass distribution in Run Block 1 of $\overline{D}$ mesons opposite one real antiproton tag and zero fake $\overline{p}$ tags. Similar fits were done for all numbers of real antiproton and fake antiproton tags. Tables 7.1 and 7.2 list the final yields from the fits for Blocks #1 and #2, respectively.

In order to determine the number of Λ_c^+ baryons produced in the c +baryon sample, the fraction of events that do not contain Λ_c^+ baryons must be estimated. As described in Section 1.6, there are two sources of backgrounds: events with two D mesons and two non-charm baryons (Figure 1.9(a)) and events in which a Ξ_c is produced (Figure 1.9(b)).

Table 7.2: Fit yields and efficiencies for Block #2. A description of each column can be found in the text.

Sample	Fit Result	ε_{vtx}	ε_{PID}	ε_{trk}	$\varepsilon_{trk+pid}$	$\varepsilon_{Acc.}$	Expected
$\overline{p} \Longleftrightarrow \overline{D}^0 \to K^+\pi^-$	1384.6 ± 59.4	1.00	0.65	0.79	0.51	0.26	10563 ± 453
$\Longleftrightarrow \overline{p}D^0 \to K^-\pi^+$	258.0 ± 26.4	1.00	0.78	0.85	0.67	0.10	4009 ± 410
$\overline{p} \Longleftrightarrow D^- \to K^+\pi^-\pi^-$	890.2 ± 54.2	0.99	0.63	0.68	0.43	0.24	8521 ± 519
$\Longleftrightarrow \overline{p}D^+ \to K^-\pi^+\pi^+$	172.1 ± 31.2	0.99	0.78	0.71	0.56	0.09	3337 ± 605
$\overline{p} \Longleftrightarrow D_s^- \to \phi\pi^-$	87.9 ± 38.6	0.98	0.65	0.68	0.44	0.31	649 ± 285
$\Longleftrightarrow \overline{p}D_s^+ \to \phi\pi^+$	0.0 ± 6.2	0.98	0.85	0.66	0.56	0.09	0 ± 121
$\overline{p} \Longleftrightarrow \overline{\Lambda}_c^- \to \overline{p}K^+\pi^-$	54.5 ± 11.8	0.96	0.56	0.61	0.34	0.20	823 ± 178
$\Longleftrightarrow \overline{p}\Lambda_c^+ \to pK^-\pi^+$	1254.3 ± 55.8	0.96	0.59	0.61	0.36	0.23	16298 ± 725
$p \Longleftrightarrow D^0 \to K^-\pi^+$	886.2 ± 40.7	1.00	0.57	0.76	0.43	0.26	8116 ± 373
$\Longleftrightarrow p\overline{D}^0 \to K^+\pi^-$	82.9 ± 18.3	1.00	0.70	0.73	0.51	0.10	1696 ± 374
$p \Longleftrightarrow D^+ \to K^-\pi^+\pi^+$	655.8 ± 40.0	0.98	0.53	0.64	0.33	0.24	8230 ± 502
$\Longleftrightarrow pD^- \to K^+\pi^-\pi^-$	130.7 ± 27.0	0.98	0.72	0.63	0.45	0.09	3140 ± 648
$p \Longleftrightarrow D_s^+ \to \phi\pi^+$	52.4 ± 11.6	0.97	0.55	0.63	0.35	0.31	498 ± 110
$\Longleftrightarrow pD_s^- \to \phi\pi^-$	2.2 ± 19.6	0.97	0.72	0.59	0.41	0.09	59 ± 530
$p \Longleftrightarrow \Lambda_c^+ \to pK^-\pi^+$	16.3 ± 5.9	0.96	0.40	0.59	0.23	0.20	367 ± 134
$\Longleftrightarrow p\overline{\Lambda}_c^- \to \overline{p}K^+\pi^-$	846.9 ± 38.8	0.96	0.55	0.57	0.32	0.23	12430 ± 570

7.1.1 $\overline{p}D \Longleftrightarrow N\overline{D}$ Background

The $\overline{p}D \Longleftrightarrow N\overline{D}$ source of background can be determined by studying $c\overline{c}$ events that have an $\overline{p}$ in the same hemisphere as a D meson.

$$
\begin{aligned}
N_{\overline{p}D \Longleftrightarrow N\overline{D}} = & \frac{N^{\overline{p}}_{pid-corrected}(\overline{p}D^0 \Longleftrightarrow)}{\mathcal{B}(\overline{D}^0 \to K^+\pi^-) \cdot \varepsilon^{\overline{p}D^0 \Longleftrightarrow}_{EventSelection} \cdot \varepsilon^{\overline{p}D^0 \Longleftrightarrow}_{reco-D^0}} + \\
& \frac{N^{\overline{p}}_{pid-corrected}(\overline{p}D^+ \Longleftrightarrow)}{\mathcal{B}(D^- \to K^+\pi^-\pi^-) \cdot \varepsilon^{\overline{p}D^+ \Longleftrightarrow}_{EventSelection} \cdot \varepsilon^{\overline{p}D^+ \Longleftrightarrow}_{reco-D^+}} + \\
& \frac{N^{\overline{p}}_{pid-corrected}(\overline{p}D_s^+ \Longleftrightarrow)}{\mathcal{B}(D_s^- \to \phi\pi^-) \cdot \mathcal{B}(\phi \to K^+K^-) \cdot \varepsilon^{\overline{p}D_s^+ \Longleftrightarrow}_{EventSelection} \cdot \varepsilon^{\overline{p}D_s^+ \Longleftrightarrow}_{reco-D_s^+}}
\end{aligned}
\tag{7.2}
$$

where the notation is the same as described for Equation 7.1, except that ε_{reco-X} refers to the background configurations of Tables 7.1 and 7.2. Figure A.2 in Appendix A shows the fits to the observed number of D mesons reconstructed on the same-side

as a $\overline{p}$ for exactly one tag and zero fake tags.

7.1.2 Ξ_c Background

Because none of the Ξ_c baryons have known absolute branching fractions, no experiment has measured the absolute or relative production rates of the Ξ_c baryons in e^+e^- collisions. Thus, to understand how much the Λ_c^+ production has been overestimated, QCD models must be used. The most well tested models are JETSET [20], HERWIG [21], and UCLA [22]. The models are generally tuned for light-quark hadrons produced at the Z pole [23]; however, all have problems with baryon production. The best agreement with data for production rates of light quark hadrons is found in JETSET, which uses a highly parameterized string model of fragmentation and hadronization. Because of its large number of parameters, JETSET is highly tunable and has limited predictive power. The UCLA model is a modified version of JETSET with fewer parameters. It outperforms than JETSET for light-quark baryons, but is less reliable for strange and charm quark baryons. HERWIG models dynamics with the more tightly constrained cluster model and is thought to provide a better physical description of QCD processes. However, HERWIG does not model the decay of heavy clusters appropriately and overestimates heavy quark and baryon production. For this analysis, the choice of JETSET is the optimal since it outperforms both HERWIG and UCLA in its prediction of Λ_c^+ production and its prediction of the ratio of Λ and Ξ production rates [24]. It is also readily available for use in the *BABAR* software framework.

One million events were generated of $u\overline{u}$+$d\overline{d}$, $s\overline{s}$, and $c\overline{c}$ each to study baryon multiplicities in continuum events. No detector simulation was needed for this study. When the generated samples were combined in a ratio of $ud : s\overline{s} : c\overline{c} = 1.74 : 0.35 : 1.3$, corresponding to the expected relative cross sections [25], the rate of Ξ_c production

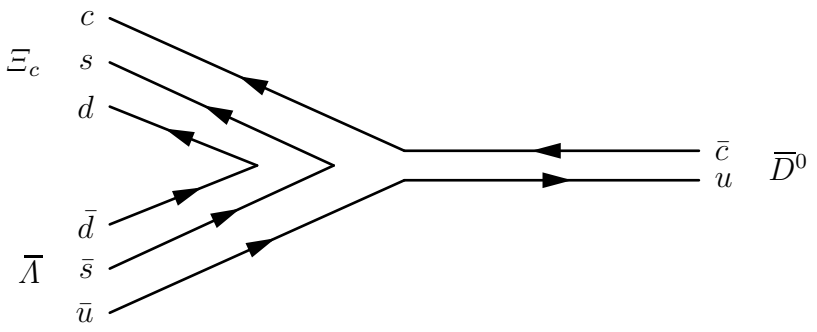

Figure 7.1: Quark diagram showing how a $\bar{\Lambda}$ baryon might be produced with a Ξ_c baryon and a $\overline{D}$ meson. Detection of the $\bar{\Lambda}$ may be useful in rejecting $\overline{D}$ events with undetected Ξ_c baryons.

to Λ_c^+ production was found to be 0.144.

As a cross-check, the strange sector prediction was verified. JETSET predicts the rate of Ξ production to be 0.163 times that of Λ production. Experimentally, this number has been measured to be 0.15 ± 0.02 [1], in strong agreement with the prediction.

Given the large fraction of Ξ_c baryons predicted by JETSET and the systematic uncertainty that comes from relying on a model, a technique to suppress the Ξ_c background was investigated. In events containing a Ξ_c baryon, there is an additional strange quark pair present compared to a similar Λ_c^+ event. There is a high probability that the $\overline{s}$ quark produced in the fragmentation will become part of a $\overline{\Lambda}$ or a $\overline{\Sigma}$ baryon. The Feynman diagram depicting $\overline{\Lambda}$ production is shown in Figure 7.1. Many times, the strange baryon will decay into an $\overline{p}$, which will cause the event to be analyzed as a Λ_c^+ production event.

Figure 7.2 illustrates the generated lab momentum distribution of $\overline{p}$'s in Ξ_c and Λ_c^+ events, showing the individual contributions from four sources: prompt fragmentation, $\overline{\Delta}$ decays, $\overline{\Lambda}$ decays, and $\overline{\Sigma}$ decays. The $\overline{p}$'s from prompt fragmentation are an unremovable source of background because they have no kinematic properties that

differ significantly from the tag $\overline{p}$'s in Λ_c^+ events. Luckily, they are very few. The $\overline{p}$'s from strong $\overline{\Delta}$ decays are also difficult to identify because of the $\overline{\Delta}$ resonance's large decay width and corresponding short lifetime.

In contrast, $\overline{p}$'s from strange baryon decays are identifiable, making them easier to remove. These $\overline{p}$'s can have significant impact parameter with respect to the interaction point due to the relatively long lifetime of the strange baryons. Additionally, the small decay widths allow the strange baryons to be identified with relatively high purity.

To examine the possibility of removing this source of $\overline{p}$'s, the $\overline{\Lambda}$ state was studied. The $\overline{\Lambda}$ state was chosen for three reasons. First, it is the most prolific contaminator (68%: see Figure 7.2) of the sample, making it the best candidate for removal. Second, it has a small width, allowing for a clean veto using a simple mass cut. Third, it is an isospin singlet, and therefore always has a charged pion accompanying the $\overline{p}$; the $\overline{\Sigma}$ and $\overline{\Delta}$ states are isospin multiplets, which decay to neutral pions a large fraction of the time.

Of the Ξ_c contamination with an $\overline{p}$ from $\overline{\Lambda} \to \overline{p}\pi^-$, only 57% could be identified correctly in Monte Carlo simulated data. The $\overline{\Lambda}$ candidates studied were those with a decay $\overline{p}$ on the same side of the event as the Ξ_c, passing the tight proton selector. In addition, the accompanying $\overline{D}$ was required to be on the opposite side of the event and have at least 2.7 GeV of momentum in the center of mass of the event. Three features of the $\overline{\Lambda}$ candidates prevented more efficient reconstruction. First, approximately 15% of the candidates had a daughter π^+ that did not enter the fiducial volume of the *BABAR* detector. Second, the daughter π^+ did not have a large p_T and so was not reconstructed efficiently. Third, the decay vertex of the $\overline{\Lambda}$ was beyond the third layer of the SVT, also preventing efficient reconstruction of the low p_T π^+'s. Figure 7.3 illustrates the latter two effects.

This study concludes that it is not feasible to remove the Ξ_c contamination by

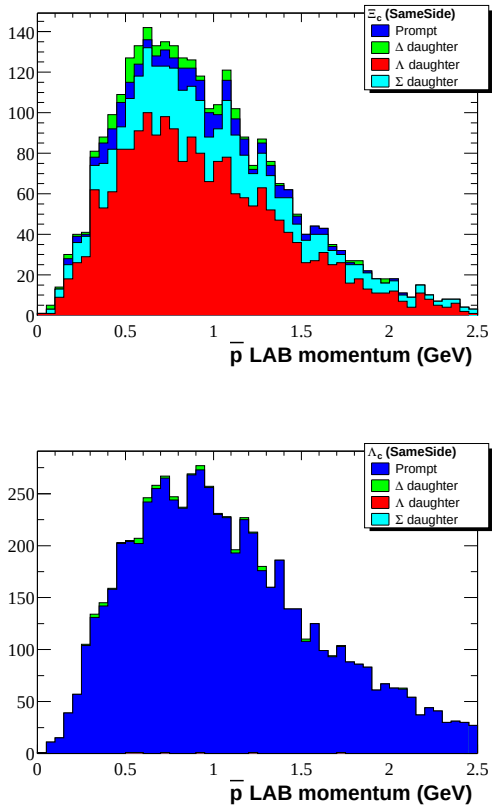

Figure 7.2: Cumulative histograms of the $\overline{p}$ momentum spectrum and its composition in JETSET-generated Ξ_c (top) and Λ_c^+ (bottom) events with $\overline{D}$ $p_{COM} > 2.7\,\mathrm{GeV}$.

reconstructing strange baryons. While strange baryons are predicted by the JETSET model to be present in a large fraction of the contaminating events, it is not possible to efficiently remove them. Attempting to partially remove the Ξ_c events would only lead to further model dependence, through estimation of the strange baryon production rates, in interpreting the final result.

Because no model independent determination of the Ξ_c background can be made, the results of the analysis depend on the estimation of this background. Therefore,

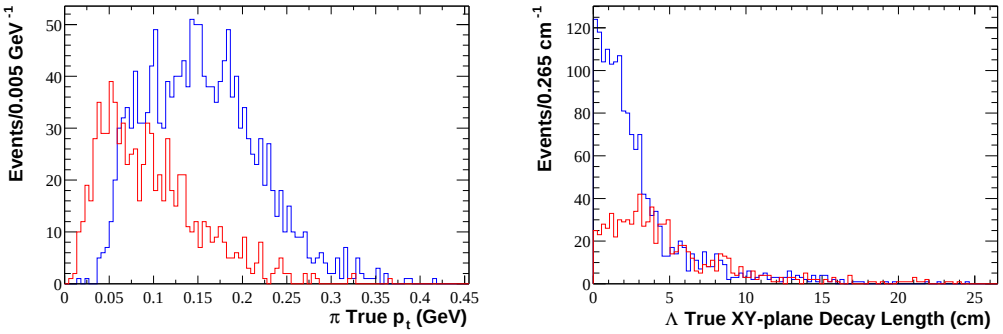

Figure 7.3: Properties of pions from $\overline{\Lambda}$ baryon decays in Monte Carlo simulated events with a Ξ_c and high momentum $\overline{D}$. The solid blue histogram represents those pions that were reconstructed; the dashed red histogram represents those pions that were not reconstructed. Pions were not reconstructed because the $\overline{\Lambda}$ decay vertex was outside the inner silicon wafers or because the transverse momentum was too small.

the results of this analysis are presented in terms of the model independent quantity:

$$\begin{aligned} R &= \mathcal{B}(\Lambda_c^+ \to pK^-\pi^+)/(1+C), \\ C &= \frac{\sigma(\overline{p}\Xi_c \Longleftrightarrow \overline{D})}{\sigma(\overline{p}\Lambda_c^+ \Longleftrightarrow \overline{D})}. \end{aligned} \tag{7.3}$$

The correction factor C will be estimated using JETSET. Future experiments could precisely measure the physical value of C and apply the correction to the result for R.

7.2 Counting $\Lambda_c^+ \to pK^-\pi^+$ Decays

The second number needed for the absolute branching fraction is the number of $\Lambda_c^+ \to pK^-\pi^+$ decays that occur in "$\overline{p} \Longleftrightarrow \overline{D}$" events. In the assumed production topology, the Λ_c^+ is found in the *same* hemisphere as the $\overline{p}$. Since reconstructing both a $\overline{D}$ and a Λ_c^+ decay in the same event is very inefficient, the condition that a $\overline{D}$ be

found is relaxed. The $\overline{D}$ is assumed present if an $\overline{p}$ and Λ_c^+ are reconstructed in the same hemisphere. This assumption will leads to additional background that will be studied. Figure A.3 in Appendix A shows the fit results for the Λ_c^+ mass peaks with a single $\overline{p}$ tag in the same hemisphere and no fake tags. Tables 7.1 and 7.2 tabulate the results of the full fit. The following equation is then used to calculate the number of Λ_c^+ baryons produced in the same hemisphere as a $\overline{p}$:

$$N_{(\overline{p},\Lambda_c^+ \to pK^-\pi^+ \Longleftrightarrow)} = \frac{N^{\overline{p}}_{pid-corrected}(\overline{p}\Lambda_c^+ \Longleftrightarrow)}{\varepsilon^{\overline{p}\Lambda_c^+ \Longleftrightarrow}_{EventSelection} \cdot \varepsilon^{\overline{p}\Lambda_c^+ \Longleftrightarrow}_{reco-\Lambda_c^+}}. \tag{7.4}$$

7.2.1 $\overline{p}\Lambda_c^+ \Longleftrightarrow N\overline{\Lambda}_c^-$ Background

Not requiring a reconstructed $\overline{D}$ allows a $\overline{\Lambda}_c^-$ to carry the $\overline{c}$ quark, resulting in a sample contaminated with $\overline{p}\Lambda_c^+ \Longleftrightarrow N\overline{\Lambda}_c^-$ events. We do not want these events since the production model is an event with a Λ_c^+-$\overline{D}$ pair that carries the c and $\overline{c}$ quarks. To estimate the number of Λ_c^+-$\overline{\Lambda}_c^-$ pairs with an $\overline{p}$ in the data, events in which the decay $\overline{\Lambda}_c^- \to \overline{p}K^+\pi^-$ appears in the hemisphere opposite an $\overline{p}$ are selected. Since these events contain two antibaryons, it is very that likely a Λ_c^+ is present to carry the charm quark. Other particle combinations that conserve charm and baryon number have a low probability of occurrence since they would contain many massive particles (one $\overline{\Lambda}_c^-$, one charm meson, and three nucleons). Figure A.4 in Appendix A shows the fit results for the Λ_c^+ mass peak with a single $\overline{p}$ in the opposite hemisphere and zero fake tags. Tables 7.1 and 7.2 tabulate the results of the fit. The total number of $\overline{p}\Lambda_c^+ \Longleftrightarrow N\overline{\Lambda}_c^-$ events is

$$N_{\overline{p}\Longleftrightarrow\overline{\Lambda}_c^- \to \overline{p}K^+\pi^-} = \frac{N^{\overline{p}}_{pid-corrected}(\overline{p} \Longleftrightarrow \overline{\Lambda}_c^-)}{\varepsilon^{\overline{p}\Longleftrightarrow\Lambda_c^+}_{EventSelection} \cdot \varepsilon^{\overline{p}\Longleftrightarrow\Lambda_c^+}_{reco-\Lambda_c^+}}, \tag{7.5}$$

where the efficiencies are the same as described for Equation 7.4.

Table 7.3: Final results for the branching fraction calculation in data. The results are presented separately for each subsample of events and for the combined data sample. Results are shown for both R, defined in Equation 7.6, and for $\mathcal{B}(\Lambda_c^+ \to pK^-\pi^+)$. The errors shown are statistical only.

Block	Tag Charge	R	$\mathcal{B}(\Lambda_c^+ \to pK^-\pi^+)$
1	positive	$(5.69 \pm 0.59) \times 10^{-2}$	$(6.29 \pm 0.66) \times 10^{-2}$
1	negative	$(5.06 \pm 0.47) \times 10^{-2}$	$(5.58 \pm 0.52) \times 10^{-2}$
2	positive	$(5.82 \pm 0.62) \times 10^{-2}$	$(6.42 \pm 0.68) \times 10^{-2}$
2	negative	$(5.57 \pm 0.53) \times 10^{-2}$	$(6.15 \pm 0.58) \times 10^{-2}$
Combined	Combined	$(5.54 \pm 0.28) \times 10^{-2}$	$(6.12 \pm 0.31) \times 10^{-2}$

7.3 Branching Fraction Calculation

All the quantities needed to calculate the branching ratio have been defined in Equations 7.1- 7.5. They can be assembled into the final formula for calculating the branching fraction:

$$\mathcal{B}(\Lambda_c^+ \to pK^-\pi^+) = \frac{N_{\overline{p}\Lambda_c^+ \to pK^-\pi^+ \Longleftrightarrow} - N_{\overline{p} \Longleftrightarrow \overline{\Lambda}_c^- \to \overline{p}K^+\pi^-}}{N_{c+baryon} - N_{\overline{p}D \Longleftrightarrow N\overline{D}}} \cdot (1 + C) \qquad (7.6)$$

The branching fraction is determined independently for each subsample of this analysis. The results are then combined as in Equation 6.1. Subsamples are defined on the basis of the charge of the tag particle and the data block number. Using results presented in this chapter, the final measurements are shown in Table 7.3. The first two columns describe the subsample. The third column represents the result prior to the correction for the Ξ_c production rate. The fourth column lists the final result with Ξ_c correction calculated in Section 7.1.2. The errors shown are statistical only. The next chapter presents a discussion of the systematic errors.

Chapter 8

Cross-checks and Systematic Uncertainties

In earlier chapters, a variety of analysis issues that could effect the final results were identified. In this chapter, the impact of each of these effects on $\mathcal{B}(\Lambda_c^+ \to pK^-\pi^+)$ is discussed and the corresponding systematic uncertainty is estimated. The systematic uncertainties are summarized in Table 8.1. Because the final result is a ratio (Equation 7.6), many of the systematic errors will partially or fully cancel.

8.1 Beam Gas Interactions

Occasionally, a particle from the electron or positron beam collides with the nucleus of residual gas in the beampipe near the detector. This interaction results in the disintegration of the nucleus, causing neutrons and protons to fly into the detector. If a beam-gas interaction occurs in the same beam crossing as a physics event, the resulting protons will be reconstructed in the event. Because only protons are substantially generated in these interactions, the remainder of this section will concentrate protons.

Charge conjugation is not implied.

This analysis relies heavily on proton identification for the tag protons, thus, an increased production of protons could cause a systematic bias in the final results. Because beam-gas interactions produce protons and not antiprotons, this effect should be confined to the data sample with proton tags. A bias will occur if the relative number of beam-gas contaminated events and uncontaminated events is not equal for the Λ_c^+ production and $\Lambda_c^+ \to pK^-\pi^+$ event samples.

The easiest method to study beam-gas produced protons is to identify tracks that do not pass through the beam spot, but are still in the path of one of the beams. By investigating tracks that pass a distance of more than 3 cm in z from the beamspot, but fulfill all other tag proton selection criteria, beam-gas protons can be isolated.

Figure 8.1 shows the distance of closest approach after releasing the z-cut restriction. Using the events at large $|z|$ to determine the level of beam-gas interactions, the fraction of contamination within the ± 3 cm cut window is estimated. As the top plots demonstrate in Figure 8.1, an excess of tag particles is generated in the positively tagged samples. The excess is visible in the $\overline{D}^0$ and D^- samples because of the high yields in these samples. The lower yields of the D_s^- and Λ_c^+ samples suppresses the visibility of the beam-gas, though it is compatible with the levels in the $\overline{D}^0$ and D^- samples.

Assuming the background in the signal region is the same as the average density of protons in the sidebands, the beam-gas background is estimated to be roughly 2%. The distribution is similar in all the positively tagged charm hadron samples. The background is expected to be low since the timing requirements in the *BABAR* reconstruction software reject out of time detector signals. Any potential beam-gas interaction has a low probability of overlapping a physics event since it must occur within 1 ns of the reconstructed event time. Because the Λ_c^+ baryon yields appear in the numerator of the final result and the D meson samples appear in the denominator,

the minimal contributions cancel to less than 0.1%. No systematic error is assigned for this negligible effect.

8.2 D Meson Branching Fractions

The final result of this analysis is designed to be a ratio in which many of the systematic errors cancel. However, the denominator of the ratio depends on the branching fractions of the D mesons, and this error does not cancel. The current world averages and errors on the branching fractions [1] used in this analysis is discussed in Section 1.2:

- $B(D^0 \to K^-\pi^+) = 0.0383 \pm 0.0009$ (2%)
- $B(D^+ \to K^-\pi^+\pi^+) = 0.0900 \pm 0.0060$ (7%)
- $B(D_s^+ \to \phi\pi^+) = 0.0360 \pm 0.0090$ (25%)
- $B(\Lambda_c^+ \to pK^-\pi^+) = 0.050 \pm 0.013$ (25%)

These errors are propagated through to the final ratio calculation in Equation 7.6 and the final systematic error is $\pm 0.12 \times 10^{-2}$.

8.3 Control Samples

The systematic error resulting from the particle identification techniques is minimized by partial cancellation of systematic uncertainties in the numerator and denominator of Equation 7.6. The cancellation is not complete because of the slight differences in the momentum distributions for different charm hadrons and for tag $\overline{p}$'s in different hemispheres. The final systematic is determined by looking at two effects: the

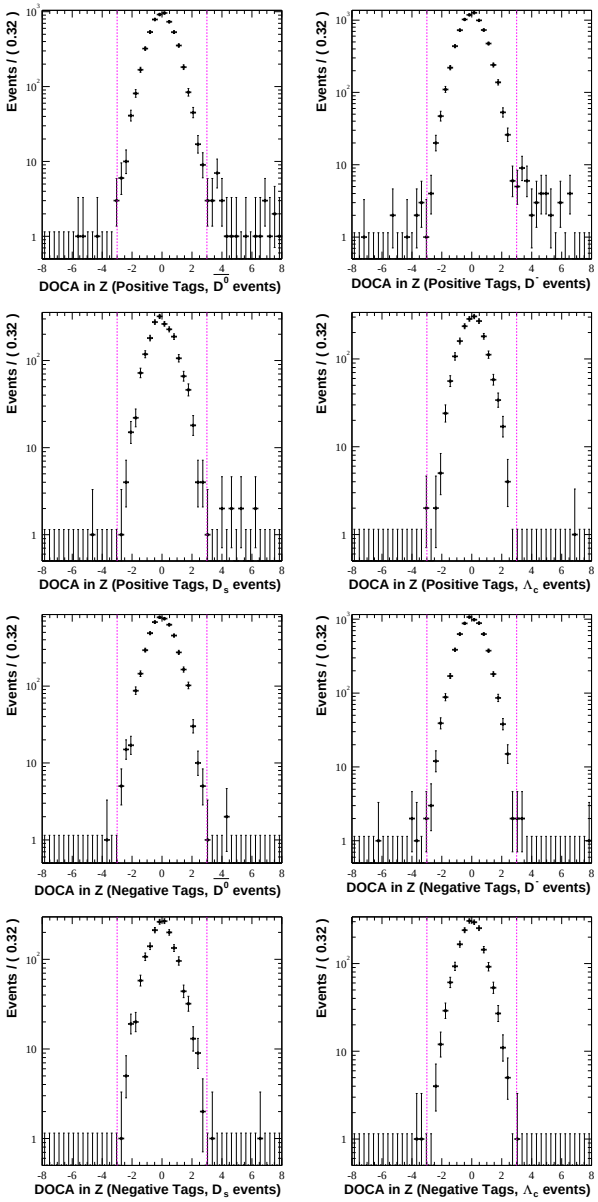

Figure 8.1: Distance of closest approach in z of the tag particles in data with respect to the middle of the interaction point (determined for each run) for proton tags (top 4 plots) and antiproton tags (bottom 4 plots), when the requirement that a proton comes from within 3 cm of the beam spot (dotted lines) is loosened. As shown in the plots, beam-gas contamination creates an excess of protons (top 4 plots) over $\overline{p}$'s.

statistical precision of the control samples and the cuts used to create the control samples.

To assess the magnitude of the first effect, all selection efficiencies used in the final branching fraction calculation are randomly varied and a new branching fraction is calculated. The variation is done using a binomial PDF with parameters determined from the statistical uncertainty in the efficiency measurement. The random variation is repeated 100 times; the spread in the resulting branching fraction values is used to calculate the systematic error. The final spread is $^{+0.17}_{-0.02} \times 10^{-2}$.

The second systematic effect of the particle identification methods is the kinematic cuts used to select the proton and kaon control samples used for efficiency calculations (see Section 4.1). The systematic is assessed by altering the cuts, repeating background subtraction, and recalculating the efficiencies. The hadron control samples are selected twice, once using a tighter set of cuts and once using a looser set of cuts. The branching fraction is recalculated with particle identification efficiencies from these new control samples. The spread in the new estimates of the branching fraction, $^{+0.02}_{-0.14} \times 10^{-2}$, is taken as the systematic error. This systematic is conservative - some spread is expected due to altered control sample statistics.

8.4 Hadron Tracking Corrections

Systematic errors resulting from the statistics of tracking efficiency calculations are included in the preceding section. This section deals with the systematics associated with the tracking system. Details on the tracking efficiency calculations are described in Section 3. The systematic for the procedure of estimating tracking efficiencies is 2% per track. Since all the samples have a similar number of tracks, the final systematic error on the ratio nearly cancels completely. The uncanceled systematic arises from the $\overline{D}^0$ samples that are reconstructed using only two tracks, as compared to other

charm hadrons that are reconstructed with three tracks. Propagating the 2% tracking error for the additional tracks in the D^-, D_s^-, and Λ_c^+ samples gives an absolute error of 0.08×10^{-2} on the final answer.

Systematic errors for tracking corrections due to kaon decays and interactions with detector material are estimated from the magnitude of their effects. When correcting for kaon decays in flight and interactions, the final branching fraction is increased by 0.05×10^{-2}. As shown in Section 3.3.1, this effect is understood to within 10% by kaon decays alone. The final systematic is assigned as the full magnitude of this uncertainty, or 0.005×10^{-2}.

Another systematic error stems from the calculation of the proton and antiproton tracking inefficiencies. Both of these calculations rely on Monte Carlo simulation that is not fully understood. Section 3.3.2 shows the interaction length estimate used by the GHEISHA simulation of the proton and antiproton propagation in detector material. The naive scattering model presented in that section overestimates the size of the inefficiency (i.e. predicts a smaller interaction length) by approximately a factor of two. If the tracking efficiencies for this analysis are recalculated without accounting for the additional scattering and annihilation of protons and antiprotons with respect to pions, the final branching fraction decreases by 0.25×10^{-2}. A systematic error of 0.25×10^{-2} is therefore assigned to represent the uncertainty in the Monte Carlo estimate of the proton and antiproton tracking inefficiency. This systematic is one of the largest because only partial cancellation occurs in the final ratio. The Λ_c^+ baryon is the only hadron reconstructed with a decay mode containing a proton, so the proton tracking inefficiency has a direct impact on the numerator of Equation 7.6.

The final tracking systematic comes from the removal of excess protons (charge conjugation not implied) described at the end of Section 3.3.2. To examine this effect, the final branching fraction is calculated both prior to and after removal of excess protons. The shift in the branching fraction is 0.01×10^{-2}. This issue is believed to be

understood quite well, and half of this shift is conservatively taken as the systematic error. The effect is small because the excess protons occur in every event subsample, and thus cancel in Equation 7.6.

8.5 Monte Carlo – Data Comparison

A cross-check is performed comparing expected momentum and polar angle distributions derived from Monte Carlo to distributions found in the data. The expected distributions are calculated by weighting each Monte Carlo event with tracking and particle identification efficiencies measured using the data control samples. The data distributions are found by performing a bin-by-bin invariant mass fit to the number of hadron signal candidates for the events in each bin.

Appendix D shows a sample of the figures showing comparison between Monte Carlo and data. The expected distributions are represented by histograms and the observed data distributions are shown as points with error bars. Because the luminosity of the Monte Carlo simulated data is less than the luminosity of the full data sample, the histogram's area is normalized to the integral of the data distributions.

The agreement between the Monte Carlo and the data is strong for the tag proton samples, as seen in Figures D.1 and D.2. This agreement builds confidence that the shapes of the Monte Carlo distributions reflect those of the data.

In the tag antiproton samples, agreement occurs in the polar angle distributions, but the momentum distributions are quite different below $1\,\mathrm{GeV}/c$ (Figures D.3 and D.2). The disagreement in the tag antiproton spectrum indicates that some mechanism for antiproton loss at low momentum, most likely annihilation, is modeled incorrectly in the Monte Carlo simulation. Because the disagreement is found in all tag antiproton samples, the systematic error is expected to be partially canceled in the final result. Full cancellation is not expected because the $\Lambda_c^+ \to pK^-\pi^+$ samples

have antiprotons not found in the reconstructed D samples. The simulation of proton interactions in the detector material was questioned in Section 3.3.2, and a systematic error for this inadequacy was calculated in the previous section. Since no other discrepancy is noticeable in the Monte Carlo, no additional systematic is assigned.

8.6 Event Selection

For an event to be used in this analysis, it must first pass the trigger and the hadronic-event cuts. The efficiencies for each type of event to be selected is detailed in Section 5.1. The systematic due to these calculations is found by propagating the errors through to the final result. The errors are mainly attributed to Monte Carlo statistics and are expected to be correlated and small. The cancellation resulting from correlations is large, giving only a modest uncertainty of 0.005×10^{-2} on the final result.

8.7 Ξ_c Production Rate

The final systematic error is the uncertainty on the quantity $C = \frac{\sigma(\overline{p}\Xi_c \Longleftrightarrow \overline{D})}{\sigma(\overline{p}\Lambda_c^+ \Longleftrightarrow \overline{D})}$ in equation 7.6. Section 7.1.2 describes how this quantity is calculated using JETSET for the fragmentation and hadronization process. This quantity is not well understood, and the error on it is conservatively estimated to be 50% of its value. Propagating this uncertainty to the final branching fractions gives a systematic uncertainty of 0.3×10^{-2}.

Table 8.1: Systematic errors on R, defined in Equation 7.3, and $\mathcal{B}(\Lambda_c^+ \to pK^-\pi^+)$. The errors on R are combined first. Next, the systematic error on C is combined to determined the final systematic on $\mathcal{B}(\Lambda_c^+ \to pK^-\pi^+)$.

Quantity	Systematic Error ($/10^{-2}$)
D Meson Branching Ratios	± 0.12
Tracking and PID Control Sample	$^{+0.17}_{-0.02}$
PID Control Sample	$^{+0.02}_{-0.14}$
Tracking Efficiency Determination	± 0.08
Kaon Tracking Efficiency	± 0.005
Proton/Antiproton Tracking Efficiency	± 0.25
Excess Proton Removal	± 0.005
Event Selection	± 0.004
Combined (R)	$^{+0.34}_{-0.32}$
Ξ_c Production Rate	± 0.24
Combined ($\mathcal{B}(\Lambda_c^+ \to pK^-\pi^+)$)	$^{+0.41}_{-0.42}$

8.8 Final Systematic Uncertainties

The systematic uncertainties quoted in the previous sections of this chapter are listed in Table 8.1. All of the errors are assumed to be uncorrelated. The errors relevant are combined in quadrature. First, the systematic errors on R (Equation 7.3) are combined, then the Ξ_c production fraction systematic is added to determine the final systematic error on $\mathcal{B}(\Lambda_c^+ \to pK^-\pi^+)$.

Chapter 9

Summary and Discussion

The final result of this analysis, $\mathcal{B}(\Lambda_c^+ \to pK^-\pi^+) = (6.12 \pm 0.31\ ^{+0.41}_{-0.42}) \times 10^{-2}$, is compatible with the previous RPP average of $(5.0 \pm 1.3) \times 10^{-2}$ [1] but represents a significant improvement in precision. Combining the two measurements, assuming they are uncorrelated, gives a new world average of $(6.0 \pm 0.5) \times 10^{-2}$. This brings the uncertainty down to 8% from 25%.

The final result also modifies the picture of the Λ_c^+ branching fractions described in Section 1.2. Since $\mathcal{B}(\Lambda_c^+ \to pK^-\pi^+)$ normalizes all the Λ_c^+ branching fraction measurements, a larger measurement for $\mathcal{B}(\Lambda_c^+ \to pK^-\pi^+)$ increases the total measured and estimated Λ_c^+ branching fractions from 78% to 92%. Although it is satisfying to produce total near 100%, it should be noted that no firm evidence exists that the estimated portion of the Λ_c^+ branching fractions is correct.

One other effect of an increase in $\mathcal{B}(\Lambda_c^+ \to pK^-\pi^+)$ is a decrease in the estimated number of Λ_c^+ baryons in the data samples of past experiments. This lowers the overall charm production rate for experiments measuring the number of charm quarks produced in Z^0 boson or in bottom hadron decays. Since approximately 8% [7, 9] of charm quarks hadronize into Λ_c^+ baryons in these experiments, a 1.5% decrease in the

charm yield is expected due to the larger $\Lambda_c^+ \to pK^-\pi^+$ branching fraction. Reducing charm yields also slightly widens the gap between experimentally measured values of n_c and the theoretical comfort zone depicted in Figure 1.7.

In addition to the new value of $\mathcal{B}(\Lambda_c^+ \to pK^-\pi^+)$, the improvement in precision has ramifications for charm counting experiments. Approximately half of the systematic error in the ALEPH and DELPHI measurements of R_c is attributed to the uncertainty in the charm hadron branching fractions. Prior to this measurement, an unknown portion of this error was due to the 25% uncertainty in $\mathcal{B}(\Lambda_c^+ \to pK^-\pi^+)$. With an error on $\mathcal{B}(\Lambda_c^+ \to pK^-\pi^+)$ of 8%, other systematics will begin to dominate. If a similarly precise measurement of $\mathcal{B}(D_s^+ \to \phi\pi^+)$ is made, then there is motivation for precision measurements of charm counting quantities.

The continued running of the *BABAR* experiment will bring advantages that could be used to refine this analysis. While the uncertainty on this result is not currently dominated by the statistical error, a larger data sample will have two beneficial effects. First, larger control samples would allow increased optimization of the proton and kaon selector performances leading to a decrease in the particle identification systematic error. Second, it may become possible to study events in which both a D meson and a Λ_c^+ baryon are reconstructed, eliminating the need to subtract the background originating from $\Lambda_c^+ \overline{\Lambda}_c^-$ events. It might then be reasonable to eliminate the requirement that an antiproton originate in the same (opposite) hemisphere as the Λ_c^+ ($\overline{D}$) hadron.

BABAR experimenters will also gain experience with the detector over time. Enhancements in tracking of charged particles will improve hadron reconstruction resolution and allow better identification of background protons in the analysis. Additional experience will also improve detector understanding, leading to increased realism in Monte Carlo simulations.

The major systematic error for this result is the uncertainty in the Ξ_c production

rate at the $\Upsilon(4S)$. It is not likely that *BABAR* or any similar experiment will improve this understanding, meaning a value with better than 8% precision may not be attainable with the current analysis model. CLEO-c plans to record a data sample at the energy threshold for $\Lambda_c^+ \, \overline{\Lambda}_c^-$ production, making this that experiment best suited to perform a precision measurement of $\mathcal{B}(\Lambda_c^+ \to pK^-\pi^+)$ free from model dependence. At threshold, any event with a fully reconstructed $\overline{\Lambda}_c^-$ baryon will contain a Λ_c^+ baryon. This would eliminate the need to tag lone antiprotons, and a measurement can be made using the ratio of "single-tags" to "double-tags". CLEO-c may also provide a cross-check for this analysis by going to the $\Xi_c \, \overline{\Xi}_c$ threshold and measuring absolute branching fractions for the Ξ_c baryon.

Appendix A

Fit Results

Results of several fits are presented in this appendix for readability of the original text. The figures are charm hadron invariant mass plots for data samples that contain a specific number of fake and real tag antiprotons in the opposite or same hemisphere as the candidate. Overlaid on each plot is the result of the fit to the sample. The fit for a particular charm hadron is done for the entire data block simultaneously, allowing only the number of signal and background events to be determined for each subsample. The number of signal and background events is shown in each figure, along with the χ^2 per degree of freedom. The parameters for the signal peak are listed in Table 5.6.

Because of the large number of subsamples with varying numbers of real and fake antiprotons, only a representative number of plots are included in this Appendix. Subsamples with a single tag particle are shown since these subsamples represent the largest fraction of the full signals.

Figure A.1 shows the $\overline{D}^0$, D^-, and D_s^- invariant mass spectrum for the subset of data in Block #1 with a tag antiproton detected in the hemisphere opposite the meson. No other real antiproton or fake antiproton tag is found in the event. These

events are the Λ_c^+ production events, in which a Λ_c^+ is expected to be produced. Figure A.2 shows D^0, D^+, and D_s^+ candidates in Block #1 with a tag antiproton in the same hemisphere as the meson. These events represent the $\overline{p}D \Longleftrightarrow N\overline{D}$ background to the Λ_c^+ production model, in which a p–D meson pair is created instead of a Λ_c^+ baryon.

Figure A.3 depicts the Λ_c^+ invariant mass spectrum for the subset of data in Block #1 with a tag antiproton detected in the same hemisphere as the Λ_c^+ candidate. No other real antiproton or fake antiproton tag is found in the event. These events are the Λ_c^+ signal events. Figure A.3 shows $\overline{\Lambda}_c^-$ candidate invariant mass in Block #1 for events in which a tag antiproton is found the hemisphere opposite the $\overline{\Lambda}_c^-$ candidate. These events represent the $\overline{p}\Lambda_c^+ \Longleftrightarrow N\overline{\Lambda}_c^-$ background to the Λ_c^+ signal in which a p–$\overline{\Lambda}_c^-$ pair are created instead of a $\overline{D}$ meson.

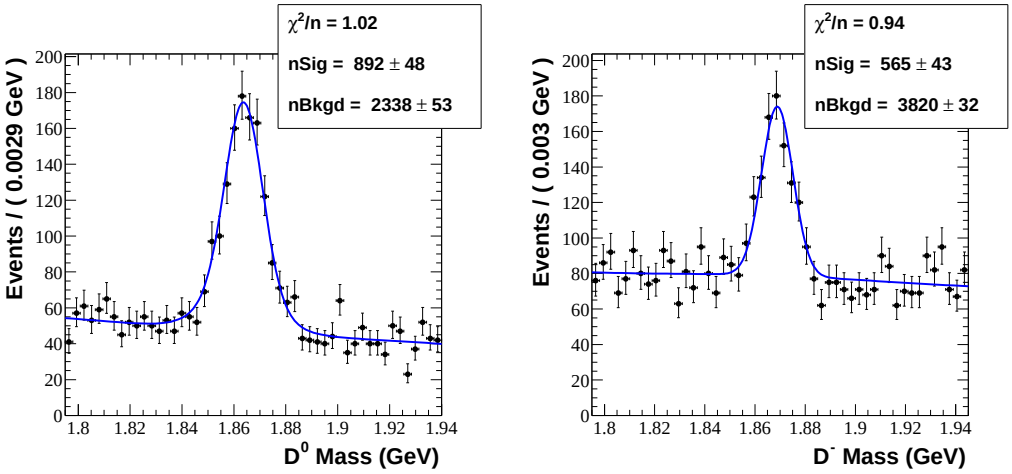

(a) $\overline{D}^0$ (b) D^-

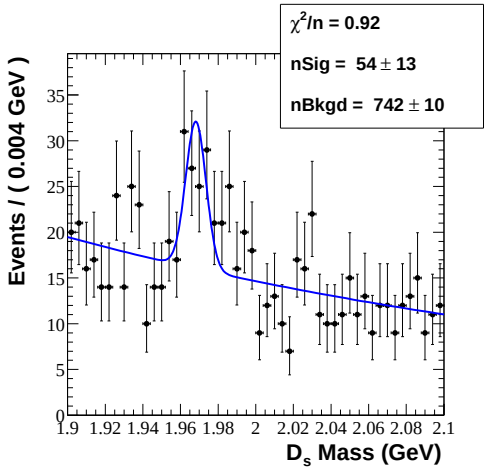

(c) D_s^-

Figure A.1: Invariant mass fits for the $\overline{D}$ mesons in the opposite event hemisphere as antiprotons. No other real antiprotons or fake antiprotons were detected in these events. The majority of these events are expected to contain a Λ_c^+ baryon.

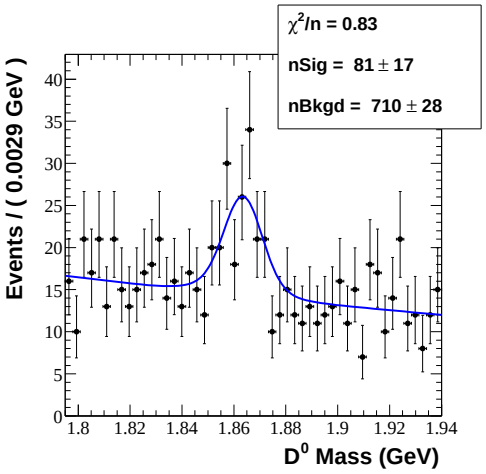

(a) $\overline{D}$

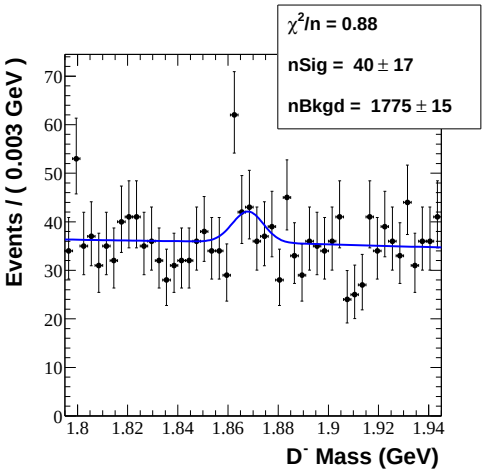

(b) D^+

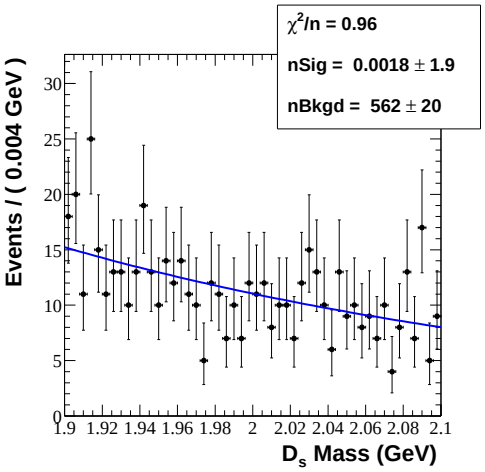

(c) D_s^+

Figure A.2: Invariant mass fits for the $\overline{D}$ mesons in the same event hemisphere as antiprotons. No other real antiprotons or fake antiprotons were detected in these events. These events represent the major source of background to the Λ_c^+ production events.

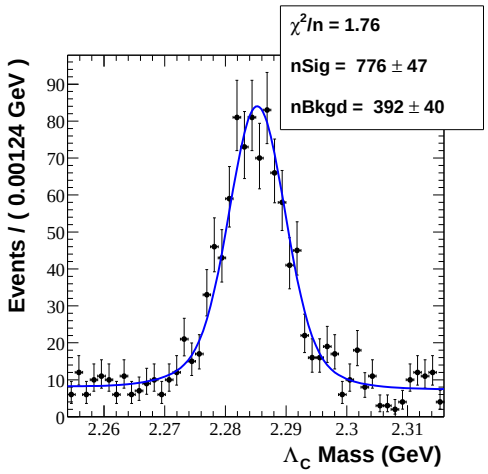

Figure A.3: Invariant mass fits for Λ_c^+ baryons in the same event hemisphere as antiprotons. No other real antiprotons or fake antiprotons were detected in these events.

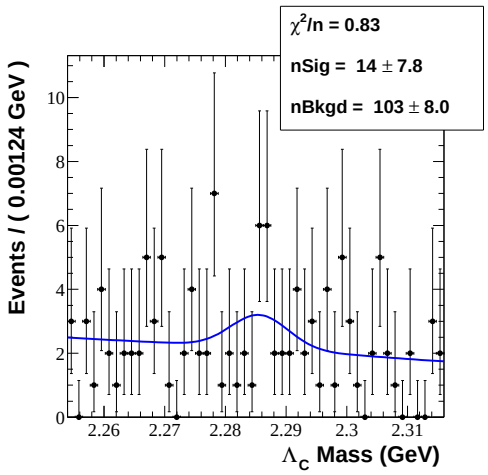

Figure A.4: Invariant mass fits for $\overline{\Lambda}_c^-$ baryons in the opposite event hemisphere as antiprotons. No other real antiprotons or fake antiprotons were detected in these events.

Appendix B

Monte Carlo Tracking Validation

Results of Monte Carlo tracking validation studies are shown in this appendix for clarity of the original text. The plots included here compare two sets of momentum and polar angle distributions. The points are from Monte Carlo particles that are found to be reconstructed by the tracking algorithms. The overlaid histograms are the result of weighting the initial Monte Carlo distributions with the tracking efficiencies calculated using separate control samples, as described in Chapter 3. The similarity of the two distributions, quantitatively represented by the Kolmogorov test score in the figures, verifies that the efficiency calculations and corrections are properly done.

The plots in this section show the momentum and polar angle distributions for the tag particles in events with D^0 and Λ_c^+ hadrons. Figures for positively and negatively charged tag particles are displayed. The upper plots in each figure require only that the tag particle be reconstructed. The lower plots require that all the particles in the event be reconstructed, verifying the tracking weights for all particles in the event.

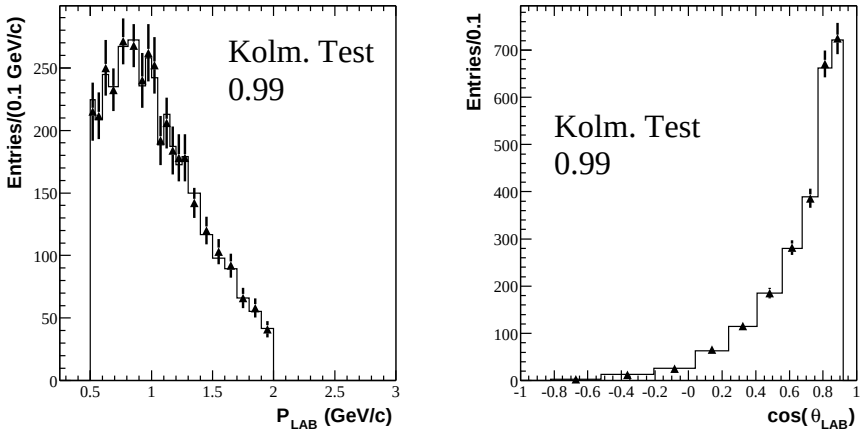

(a) Single particle efficiency weighting

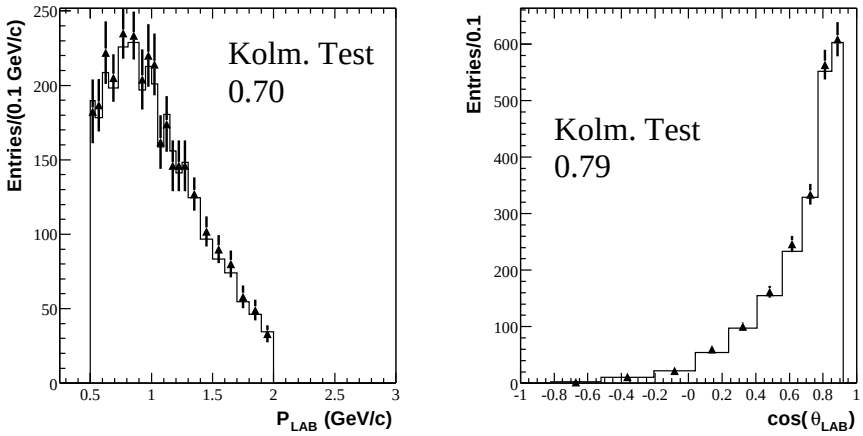

(b) Event efficiency weighting

Figure B.1: Monte Carlo tracking validation of momentum and polar angle distributions for a tag proton in the hemisphere opposite a D^0 meson.

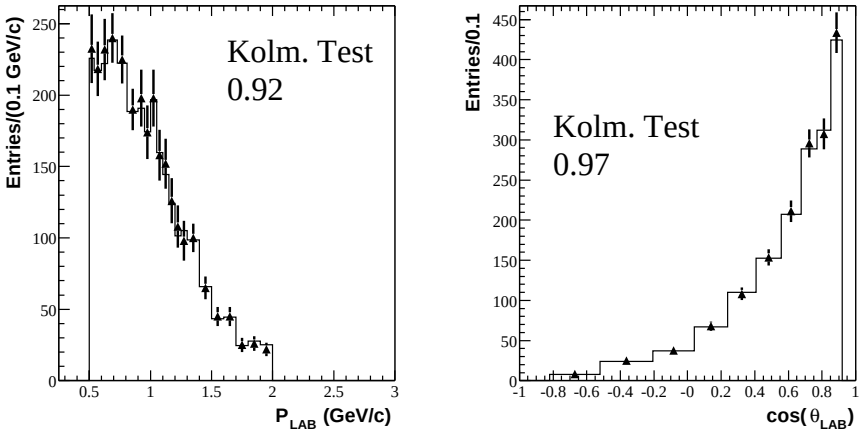

(a) Single particle efficiency weighting

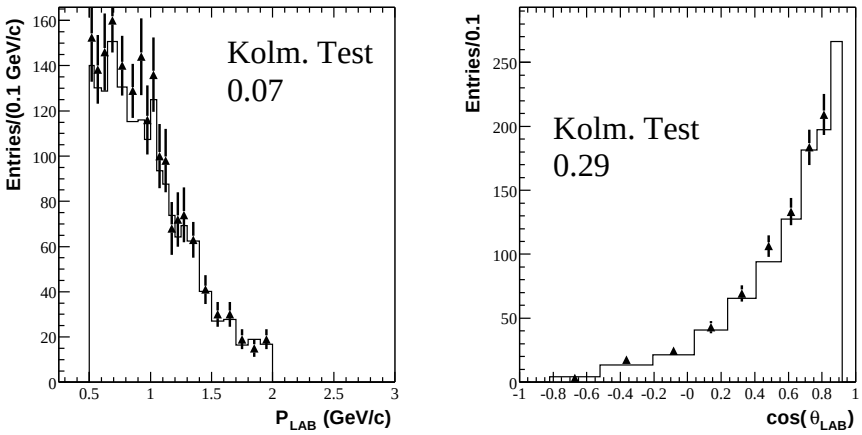

(b) Event efficiency weighting

Figure B.2: Monte Carlo tracking validation of momentum and polar angle distributions for a tag proton in the same hemisphere as a $\overline{\Lambda}_c^-$ baryon.

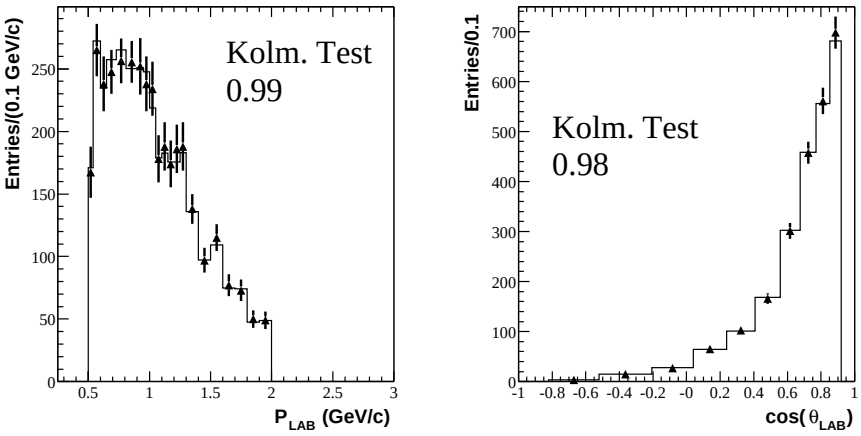

(a) Single particle efficiency weighting

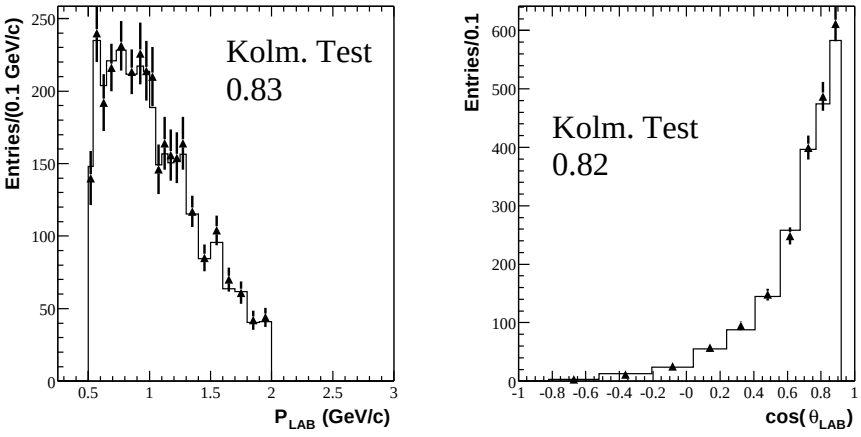

(b) Event efficiency weighting

Figure B.3: Monte Carlo tracking validation of momentum and polar angle distributions for a tag antiproton in the hemisphere opposite a $\overline{D}^0$ meson.

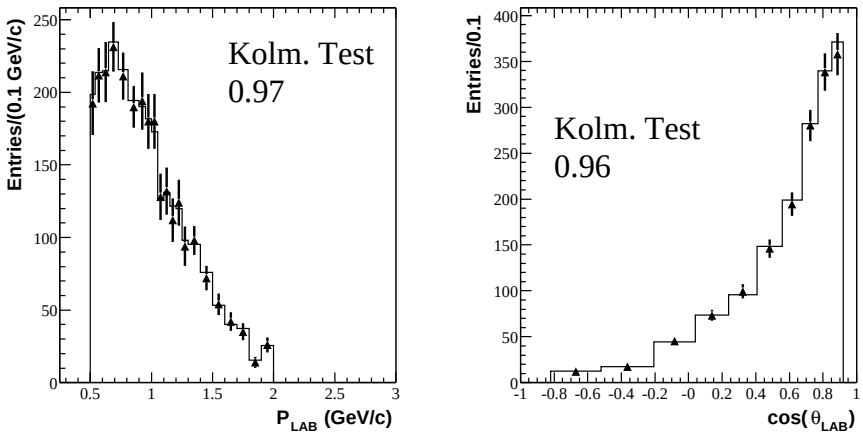

(a) Single particle efficiency weighting

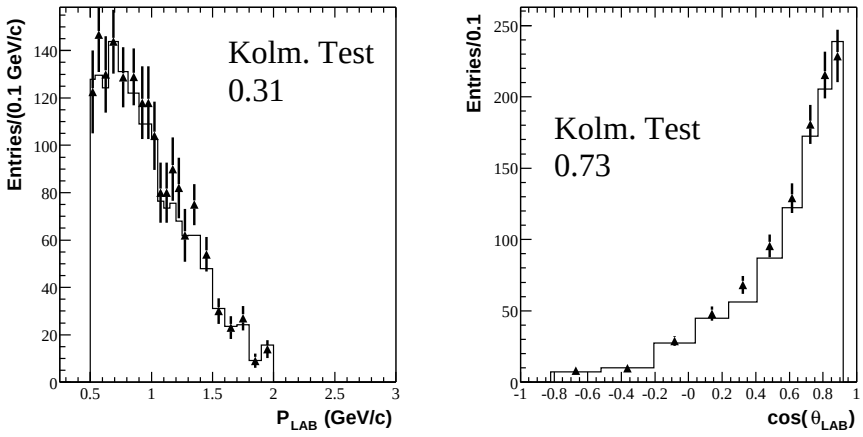

(b) Event efficiency weighting

Figure B.4: Monte Carlo tracking validation of momentum and polar angle distributions for a tag antiproton in the same hemisphere as a Λ_c^+ baryon.

Appendix C

Monte Carlo Particle Identification Validation

Results of Monte Carlo particle identification validation studies are included in this appendix for clarity of the original text. The plots shown here are similar to those in Appendix B, except that particle identification criteria are applied in addition to the tracking selection.

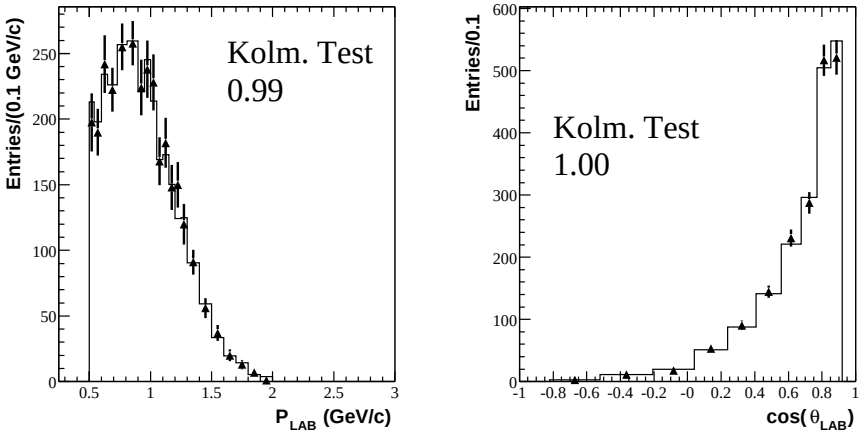

(a) Single particle efficiency weighting

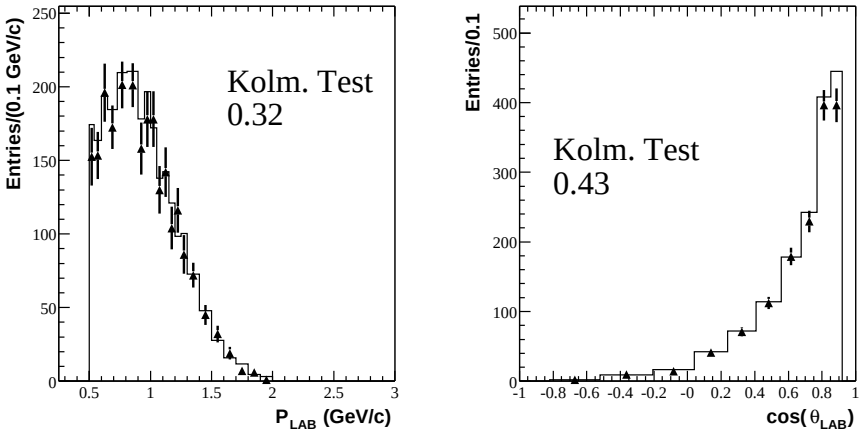

(b) Event efficiency weighting

Figure C.1: Monte Carlo particle identification validation of momentum and polar angle distributions for a tag proton in the hemisphere opposite a D^0 meson.

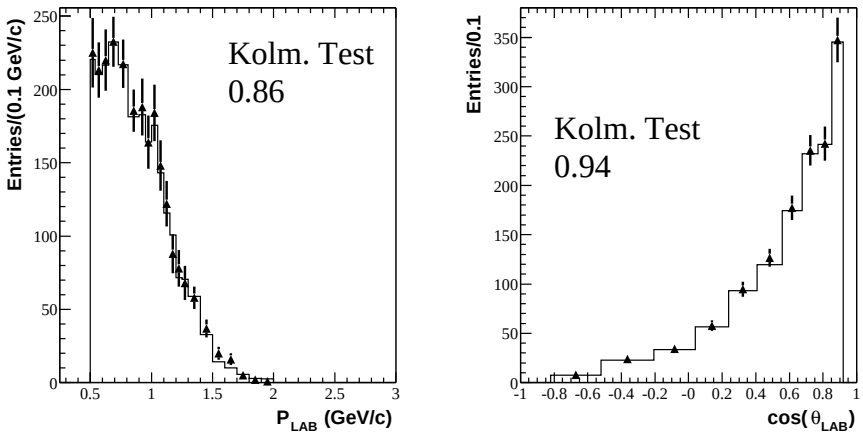

(a) Single particle efficiency weighting

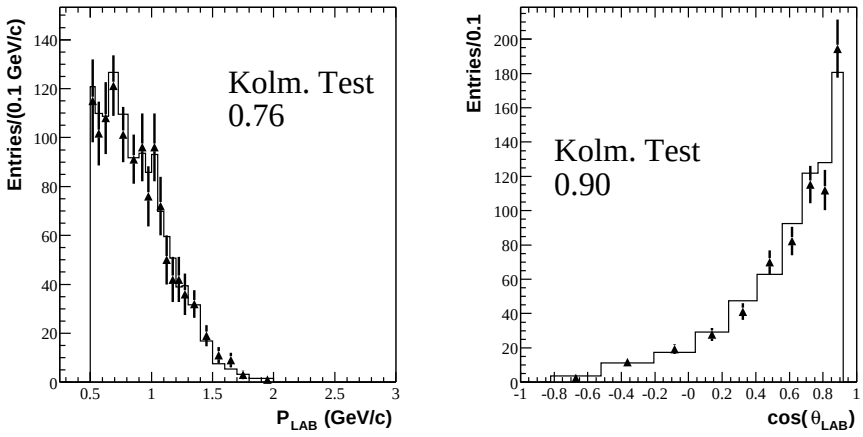

(b) Event efficiency weighting

Figure C.2: Monte Carlo particle identification validation of momentum and polar angle distributions for a tag proton in the same hemisphere as a $\overline{\Lambda}_c^-$ baryon.

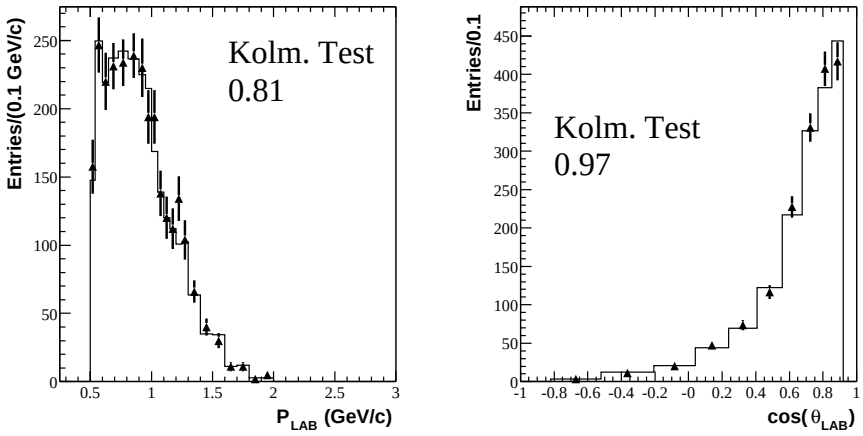

(a) Single particle efficiency weighting

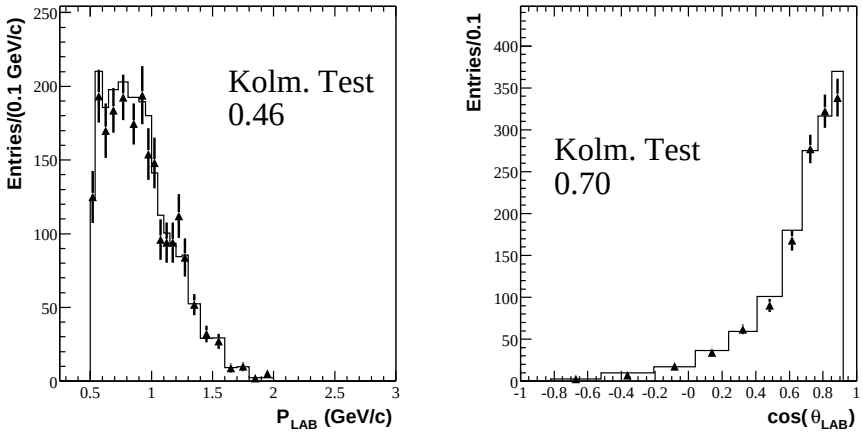

(b) Event efficiency weighting

Figure C.3: Monte Carlo particle identification validation of momentum and polar angle distributions for a tag antiproton in the hemisphere opposite a $\overline{D}^0$ meson.

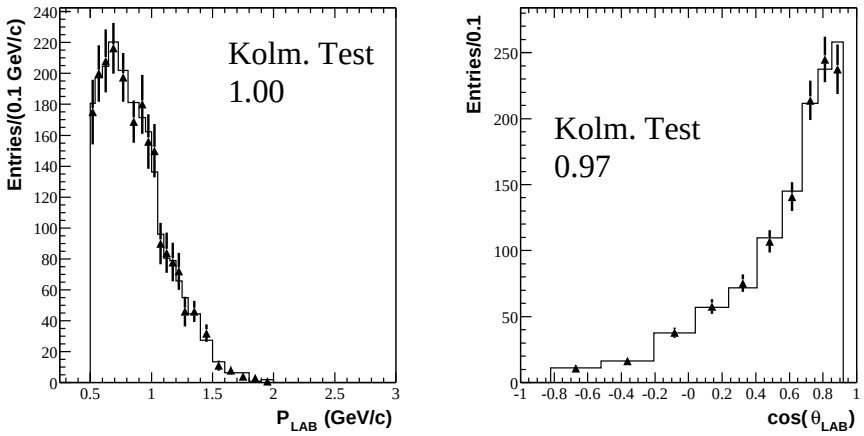

(a) Single particle efficiency weighting

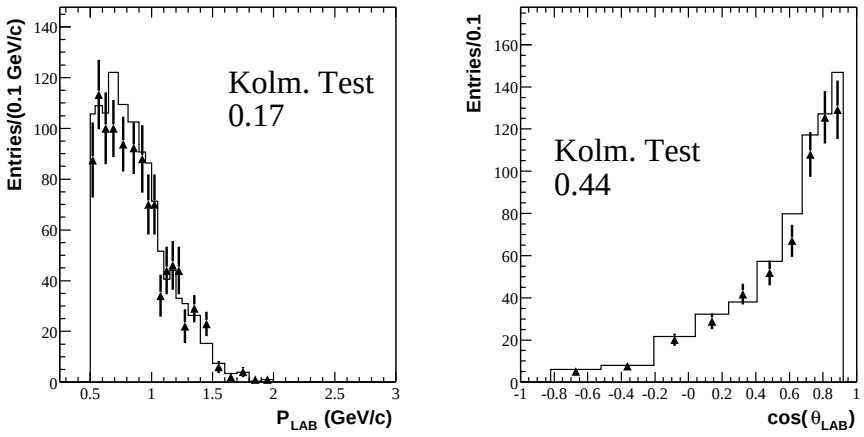

(b) Event efficiency weighting

Figure C.4: Monte Carlo particle identification validation of momentum and polar angle distributions for a tag antiproton in the same hemisphere as a Λ_c^+ baryon.

Appendix D

Monte Carlo – Data Comparison

Results of Monte Carlo – data comparison studies are included in this appendix for clarity of the original text. The plots shown here compare two sets of momentum and polar angle distributions. The histograms are Monte Carlo events that are weighted with tracking and particle identification efficiencies measured in the data control samples. The points are calculated by performing a bin-by-bin fit to the number of signal candidates in the invariant mass distribution. Because the luminosity of the Monte Carlo simulated data is less than the luminosity of the full data sample, the histogram's area is normalized to the integral of the data distributions. The similarity of the two distributions, quantitatively represented by the Kolmogorov test score in the figures, is a measure of how accurately the Monte Carlo simulates the data.

The plots in this section show the momentum and polar angle distributions for the tag particles in events with D^0 and Λ_c^+ hadrons. Figures for positively and negatively charged tag particles are included.

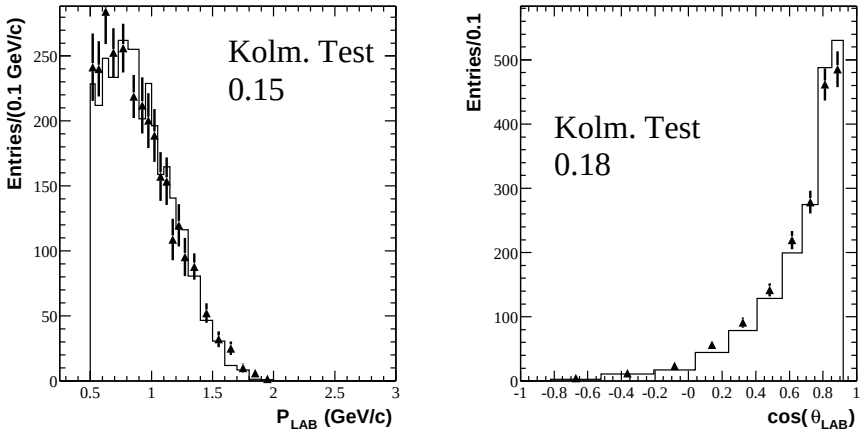

Figure D.1: Monte Carlo – data comparison of the momentum and polar angle distributions of a tag proton in the hemisphere opposite a D^0 meson. The histogram area is normalized to the integral of the data distribution.

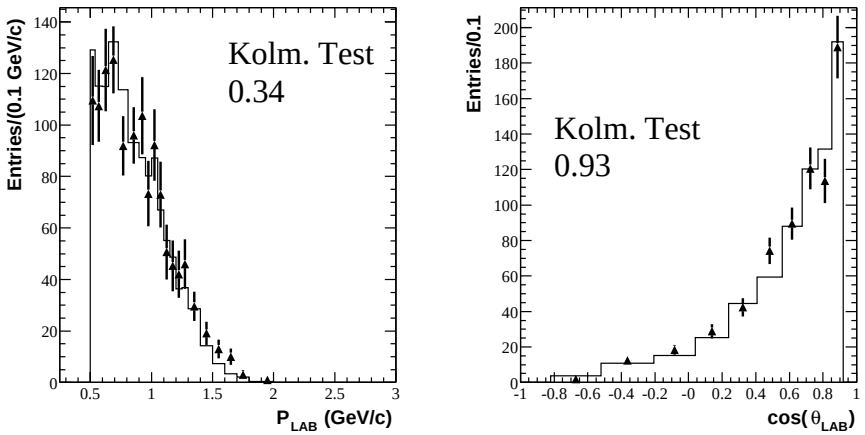

Figure D.2: Monte Carlo – data comparison of the momentum and polar angle distributions for a tag proton in the same hemisphere as a $\overline{\Lambda_c}$ baryon.

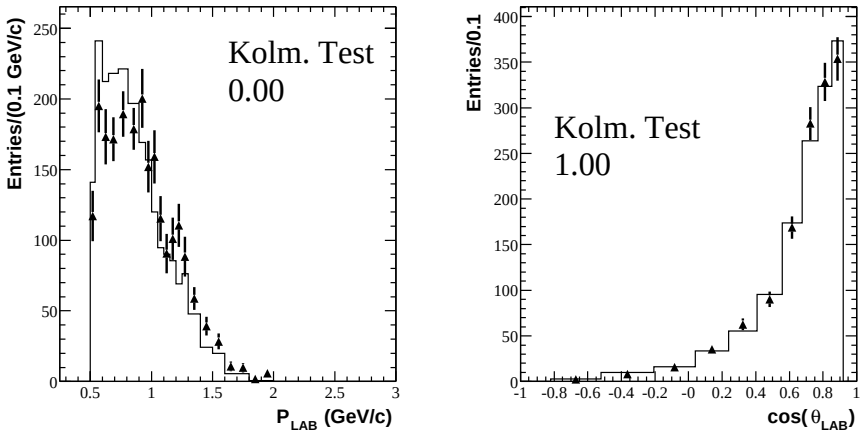

Figure D.3: Monte Carlo – data comparison of the momentum and polar angle distributions for a tag antiproton in the hemisphere opposite a $\overline{D}^0$ meson.

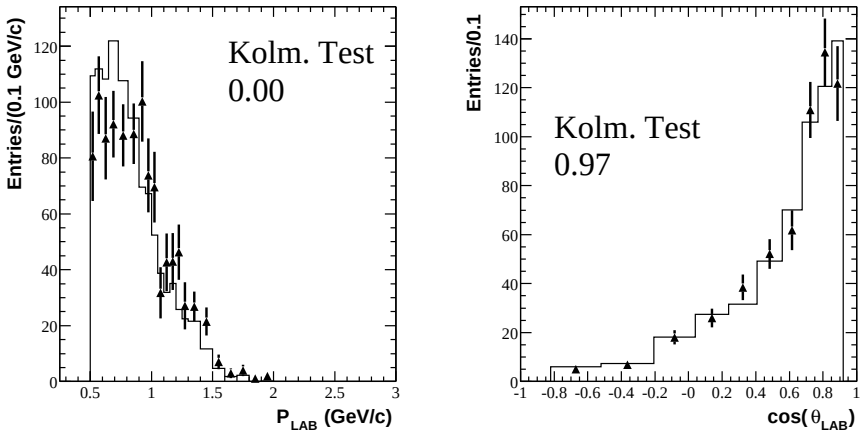

Figure D.4: Monte Carlo – data comparison of the momentum and polar angle distributions for a tag antiproton in the same hemisphere as a Λ_c^+ baryon.

Bibliography

[1] K. Hagiwara et al., "Review of Particle Physics," Physical Review D **66**, 010001 (2002).

[2] "Heavy Flavors 9," California Institute of Technology (2001).

[3] D. Griffiths, *Introduction to Elementary Particles*, John Wiley and Sons, Inc. (1987).

[4] C. Wohl, private communication.

[5] V. D. Barger and R. J. Phillips, *Collider Physics*, Addison-Wesley (1987).

[6] M. A. Samuel, "$Z \to b\bar{b}$ and $Z \to c\bar{c}$ as tests of the standard model and the mass of the Higgs boson," Phys. Lett. **B397**, 241–244 (1997).

[7] R. Barate et al., "Study of charm production in Z decays," Eur. Phys. Jour. **C16**, 597–611 (2000), hep-ex/9909032.

[8] P. Abreu et al., "Measurements of the Z partial decay width into $c\bar{c}$ and multiplicity of charm quarks per b decay," Eur. Phys. Jour. **C12**, 225–241 (2000).

[9] M. Neubert, "B decays and the heavy-quark expansion," Adv. Ser. Direct. High Energy Phys. **15**, 239–293 (1998), hep-ph/9702375.

[10] R. A. Poling, "Heavy quark decays," Int. J. Mod. Phys. **A15S1**, 53–79 (2000), hep-ex/0003025.

[11] H. Albrecht et al., "Observation of the Charmed Baryon Λ_c in e^+e^- Annihilation at 10 GeV," Phys. Lett. **B207**, 109 (1988).

[12] G. D. Crawford et al., "Measurement of baryon production in B meson decay," Phys. Rev. **D45**, 752–770 (1992).

[13] H. Albrecht et al., "Measurement of inclusive baryon production in B meson decays," Z. Phys. **C56**, 1–6 (1992).

[14] S. Anderson et al., "First observation of the decays $B^0 \to D^{*-}p\overline{p}\pi^+$ and $B^0 \to D^{*-}p\overline{n}$," Phys. Rev. Lett. **86**, 2732–2736 (2001), hep-ex/0009011.

[15] I. Dunietz, "On the necessity of recalibrating heavy flavor decays and its impact on apparent puzzles in high energy physics," (1996), hep-ph/9606247.

[16] I. Dunietz, "Heavy baryon production and decay," Phys. Rev. **D58**, 094010 (1998), hep-ph/9805287.

[17] D. E. Jaffe et al., "Measurement of $\mathcal{B}(\Lambda_c^+ \to pK^-\pi^+)$," Phys. Rev. **D62**, 072005 (2000), hep-ex/0004001.

[18] D. Kirkby and W. Verkerke, "The RooFit Toolkit for Data Modeling," http://roofit.sourceforge.net/.

[19] D. H. Perkins, *Introduction to High Energy Physics*, Addison-Wesley (1987).

[20] T. Sjostrand, "High-energy physics event generation with PYTHIA 5.7 and JETSET 7.4," Comput. Phys. Commun. **82**, 74–90 (1994).

[21] G. Corcella et al., "HERWIG 6: An event generator for hadron emission reactions with interfering gluons (including supersymmetric processes)," JHEP **01**, 010 (2001), hep-ph/0011363.

[22] S. Chun and C. Buchanan, "A simple plausible path from QCD to successful prediction of $e^+e^- \rightarrow$ hadronization data," Phys. Rep. **292**, 239–317 (1998).

[23] P. V. Chliapnikov, "Hyperfine splitting in light-flavour hadron production at LEP," Phys. Lett. **B462**, 341–353 (1999).

[24] B. R. Webber, "Fragmentation and hadronization," Int. J. Mod. Phys. **A15S1**, 577–606 (2000), hep-ph/9912292.

[25] H. R. Quinn et al., "The *BABAR* Physics Book," Technical Report (1998). SLAC-R-504.